UNIVERSITY OF CALIFORNIA
RIVERSIDE

Halo Formation in Self-Interacting Dark Matter Models

A Dissertation submitted in partial satisfaction
of the requirements for the degree of

Doctor of Philosophy

in

Physics

by

Omid Sameie

September 2019

Dissertation Committee:
Dr. Hai-Bo Yu, Chairperson
Dr. Laura Sales
Dr. Brian Siana

The Dissertation of Omid Sameie is approved:

_____

_____

_____

Committee Chairperson

University of California, Riverside

Acknowledgements

I'd like to express my gratitude to all who supported me throughout my Ph.D. years. Above all, I am grateful to my family who supported me unconditionally. I'd like to thank my advisors Dr. Hai-Bo Yu and Dr. Laura Sales. Without their support and guidance it would have not been possible for me to make any major progress or achievements. Hai-Bo and Laura have provided the best advice and supervision I could get. I would also like to thank other members of Physics and Astronomy Department at UC Riverside for being such amazing colleagues. I am also grateful to my research group members, specially Dr. Peter Creasey who has been an invaluable instructor to me.

I'm delighted and grateful to my collaborators at Carnegie observatories, specially Dr. Andrew Benson. It has been my great pleasure to work with him over the last couple of years of my Ph.D. program. I would like to extend my acknowledgement to Dr. Leonidas Moustakas for his continuous support.

I'd like to thank all my previous teachers and advisors back home, specially Mr. Mohammad Ali Najafi, Dr. Ahmad Ghodsi, Dr. Hamid Reza Sepangi, and Dr. Hassan Firouzjahi.

Since January 2017, I have been supported by the NASA MIRO FIELDS fellowship. This has been a great opportunity for me to expand my circle of collaboration beyond UCR. I'd like to thank all people involved in this program, specially Dr. Bahram Mobasher.

Finally, I want to thank Pooya, Ardalan, Aghil, Saeed, Ehsan, Peyman, Fariborz, Parham, Pouria, Amin, Farzin, Ana, and Xinnan for being such unbelievable friends.

To my parents,

Akram and Toktam,

and my grandparents

ABSTRACT OF THE DISSERTATION

Halo Formation in Self-Interacting Dark Matter Models

by

Omid Sameie

Doctor of Philosophy, Graduate Program Physics
University of California, Riverside, September 2019
Dr. Hai-Bo Yu, Chairperson

The standard model of cosmology assumes that dark matter (DM) is cold and collisionless. This collisionless Cold DM (CDM) model has been extremely successful in explaining various observational phenomena on scales larger than galaxies. Despite the successes on large scales, the CDM model faces several challenges on smaller scales that have puzzled the community for many years. One of the most intriguing discrepancies between CDM predictions and observations is about the DM content in dwarf and spiral galaxies. While CDM predicts radially divergent DM density cusps at the halo centers, many observations suggest constant DM density cores. Abundance of the observed Milky Way satellite galaxies has also been at odds with the predictions from CDM. While observations suggest that the number of luminous Milky Way satellites is less than 100, CDM N-body simulations predict 1-2 orders of magnitude more subhalos for a Milky Way-like galaxy.

As an alternative to CDM, self-interacting dark matter (SIDM) models are proposed as potential solutions to some of these cosmological issues. In this class of DM models, DM-DM scattering leads to distributions of energy at the center of the halo such that after a few dynamical times, the inner halo reaches an isothermal state. This results in the re-distribution of DM particles, which, in principle, can form constant density cores opposite to the cusps predicted by the CDM

model. The interaction between dark matter particles can be extended to the scenarios where DM scatters off from some *other* relativistic dark sector particles (e.g. dark photons), leading to suppressions in the matter power spectrum. This results in the depletion of DM halos in the regime corresponding to this cutoff in the matter power spectrum, which provides another channel to address the tension between theoretical predictions and observations.

In this dissertation, I study the impact of non-gravitational interactions in the dark sector on the distribution and evolution of DM halos. I find that when entangled with the baryonic potentials, SIDM models possess rich phenomenology for the formation of structures in the universe. For isolated DM halos with low baryonic content, like many dwarf-sized galaxies, DM-DM interactions lead to a cored DM density profile, as expected from the isothermal behavior of SIDM. On the other hand, in isolated halos with a more significant contribution of baryons, closer to the mass scale of the Milky Way, DM self-interactions trigger a phase of core contraction, leading to a high central density. For subhalos within a main host, the environmental effects, such as tidal stripping and tidal shocking, can dramatically change the fate of these objects. While gravitational tides remove mass from outskirts of the satellite halos, the heat transport due to the DM self-interactions can speed up core collapse. The transition from the core expansion phase to core collapse phase is controlled by the orbit and pre-infall halo parameters.

In the DM models, where DM experiences interactions with dark photons, the suppression in the matter power spectrum causes a depletion of DM halos in the regime of dwarf galaxies. In this dissertation, I develop an analytical Press-Schechter approach to compute halo abundance for SIDM models in a more computationally efficient way compared to the conventional numerical simulations. I calibrate and test this analytical model with cosmological simulations, and show that it is robust over different SIDM models, halo mass regimes, and cosmological timescales. I use this formalism to constrain the parameter space of DM-dark photon interactions.

Contents

List of Figures

List of Tables

Chapter 1

Introduction

Since its first discovery (Zwicky, 1933, 1937; Rubin and Ford, 1970), the nature of Dark Matter (DM) has remained elusive. The current standard model of cosmology assumes dark matter is a massive particle with negligible relic thermal velocity, and interacts only through gravity (Planck Collaboration et al., 2018). This collisionless Cold DM (CDM) paradigm has been a cornerstone to galaxy formation models (Springel, 2005; Vogelsberger et al., 2014b; Schaye et al., 2015; Wang et al., 2015; Hopkins et al., 2018). Current theoretical models for how galaxies form and evolve agree well with a plethora of observations such as large-scale clustering, lensing, and scaling relations. Despite its successes in many different large-scale observations (Planck Collaboration et al., 2014; Percival et al., 2007), CDM has faced different challenges on the scales relevant to galaxies smaller than the Milky Way (MW) (see Bullock and Boylan-Kolchin, 2017, for a review). Most of these inconsistencies have roots in the fact that the prediction of CDM for the distribution of DM, characterized by Navarro-Frenk-White (NFW) profile (Navarro et al., 1997), is radially divergent at the center of DM halos, i.e. density cusps. In contrast, the observations of many dwarfs and spiral galaxies prefer shallower DM distributions, i.e. density cores (Moore, 1994; Flores and Primack, 1994; de Blok et al., 2008; Oh et al., 2011, 2015).

This so-called “core-cusp" issue can be promoted to the diversity in the shape of galactic rotation curves. Oman et al. (2015) compared circular velocities of observed galaxies, defined as $V_{\rm circ}(r) = \sqrt{\frac{GM(r)}{r}}$, to the predictions of the CDM model inferred from cosmological simulations.

They found that the scatter in the DM content of these galaxies at the central region within few kpc is systematically larger than that predicted by the CDM model.

One possibility to reconcile the observations with numerical simulations is to invoke baryonic processes, such as stellar feedback mechanisms (Navarro et al., 1996; Binney et al., 2001; Mo and Mao, 2004; Read and Gilmore, 2005; Mashchenko et al., 2006, 2008; Pontzen and Governato, 2012; Brooks and Zolotov, 2014). Stellar feedback generates substantial gas outflows, which can cause fluctuations in the gravitational potential, reducing the central DM density. However, uncertainties in the sub-resolution physics associated with the feedback processes have left the parameter space of these mechanisms largely unconstrained, imposing the question of whether feedback can address these small-scale issues (Gnedin and Zhao, 2002; Ceverino and Klypin, 2009; Schaye et al., 2015; Zhu et al., 2016). Moreover, for the least massive galactic systems, i.e. dwarf spheroidals and ultra faint dwarfs, the relative contribution of baryons to the total mass is sub-dominant such that feedback mechanisms are unlikely to alter the DM density profiles (Garrison-Kimmel et al., 2013; Bose et al., 2019).

An alternative approach is to modify the underlying assumptions about the nature of DM. In a pioneering study, Spergel and Steinhardt (2000) proposed that DM self-interactions can potentially alleviate the tension in the observed central DM density (Tulin and Yu, 2018). The basic idea involves the thermalization of central region due to the DM self-interactions where the cuspy density profile predicted by the CDM model turns into a cored profile. DM particles with a large self-interaction cross section per unit mass, $\sigma/m \sim 1$ cm^2/g, experience multiple scatterings in the inner halo over the cosmological timescale, making distinct departures from the CDM predictions. The outer halo, in the contrary, remains collisionless, and therefore retains the large-scale predictions of the CDM (Spergel and Steinhardt, 2000; Yoshida et al., 2000b; Davé et al., 2001; Colín et al., 2002; Vogelsberger et al., 2012; Rocha et al., 2013).

Following the first cosmological simulations of the SIDM models (Yoshida et al., 2000b,a; Davé et al., 2001; Firmani et al., 2001), several authors pointed out that a single cross section cannot satisfy the observed central densities in both dwarf galaxies and more massive systems such as galaxy clusters (Miralda-Escudé, 2002; D'Onghia and Burkert, 2003). However, these

concerns may be avoided by considering a velocity-dependent DM cross section (Feng et al., 2009; Vogelsberger et al., 2012; Rocha et al., 2013). Moreover, Peter et al. (2013) showed that previous analysis regarding the impact of DM self-interaction on the halo shape of galaxy clusters has been overestimated. Overall, these works suggest that a DM model with a velocity-dependent cross section σ/m $(\overline{v})$ equal to $\sim 1-10$ cm^2/g in the regime of dwarf galaxies and ~ 0.1 cm^2/g in the mass-scale of galaxy clusters would pass any current observational constraints (Kaplinghat et al., 2016).

One of the shortcomings of these simulations was the absence of baryonic effects. Inclusion of the baryonic gravitational potential results in the adiabatic contraction of DM halos (Blumenthal et al., 1986; Abadi et al., 2010; Gnedin et al., 2011). In addition, star formation followed by stellar feedback may remove some of these DM particles from the galactic center. Kaplinghat et al. (2014) used the Jeans model to study the impact of DM self-interactions and baryons on the shape and distribution of DM particles in the halos. Their analysis shows that the DM density profile inferred from the isothermal solution is controlled by the total gravitational potential, $\rho_{\rm dm}(r) \propto \exp\big(-\frac{\Phi_{\rm tot}(r)}{\sigma_0^2}\big)$. As a result, a significant contribution from the baryons can change both the DM density slope and the 3D shape of the halo. However, only a few full hydrodynamical SIDM simulations have been performed to test these analytical predictions (Robles et al., 2017a; Fitts et al., 2018; Robertson et al., 2018b,a). The main challenge is that hydrodynamical SIDM simulations are computationally expensive, and the force/mass resolution necessary to probe the inner region of dwarf galaxies requires state of the art computational resources.

The gravitational effects of baryons can be modeled as analytical potentials in the idealized N-body simulations, which has been demonstrated to be fruitful for the CDM model (Johnston et al., 1995; Muñoz et al., 2008; Peñarrubia et al., 2008; Kazantzidis et al., 2009; D'Onghia et al., 2010; Garrison-Kimmel et al., 2017). It is worth noting that this method neglects the back-reaction of the DM distribution on the baryons and the impact of the stellar feedback on the DM density profile. The latter approximation, however, is justified by a couple of studies showing that in the presence of thermalized cores, feedback doesn't alter the shape of the DM density profiles (Robles et al., 2017a; Robertson et al., 2018b). As a result, The analytical

potentials have been implemented in numerical simulations for both CDM and SIDM models.

Lastly, DM might have also experienced scattering from relativistic particles in the early universe. In this class of SIDM models, the interactions between DM and other relativistic components in the dark sector (e.g. dark photons) would have suppressed the linear matter power spectrum (Chacko et al., 2016; Cyr-Racine et al., 2016; Brust et al., 2017; Feng et al., 2009). This consequently changes the abundance of the DM halos in the regime relevant to the cutoff in the power spectrum (Buckley et al., 2014; Vogelsberger et al., 2016; Murgia et al., 2017).

In this dissertation, I use both analytical methods and numerical simulations to study SIDM in the context of galaxy formation. I perform both cosmological and controlled N-body simulations to investigate the effects of dark matter interactions on the abundance and structure of DM halos. In a series of papers (Creasey et al., 2017; Sameie et al., 2018, 2019), I use some of these tools to study 1) the impact of SIDM plus baryons on the shape of the circular velocity in the field galaxies, Chapter 2, 2) impact of the baryonic distribution on the 3D shape and density profile of SIDM halos, Chapter 3, and 3) the fate of MW satellites in the presence of DM self-interactions, Chapter 4. In Chapter 5, I consider the general approach of the extended Press-Schechter formalism (Press and Schechter, 1974; Bond et al., 1991; Bower, 1991) to examine whether this framework can accurately calculate the halo abundance in the SIDM models with DM-dark photon interactions. I calibrate the Press-Schechter formalism to N-body simulations, and show that it can accurately predict the number density of halos (halo mass function) in the mass regime where the power spectrum is suppressed.

Chapter 2

Creating diverse rotation curves via baryonic and self-interaction effects

2.1 Introduction

ΛCDM makes testable predictions at galactic scales that can be contrasted with observations. Among the most fundamental of them is for the structure of dark matter halos, with a density profile parameterised by a Navarro-Frenk-White (NFW) profile (Navarro et al., 1997), which at the inner radii scales as a power law $r^{-\alpha}$ with $\alpha \approx 1$. Observations, however, of the rotation curves of spiral galaxies, including dwarf and low surface brightness galaxies, often exhibit an inner circular velocity of stars and gas that increases more mildly than expected from a CDM halo (e.g. Flores and Primack, 1994; Moore, 1994; Persic et al., 1996; Kuzio de Naray et al., 2008; Oh et al., 2015), indicating an inner density profile shallower than the NFW cusp, i.e., $\alpha < 1$. This discrepancy can be further generalised as the mass deficit problem: the CDM halo contains too much dark matter mass in the inner regions than inferred from observations (Boylan-Kolchin et al., 2011; Ferrero et al., 2012; Papastergis et al., 2015; Papastergis and Shankar, 2016; Schneider et al., 2016).

A more intriguing observation is that the galactic rotation curves exhibit a large diversity. Individual fits to galaxy rotation curves span a spectrum from cores $\alpha \approx 0$ (e.g. Côté et al.,

2000; de Blok et al., 2008; Kuzio de Naray et al., 2010) to cusps (e.g. van den Bosch et al., 2000; Swaters et al., 2003; Spekkens et al., 2005), and in the case of cored profiles, the central densities can differ by factor of 10 for galaxies inhabiting similar halos (Kuzio de Naray et al., 2010). Recently, Oman et al. (2015) quantified this diversity in rotation curves by comparing $V_{2\,\mathrm{kpc}}$ for a fixed V_{max}, where $V_{2\,\mathrm{kpc}}$ is the circular velocity at 2 kpc and V_{max} is the peak circular velocity. For V_{max} in the range of 50–250 $\mathrm{km\,s^{-1}}$, the scatter in $V_{2\,\mathrm{kpc}}$ is a factor of 3-4 and consequently the mechanism invoked to generate cored profiles must also accommodate this large variations in rotation curve shapes. Notably mass modelling is subject to significant uncertainties, especially at the scale of low mass dwarfs where pressure support effects, triaxiality, inclination, hidden bars and other irregularities hamper the utility of circular velocity profiles for mass modelling (Hayashi et al., 2004; Rhee et al., 2004; Pineda et al., 2017; Read et al., 2016b), making it hard to assess the precise spread in the rotation curves. In this paper, we take the result reported in Oman et al. as our reference.

The distribution of rotation curves is clearly too heterogeneous to be indexed with a single parameter. For example, several different galaxy formation models seem able to reproduce the Tully-Fisher (Tully and Fisher, 1977) relation within ΛCDM (McCarthy et al., 2012; Brook et al., 2016; Di Cintio and Lelli, 2016; Sales et al., 2017; Ferrero et al., 2017; Santos-Santos et al., 2016; Katz et al., 2017) provided the stellar feedback populates dark matter halos with the right stellar mass and size (though see also Pace, 2016), yet despite this global consensus the circular velocity profiles predicted by each model differ in detail, with some cases leading to the formation of cores (e.g. Governato et al., 2010; Pontzen and Governato, 2012; Di Cintio et al., 2014; Read et al., 2016a; Wetzel et al., 2016) whereas other simulations preserve the inner dark matter cusps (e.g. Sawala et al., 2015; Vogelsberger et al., 2014a; Schaller et al., 2015). The disagreement may arise from the inclusion of different physical processes, different numerical implementation or may even vary with star formation histories (e.g. Oñorbe et al., 2015; Tollet et al., 2016).

In particular, the feedback model applied by Oman et al. (2015) appears unable to explain the scatter in observations within the ΛCDM framework. On the other hand, Brook (2015) finds

good agreement between simulations and observations when looking at the scatter in the ratio between the circular velocity at 1 kpc and $V_{\rm max}$. Similarly Read et al. (2016b) has also found consistency between baryon induced cores within ΛCDM and the shape of observed rotation curves. It is unclear, however, that this baryonic solution would hold if the size of the cores measured in observations is $\gtrsim$1 kpc (see for instance Tollet et al., 2016). In fact, this may represent a serious limitation of this solution. For example IC 2574 has an inferred cored inner halo which extends for 8 kpc, well beyond the radius of the stars, with a stellar half-mass radius of 5 kpc. This type of object is a challenge to the hypothesis of feedback generated cores since, by construction, the extent of the cores in such scenarios is limited to the region where stars form and deposit their energy (Di Cintio et al., 2014).

An alternative solution is to consider cores formed out of self-interacting dark matter (SIDM), which we explore in this paper. The SIDM model retains important features of the CDM model including the distribution of halo concentrations as a function of mass (Rocha et al., 2013). SIDM differs, however, in that scattering between dark matter particles leads to heat transfer and the generation of dense cores in the inner regions of halos (Spergel and Steinhardt, 2000; Firmani et al., 2001). Recent high-resolution N-body simulations have shown that the self-interaction cross-section per unit mass $\sigma_{\rm T}/m_\chi \sim 1$ cm^2 g^{-1} is required to have core densities that are preferred by galaxy observations (Vogelsberger et al., 2012; Zavala et al., 2013; Rocha et al., 2013; Elbert et al., 2015). Kaplinghat et al. (2016) finds $\sigma_{\rm T}/m_\chi \approx$ 1–3 cm^2 g^{-1} by directly fitting the rotation curves of dwarf galaxies. On the other hand, there are various constraints on $\sigma_{\rm T}/m_\chi$, including merging clusters (Randall et al., 2008; Kahlhoefer et al., 2014; Robertson et al., 2017; Kim et al., 2017b), shapes of elliptical galaxies and galaxy clusters (Miralda-Escudé, 2002; Feng et al., 2009; Peter et al., 2013), core sizes of clusters (Yoshida et al., 2000b; Rocha et al., 2013; Kaplinghat et al., 2016; Elbert et al., 2018), and survival of dwarf halos from evaporation (Gnedin and Ostriker, 2001).

Among these constraints the strongest limit is $\sigma_{\rm T}/m_\chi \lesssim$0.1 cm^2 g^{-1} in galaxy clusters (Yoshida et al., 2000b; Kaplinghat et al., 2016; Elbert et al., 2018), where the relative dark matter velocity $v \sim 1500$ km s^{-1}. As such, the self-interaction cross-section should have a mild velocity

dependence, which can be naturally realised in a class of hidden sector dark matter models with a light force mediator (e.g. Feng et al., 2009, 2010; Buckley and Fox, 2010; Loeb and Weiner, 2011; Tulin et al., 2013a,b; Boddy et al., 2014, 2016). A velocity-dependent SIDM model, based a Yukawa potential, has been implemented in zoom-in N-body simulations (Vogelsberger et al., 2012, 2016), and further generalised in the ETHOS (Effective Theory of Structure Formation) framework, mapping underlying particle physics parameters to astrophysical observables (Vogelsberger et al., 2016; Cyr-Racine et al., 2016).

This approach has several distinct features that help explain the rotation curve diversity. Firstly, the scatter in the halo concentration leads to variations in core density directly (Kaplinghat et al., 2016). Secondly, the self-interactions thermalize the inner halo with its central dark matter density *dependent* upon the baryonic extent. In dark matter dominated galaxies, a dense core forms whose density is determined by the self-interaction cross-section and the halo mass. With a cored profile, the features in the baryon distribution are more prominently reflected in the rotation curves. In contrast, in galaxies where the baryon component dominates the potential, the thermalization process lead to a denser central core with sizes influenced by the baryonic scale radius (Kaplinghat et al., 2014). Analytical calculations to address the diversity problem have been carried out by Kamada et al. (2017) using isothermal approximations to the effects of SIDM with a baryonic potential in order to construct fits for a diverse range of individual spiral galaxies.

In this work we explore the combined effects of SIDM and baryonic potentials by performing a series of numerical experiments. Our focus is on global trends but we include a pair of individual fits to test our results on the strongest outliers from observations. We sample a realistic range of concentrations and halo masses taken from cosmological simulations together with observed trends in the mass-size relation of galaxies. Our numerical approach and the analytical one presented in Kamada et al. (2017) complement each other in addressing the diversity problem in the SIDM model. The structure of this paper is as follows. In Section 2.2 we introduce in detail our simulations. Sections. 2.3.1 and 2.3.2 explore the diversity problem for a large sample of halos with $V_{\rm max} = [30\text{-}250]$ km s^{-1} with the latter including the effect of baryons. In

Sec. 2.3.3 we confirm that we can find rotation curves that are reasonable matches to a pair of extreme (one cusp-like and one core-like) observed rotation curves. In Sec. 2.4 we summarise and conclude.

2.2 Numerical simulations

We use a combination of N-body simulations and analytical tools to study the mass profile of galaxies within the SIDM framework including the effects driven by their baryons. The main focus of this work is on disk dominated galaxies, which we model with a disk component embedded within a massive and more extended dark matter halo (i.e. no bulge). For the N-body simulations we must produce discretised initial conditions which we describe for the halo in Section 2.2.2 in addition to the baryonic potential in 2.2.3. We evolve these initial conditions with and without the effect of a baryonic disk and also with and without self-interaction terms using the simulation code described in Section 2.2.1.

2.2.1 N-body code

We use the AREPO code Springel (2010) with the modifications of Vogelsberger et al. (2012) and Vogelsberger et al. (2016) to account for dark matter self-interactions. This methodology uses a Monte-Carlo approach to model the scattering of dark matter via the probabilistic scattering of the macroscopic dark matter particles in the simulation, where the density distribution due to an individual particle is smoothed over some kernel which extends over the k-nearest neighbours. Such an explicit method requires a time step limit $\Delta t_{\rm sidm}$ such that only $\lesssim$1 scattering can occur per particle per timestep. Notably in the cusp region of an NFW halo (i.e. $\rho \sim r^{-1}$ as $r \to 0$) as one moves towards the centre one finds that $\Delta t_{\rm sidm} \propto \frac{1}{\rho\sigma} \sim r^{\frac{1}{2}}$ (with σ the velocity dispersion), i.e the centre of the halo is so dynamically cold and dense that the mean-free path is below the particle separation. To avoid such small time steps one additionally needs to limit them to a small fraction of the acceleration time step.

We have modified this code to include a baryonic potential of a Miyamoto-Nagai (hereafter MN) disk (Section 2.2.3) and used a constant self-interaction cross-section for scattering, which is a good approximation in the dark matter low velocity limit, e.g., $v \lesssim 400$ km s^{-1} as shown in Fig. 1 of Kaplinghat et al. (2016).

In our calculations we assume a Hubble constant $H_0 = 70$ km s^{-1} Mpc^{-1}. Our simulation period is fixed at 10 Gyr, slightly shorter than the Hubble time ($H_0^{-1} \approx 13.96$ Gyr) in order to account, in an approximate way, for the assembly time of such galactic disks. It should be emphasised that isolated simulations with a static disk potential is well-motivated in the SIDM model; for $\sigma_{\rm T}/m_\chi \gtrsim 1$ cm^2/g, dark matter self-interactions occur multiple times in the inner halo over the age of galaxies, which drive thermalization of the inner halo in the presence of the stellar disk, and as such the final inner SIDM halo profile is more robust to changes in the formation history (given a known baryon distribution) than that of CDM.

2.2.2 Isolated halo initial conditions

For each of our galaxies, we generate a large set of compound galaxies consisting of an exponential disk embedded in a dark matter halo using the code MAKEDISK (Hernquist, 1993; Springel et al., 2005). The systems are set up in near equilibrium by requiring a joint solution to the combined phase space of both disk and halo component. In particular, the density profile of the halo is set up with a Hernquist (1990) density profile:

$$\rho_{\rm dm}(r) = \frac{M_{\rm dm} r_{\rm hq}}{2\pi r \left(r + r_{\rm hq}\right)^3}, \tag{2.1}$$

with $r_{\rm hq}$ the scale radius of the halo. Hernquist (1990) profiles show a r^{-1} slope in the inner density profile and r^{-4} in the outskirts, in close agreement with the inner/outer slopes of -1 and -3, respectively, of the cosmologically inspired NFW profiles (Navarro et al., 1997). The Hernquist profile has the extra advantage of having an analytic expression for its distribution function, which facilitates the process of setting up the initial conditions.

Hernquist halos can be "scaled" to match a given NFW profile quite closely and we therefore report our results in terms of virial mass[1] M_{200} and concentration parameter c corresponding to NFW halos. Finding the equivalent halo (by matching the dark matter mass within r_{200} and the asymptotic density profile as $r \to 0$) gives the relation between parameters

$$M_{\rm dm} = M_{200} - M_{\rm d} \tag{2.2}$$

$$r_{\rm hq} = \left(\frac{GM_{200}}{100H_0^2}\right)^{1/3} c^{-1}\sqrt{2\ln(1+c) - \frac{2c}{1+c}} \tag{2.3}$$

dependent upon the baryonic component $M_{\rm d}$ and the redshift zero Hubble constant H_0.

The matching of the internal regions of our Hernquist profile to the desired NFW is less accurate as we move close to the scale radius of the NFW $r_{\rm s}$, with the density of a Hernquist halo falling off more steeply beyond that point. In terms of the velocity dispersion profile, the Hernquist halo has a peak velocity dispersion shell that is more compact and this velocity dispersion is lower than the NFW value. This can affect the heat exchange, which stops once the isothermal core has been established. As a consequence of the lower velocity dispersion peak, Hernquist profiles can be more prone to the so called "core collapse" phenomena, or the runaway collapse in the inner regions that ultimately reverses the process of mass scattering away from the core and condenses instead more mass in the inner regions. This process would be exacerbated by the presence of baryons and as $\sigma_{\rm T}/m_\chi$ increases.

We have extensively tested this scenario and we include some comparisons in Appendix 2.5.2. We find that it makes a negligible difference in most of our simulations except for extreme cases with concentrated halos, however as we shall see later it is the *low* concentration halos where most of the interesting discrepancy between CDM and SIDM predictions lie, i.e. these halos are expected to host the low central (dark matter) density galaxies that are most challenging to CDM. As such our approach of using Hernquist halos is conservative, as the effect will be small and any deviations will cause us to underestimate our conclusions.

For the simulations showed in Sec. 5.3, we set up our halos using $n_p = 10^5$ particles to

[1] Virial quantities are defined at the virial radius r_{200}, where the enclosed density is 200 times the critical density of the Universe.

model the dark matter distribution, which results in a spread for the mass per particle $m_p = 8.97 \times 10^4$–2.66×10^7 $M_\odot$ according to the mass of the simulated halo. We use a gravitational softening length $\epsilon = 50$ pc, and we have tested for numerical convergence using a halo with $M_{200} = 1.1 \times 10^{11}$ $M_\odot$ and increasing/decreasing the particle number by a factor 10 with respect to our fiducial runs and find agreement within 10% in the (dark matter only) circular velocity profiles (and by proxy mass) for all radii outside 1.0 kpc.

2.2.3 Disk potential

The baryonic component of our galaxies is modelled by a fixed disk potential, which is not only computationally cheaper, but also allows us to maintain full control on the exact distribution of the baryons. This is particularly important for dwarf galaxies which undergo hundreds of orbits over a Hubble time and are thus particularly sensitive to (unphysical) discretisation-induced instabilities. We therefore strip the disk particles created in our initial conditions, and use instead an extra component in the gravitational force that accounts for the removed disk particles. This approach is not fully self-consistent since it ignores the back-reaction of the halo onto the baryons, but it provides a useful tool to explore the evolution of halo potentials in SIDM in a set of controlled experiments where the *final* baryonic distribution is known.

We implemented a static potential in AREPO following a Miyamoto and Nagai (1975) disk:

$$\Phi_{\rm MN}(R,z) = \frac{-GM_{\rm d}}{\sqrt{R^2 + \left(R_{\rm d} + \sqrt{{z_{\rm d}}^2 + z^2}\right)^2}}\,, \tag{2.4}$$

for a disk of mass $M_{\rm d}$ and scale radius $R_{\rm d}$ and we keep the disk relatively thick in all cases by setting $z_{\rm d}/R_{\rm d} = 0.3$ (appropriate to model dwarf irregular galaxies). Note that the half-mass radius of the flat ($z_{\rm d} = 0$) MN disk is $\sqrt{3}R_{\rm d}$ which is very close to the ratio of half-mass to scale radius of an exponential disk of 1.678 and so unless ones disk is extremely thick, the scale radius of an exponential fit will be within a few percent[2]. From here on we will use $R_{\rm d}$ interchangeably

[2] The differences are much more pronounced in the tails of the distribution, indeed one cannot choose to correspond a flat exponential to a MN density profile via for example the mass weighted root-mean square radii since for the latter that is a divergent quantity.

to refer to either the scale length of our baryonic disks in simulations (the MN scale radius) or the exponential disks associated with observed late-type dwarf galaxies.

Notice that the initial conditions are created assuming an exponential profile while the fixed potential uses an MN model for the disk. We have tested that this small inconsistency does not affect our results. Due to the diffusive nature of SIDM the resulting deviations due to non-equilibria are of the order of a few percent and quickly damped. Alternative approaches include that of Elbert et al. (2018) where the MN disk is 'grown' adiabatically (compared to the orbital timescale) from an initially halo-only setup. We have tested the extreme case of inserting the fixed potential instantaneously and find that after 10 Gyr evolution in SIDM at 2 kpc this makes a relative difference in the $V_{2\,\mathrm{kpc}}$ of $-0.2\,\mathrm{km\,s^{-1}}$ or 0.6%. Our method, being closer to equilibrium, is expected to be lower than these bounds.

We run the simulations for 10 Gyr and compute the circular velocity profiles. For the CDM cases this is in the most part a straightforward numerical test since the initial conditions are created in equilibrium and we do not see significant evolution of the mass distribution with time. For the most extended disks ($R_\mathrm{d} = 6$ kpc), however, the centre-of-mass is not well 'tied' to the centre of the (shallow) baryonic potential, and the centre-of-mass can 'drift' on the order of a kpc over 10 Gyr (i.e. an average of $0.1\,\mathrm{km\,s^{-1}}$) from the centre of the baryonic disk potential, making the assessment of the mass distribution within 2 kpc problematic. This evolution is expected due to discretisation of ICs and asymmetry in tree-based gravitational methods, and is relatively hard to suppress even with a tight timestep criteria. This process can of course also occur to the SIDM halos, although it is somewhat suppressed since their profiles have less compact centres. Since evolving CDM halos in extreme cases is somewhat tangential to the purpose of this paper, however, we have tested the CDM evolution on the more compact ($R_\mathrm{d} = 0.5$ and 1.5 kpc) halos, whose $V_{2\,\mathrm{kpc}}$ evolve by an average of -7.7% over 10 Gyr. For the $R_\mathrm{d} = 6$ kpc CDM halos we will use the initial conditions, as we believe those to be more accurate.

V_{200} ($\mathrm{km\,s^{-1}}$)	M_{200} ($\mathrm{M_\odot}$)	concentration (-2σ,median,$+2\sigma$)	r_s (kpc) -2σ,med.,$+2\sigma$	ρ_s ($10^6\,\mathrm{M_\odot\,kpc^{-3}}$)* -2σ,med.,$+2\sigma$	$\mathrm{M_d}$ ($\mathrm{M_\odot}$)	med. R_d (kpc**)
15	1.12×10^9	9.99, 15.60, 24.38	2.15, 1.37, 0.88	6.07, 18.42, 57.80	†	†
30	8.97×10^9	8.32, 12.99, 20.30	5.15, 3.30, 2.11	3.89, 11.63, 36.04	1.71×10^8	(1.93)
50	4.15×10^{10}	7.27, 11.36, 17.74	9.83, 6.29, 4.03	2.82, 8.32, 25.52	8.84×10^8	(2.53)
70	1.14×10^{11}	6.65, 10.39, 16.23	15.04, 9.62, 6.16	2.29, 6.69, 20.36	2.79×10^9	(3.03)
100	3.32×10^{11}	6.05, 9.46, 14.78	23.60, 15.11, 9.67	1.84, 5.31, 16.05	1.09×10^{10}	(3.60)
150	1.12×10^{12}	5.44, 8.50, 13.28	39.41, 25.22, 16.14	1.43, 4.10, 12.27	3.72×10^{10}	(4.09)
200	2.66×10^{12}	5.04, 7.88, 12.30	56.69, 36.28, 23.22	1.20, 3.42, 10.15	6.22×10^{10}	(4.53)

Table 2.1: Parameters for the halos used in our diversity analysis. V_{200} and M_{200}, concentrations with $\pm2\sigma$ relative to the median relation from Ludlow et al. (2014), and in NFW parameters we give the scale radius r_s and density ρ_s for this range of concentrations. For the simulations where we include a baryonic disk, $\mathrm{M_d}$ refers to the total baryonic disk mass.
* NFW density ρ_s is computed in the dark matter-only halo case. For the simulations with baryonic disks we fix M_{200} but add a baryonic component, and thus ρ_s is multiplied by the dark fraction $M_{\rm dm}/M_{200}$.
** We quote median baryonic disk radii only for reference, since we attempt to span the distribution with 0.5-6 kpc as described in the main text.
† This halo was simulated in DM-only.

2.3 Results

2.3.1 Circular velocity profiles in dark matter only halos

To illustrate the effect of dark matter self-interactions on the density profile of a dwarf halo without the influence of baryons, we use the analytical Jeans method proposed in (Kaplinghat et al., 2014, 2016) and tested against simulations in (Rocha et al., 2013; Elbert et al., 2015). We have further checked that its accuracy is within 10–20% compared to the results from our N-body code (Vogelsberger et al., 2012). The details of the formalism can be found in Appendix 2.5.1.

Our suite of halos aims to span the 'dwarf' galaxy distribution with 7 halos of V_{200} from 15-200 $\mathrm{km\,s^{-1}}$, the upper limit being near Milky Way-like (where velocity dependent corrections may play some role) down to dwarfs so baryon-poor that we expect negligible deviations from the DM-only results. To encompass the diversity in concentrations we sample $\pm2\sigma$ deviations from the cosmological mass-concentration relation presented in Ludlow et al. (2014), whose

median is well approximated by the linear fit

$$c = 10.51 \times \left(\frac{M_{200}}{10^{11}\,\mathrm{M}_\odot} \right)^{-0.088}, \tag{2.5}$$

and at each halo mass the distribution is approximately log-normal where 1σ corresponds to a ratio of ≈ 1.25. The corresponding halo mass (M_{200}) and NFW r_s and ρ_s are given for the $70\,\mathrm{km\,s^{-1}\,Mpc^{-1}}$ cosmology in Table 3.1.

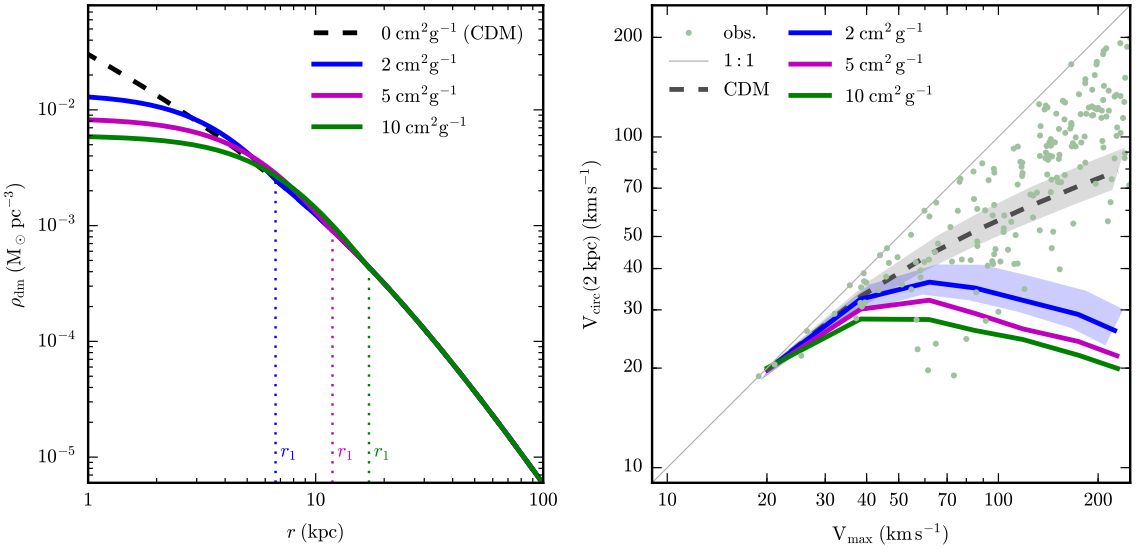

Figure 2.1: *Left panel:* core formation in a dark matter only halo (NFW) with different σ_T/m_χ. Dark matter density profile evolution for SIDM over 10 Gyr in *blue*, *magenta* and *green* for $\sigma_\mathrm{T}/m_\chi = 2$, 5 and 10 $\mathrm{cm^2\,g^{-1}}$ respectively, with CDM ($\sigma_\mathrm{T}/m_\chi = 0$ $\mathrm{cm^2\,g^{-1}}$) in *black dashed*. *Vertical dotted lines* indicate r_1 (the radius of unit scattering). *Right panel:* effects of SIDM on the $V_{2\,\mathrm{kpc}}$ vs V_max relation compared to CDM for dark matter onlyhalos. *Black line* is the CDM case, *blue* the $\sigma_\mathrm{T}/m_\chi = 2$ $\mathrm{cm^2\,g^{-1}}$ where the shaded regions denote $\pm 1\,\sigma$ scatter (due to halo concentrations; we have interpolated the values from the $\pm 2\sigma$ runs in Table 3.1). *Magenta* and *green* denote $\sigma_\mathrm{T}/m_\chi = 5$ $\mathrm{cm^2\,g^{-1}}$ and 10 $\mathrm{cm^2\,g^{-1}}$ respectively. *Green points* indicate observed values collated in Oman et al. (2015) Table 1, from which we also include the mass deficits, 5×10^8 and $10^9 \mathrm{M}_\odot$and their effect on $V_{2\,\mathrm{kpc}}$ in *blue shaded regions*.

The left panel of Fig. 2.1 shows the density profiles of a halo with $V_{200} = 70\,\mathrm{km\,s^{-1}}$ ($M_{200} = 1.1 \times 10^{11}$ $\mathrm{M}_\odot$) and a concentration $c = 6.65$ after 10 Gyr evolution with CDM ($\sigma_\mathrm{T}/m_\chi = 0$ $\mathrm{cm^2\,g^{-1}}$, black dashed line) vs. SIDM with $\sigma_\mathrm{T}/m_\chi = 2$, 5 and 10 $\mathrm{cm^2\,g^{-1}}$ (see solid lines according to labels). The radius of unit scattering, r_1 (see also Appendix 2.5.1) outside of which

the halo is undisturbed is marked for the three cases. This radius grows with cross-section, and in the interior we see all three cross-sections produce cores for this halo that extend beyond 2 kpc.

Fig. 2.1 (right panel) shows the circular velocity of the SIDM halo profiles evaluated at 2 kpc as a function of $V_{\rm max}$. For the comparison, we also plot the corresponding CDM one with the mass-concentration relation from Ludlow et al. (2014) and the range spanned by a compilation of the observed rotation curves in galaxies taken from Oman et al. (2015). It is clear that $V_{2\,\rm kpc}$ increases steadily with $V_{\rm max}$ in the case with CDM, although the relation stays below the 1 : 1 line. In contrast, SIDM predicts a much shallower relation. $V_{2\,\rm kpc}$ is almost independent of $V_{\rm max}$ in the range explored, and the median $V_{2\,\rm kpc}$ value at a given $V_{\rm max}$ depends mildly on cross-section. For low mass halos (low circular velocity), $V_{\rm max}$ tends to converge to near $V_{2\,\rm kpc}$, since the objects are small and the core size becomes much less than 2 kpc and $V_{\rm max}$ is measured near 2 kpc. It is interesting to note this is a common feature in CDM as well as SIDM halos. Shaded regions indicate $\pm1\sigma$ in concentration (we interpolate from the $\pm2\sigma$).

The range of $V_{2\,\rm kpc}$ and $V_{\rm max}$ statistics of the galaxy rotation curve distribution is shown in Fig. 2.1 (taken from Oman et al., 2015). The scatter found in the data is significantly larger than derived purely from that of concentration variations (in either CDM or SIDM). A large fraction of the observed $V_{2\,\rm kpc}$ scatter below the relation expected for CDM, suggesting that such objects have a lower dark matter density in the inner regions than predicted by the model. Instead, self-interactions seem to have the opposite behaviour, providing a better match to these low density objects but predicting too low a $V_{2\,\rm kpc}$ to explain most of the data. These calculations, however, ignore the contribution of the baryons, and as we argue below, the mass and radial extent of the gas and stars in galaxies may significantly change this prediction to bring SIDM in closer agreement with observations.

2.3.2 Circular velocity profiles in the presence of baryons

For collisionless dark matter halos, the presence of baryons may change the shape of the *total* circular velocity profile by adding the contribution from the gas and the stars. This contribution

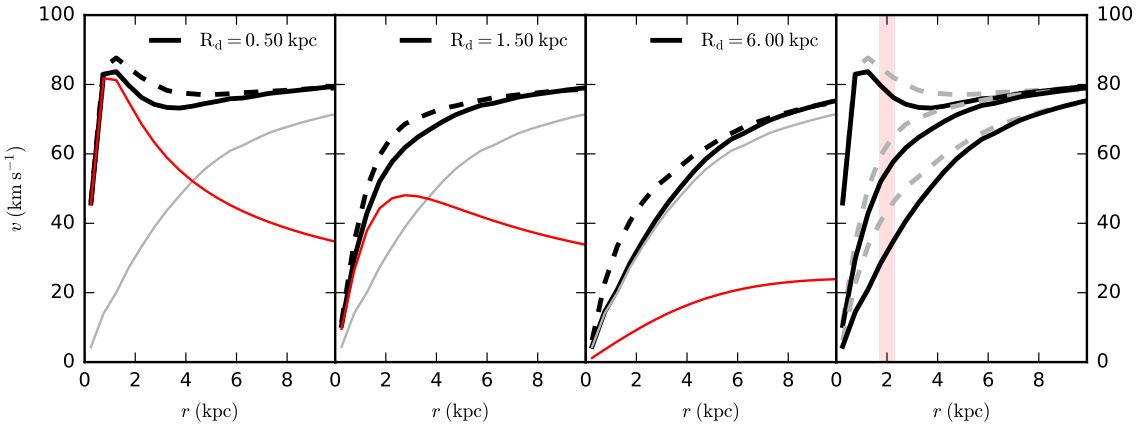

Figure 2.2: *Left three panels:* Dark matter contribution to the circular velocity profile for a dwarf galaxy ($V_{200} = 70$ km s^{-1}, $c = -2\sigma$) with a fixed baryonic disk component with scale radii 0.5, 1.5 and 6 kpc from left to right respectively, simulated for 10 Gyr with a cross-section $\sigma_T/m_\chi = 2$ cm^2 g^{-1}. *Red lines* indicate the baryonic contribution, *grey* the dark matter (SIDM), and *thick solid black* the total. For comparison, the *thick dashed black* lines indicate the CDM total. *Right panel* combines the three profiles, with the CDM comparisons in *grey dashed lines*.

may or may not change the overall profile, depending on the relative fraction of baryonic mass and also the spatial distribution of these baryons[3]. If gas and stars are very centrally concentrated, they will dominate the contribution to the circular velocity modifying the profile to rise more steeply than the original NFW halo. On the other hand, if the baryons are fairly extended, their contribution could be sub-dominant to the dark matter, in which case the total velocity profile including baryons does not deviate significantly from that of the original NFW halo.

Fig. 2.2 (leftmost three panels) illustrates this point using the N-body simulations set up described in Sec. 2.2. For a fixed halo with $V_{200} = 70$ km s^{-1}, $M_d = 2.8 \times 10^9$ M$_\odot$ (according to abundance matching relations from Behroozi et al. (2013)) and a concentration -2σ below the median. We plot the equivalent 'circular velocity' inferred for a spherically averaged mass distribution

$$V_{cir}^2 = GM(r)/r = V_{cir,dm}^2 + V_{cir,bar}^2 \tag{2.6}$$

which is an approximation for non-spherical distributions (for a pure thin MN disk without a

[3] Notice that baryons could additionally cause the dark halo to contract (Blumenthal et al., 1986), but given our initial condition set-up, the halos will be created already in equilibrium with the baryonic potential

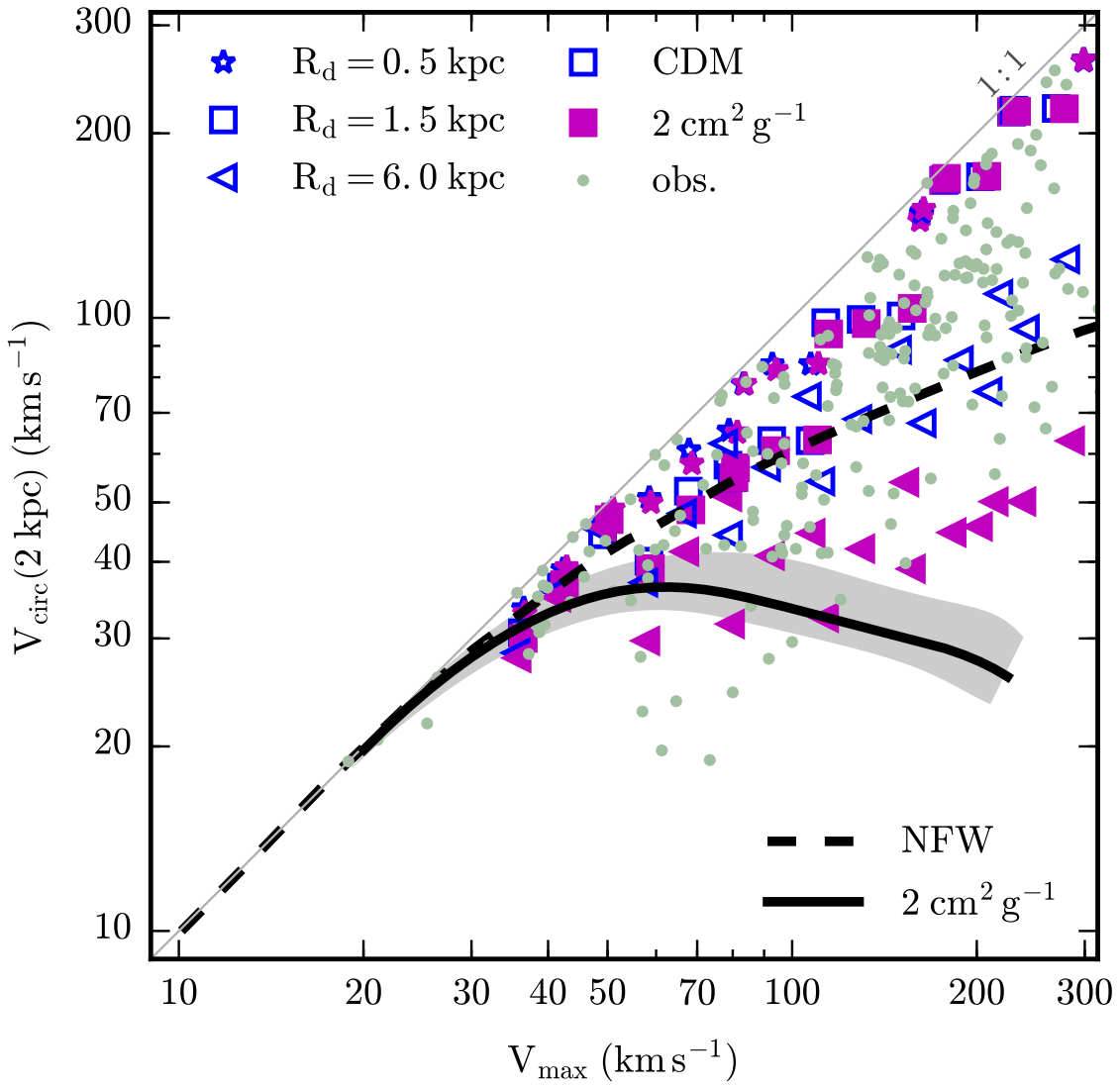

Figure 2.3: N-body simulations in the presence of galactic disks. *Left panel* shows the individual simulations with disk scale lengths R_d = 0.5, 1.5 and 6 kpc in *stars*, *squares* and *triangles* respectively, where each is repeated for the three different -2σ, median, and $+2\sigma$ concentrations and SIDM in *solid magenta* and CDM in *open blue symbols*. *Dashed black line* indicates the CDM relation without baryons, and *solid black* the corresponding SIDM (with $\pm1\sigma$ shading).

halo these deviations are at maximum $\approx$ 15%). We assume that the baryons distribute in a MN disk with scale length equivalent R_d = 0.5, 1.5 and 6 kpc (left to right). The long-dashed lines indicate the final profiles including the baryons for CDM, which show different shapes according to R_d, with the differences tracing back to the contribution of the baryons in each case.

As expected, a more concentrated baryonic distribution (small $R_{\rm d}$) shows a steep raise of the circular velocity curve, whereas larger $R_{\rm d}$ values grow more gently. The case with $R_{\rm d} = 0.5$ kpc results in a declining circular velocity profile which might not be the typical galaxy included in studies of rotation curves (probably representing a bulge dominated object instead). However, we include this case for illustration of the possible extremes and how CDM and SIDM would react to the presence of such a compact galaxy.

The same exercise of considering a fixed halo and baryonic content but changing the spatial distribution can be done assuming the SIDM scenario. The three left panels in Fig. 2.2 show the expected total profiles assuming a self-interaction cross-section $\sigma_{\rm T}/m_{\chi} = 2$ cm^2 g^{-1} (see solid black lines). The dark matter component still shows a cored profile due to the self-interactions (see thin grey line) but this is obscured in the *total* velocity profile. In fact, the inclusion of baryons creates a fair amount of *diversity* in the shapes of the circular velocity profiles for CDM and SIDM (see right panel in the same figure). For example, if we measure $V_{2\,\rm kpc}$ in these halos (vertical red shaded region), CDM covers a range $\approx 45-83$ km s^{-1} which is comparable to that spanned by SIDM, $V_{2\,\rm kpc} \approx 30-75$ km s^{-1}. Encouragingly, the effect of baryons in the case with self-interactions creates a wide range of (total) rotation curves but also maintains a lower central density (in the cases where baryons are extended), allowing better accommodation of the low $V_{2\,\rm kpc}$ values that are occur in observations (see right panel Fig. 2.1) and for which CDM alone has no explanation.

We generalise this by simulating all halos introduced in Sec. 2.3.1 but including a baryonic disk. The mass of the disk is the sum of a stellar and gaseous component, with the first set by the abundance matching relation between M_* and M_{200} introduced in Behroozi et al. (2013) and the gas mass computed from the $M_{\rm gas}$-$M_\star$ relations of Huang et al. (2012). To account for variations in halo concentration c, we sample three different halos of median and $\pm 2\sigma$ extremes according to the mass-concentration relation from Ludlow et al. (2014). Table 3.1 summarises the main properties of all our runs. Each halo is then set up in equilibrium with their baryonic MN disk of scale lengths $R_{\rm d} = 0.5,\ 1.5,$ and 6.0 kpc. We fix the scale height of the disks to $z_{\rm d} = 0.3R_{\rm d}$, a slightly hotter structure than for Milky-Way-like galaxies but that provides a

reasonable description of lower mass galaxies, the main target of this study.

We run our simulations for 10 Gyr assuming i) collisionless cold dark matter (CDM) and ii) a fiducial self-interaction cross-section $\sigma_{\rm T}/m_\chi = 2$ cm^2 g^{-1} for the SIDM case. We investigate the relation between $V_{\rm max}$ and $V_{2\,\rm kpc}$ of our halos in CDM and SIDM in the left panel of Fig. 2.3. Symbol shapes (square, star, triangle) indicate the different scale lengths sampled whereas open-blue and filled-magenta differentiate between CDM and SIDM runs. A quick inspection suggests that self-interactions are able to generate a wider range of $V_{2\,\rm kpc}$ at fixed $V_{\rm max}$ which is in better agreement with observed values from the compilation in Oman et al. (2015) (green dots). The diversity in both cases, CDM and SIDM, arises from different contribution by the baryons. Since SIDM cores imply a lower dark matter density in the inner regions, the contribution of baryons is *more* important that in the collisionless case, creating a larger variety in $V_{2\,\rm kpc}$. Notice that for the more compact disks ($R_{\rm d} = 0.5$ and 1.5 kpc) the predictions from CDM and SIDM are not that different, and in both cases $V_{2\,\rm kpc}$ can be very close to $V_{\rm max}$, which suggests these rotation curves are relatively flat. One should also note that in a cosmological context the central density would be even further promoted by the adiabatic contraction introduced by baryonic collapse (e.g. Elbert et al., 2018), which occurs even in the models with bursty feedback (Tollet et al., 2016). In the case with non-dominant baryonic components (triangles) the points stay close to the dark matter-only case (thin solid lines), which is significantly lower in the case of self-interactions, as discussed in Sec. 2.3.1.

The lower envelope of points in either scenario corresponds to the most extended disks populating the -2σ outliers in halo concentration. A few of the observed points in the left panel of Fig. 2.3 still remain unexplained ($V_{\rm max} \approx 70$ km s^{-1} and $V_{2\,\rm kpc} \approx 20$ km s^{-1}) showing central densities even lower than can be obtained in SIDM with $\sigma_{\rm T}/m_\chi = 2$ cm^2 g^{-1}. This could be suggesting the need for a larger cross section for self-interactions or more extreme outliers on the mass-concentration relation. We should also bear in mind the possibility of observational errors as discussed in Sec. 2.1.

We have probably overstated the extremity of these outliers since we have at zero-th order ignored correlations between halo and disk properties that would alleviate the tension. For

instance, if more compact disks systematically populate more concentrated halos whereas extended disks live in low concentration halos, the shaded areas could be larger. We have also not made an attempt to account for observational biases in these calculations. Regardless of the absolute value, however, we emphasise that at fixed assumptions, SIDM seems to always provide a larger range of diversity than CDM (with scatter at least 150% of the latter).

An interesting corollary of the analysis above is that, fixing the relation $V_{\rm max}$-$V_{2\,\rm kpc}$, a given halo in CDM and SIDM would be predicted to have different contribution from the baryons at 2 kpc, since in SIDM the baryonic matter will have to "compensate" for the lower density of the cored dark matter halo. It is therefore important to compare the dark matter fractions predicted in both models to check that they are consistent with observed galaxies. Fig. 2.4 shows the dark matter fractions $f_{\rm dm} = M_{\rm dm}/M_{\rm tot}$ measured at 2 kpc for our CDM and SIDM halos (open and filled symbols, respectively) compared to a subsample of galaxies taken from the rotation curves presented in (Oh et al., 2015) and Kuzio de Naray et al. (2008). For the former we use their disk-halo decomposition from the stellar, HI and kinematic data, and for Kuzio de Naray et al. (2008) we use their 'popsynth' mass modelling rather than the extremal fits. In a couple of cases the last-measured point does not reach 2 kpc and for these we used the dark matter fraction at the last measured point.

There is a significant overlap between the collisionless and the self-interacting scenarios. Also, spatial resolution coupled to uncertainties in the mass-to-light ratios for the observed objects makes $f_{\rm dm}$ probably not a good enough indicator to distinguish between these alternative models. Nonetheless, it is reassuring that the same SIDM objects that reproduce better the observations in the $V_{\rm max}$-$V_{2\,\rm kpc}$ plane, seem to have dark matter fractions that are consistent with current observations.

2.3.3 Two extreme examples: IC 2574 and UGC 5721

In Sec. 2.3.2, we presented a detailed statistical analysis of a sample of objects simulated within the SIDM paradigm. This, however, left unexplained one of the main motivations of this work, which is the existence of extreme outliers which are not possible to accommodate within the

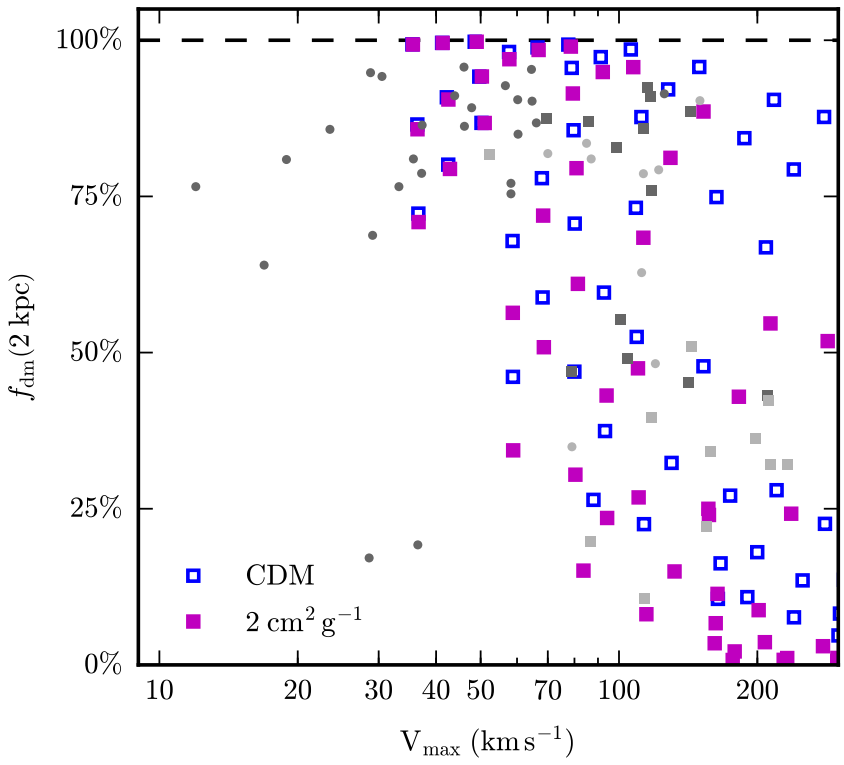

Figure 2.4: Dark matter contribution to the rotation curve at 2 kpc for SIDM simulations and observed dwarfs (see main text). *Filled magenta squares* are the SIDM simulations, in comparison to the CDM in *open blue squares*. *Greyscale symbols* refer to observed galaxies from (Oh et al., 2015) (*dark circles*), Kuzio de Naray et al. (2008) (*light circles*), de Blok et al. (2001) (*light squares*) and de Blok et al. (2008) (*dark squares*).

standard CDM scenario. We turn then our attention to two particular examples highlighted in Oman et al. (2015), UGC 5721 and IC 2574. These two galaxies have similar circular velocity measured at the outermost point of the rotation curve $\approx 80\ {\rm km\,s^{-1}}$, which probably indicate that they populate dark matter halos with similar mass, but the *shapes* of the inner regions are remarkably different: whereas UGC 5721 is consistent with a 'cuspy' NFW profile, IC 2574 has a very extended core. This pair is an interesting case of the aforementioned diversity and we can use it as benchmark for our SIDM scenario.

In Figs. 2.5 and 2.6 we show the data together with the best fit CDM (dashed line) and SIDM (solid black) curves. For UGC 5721 (NGC3724) we use the rotation curve data from Swaters et al. (2003) and stellar and gas densities from Andrew Pace (priv. communication, for

Property	Symbol	IC 2574	UGC 5721
Disk scale length	$R_{\rm d}$	3.0	0.50 kpc
Disk scale height	$z_{\rm d}$	0.9	0.15 kpc
Stellar mass	$M_\star$	3.00×10^8	4.48×10^8 $M_\odot$
Gas mass†	$M_{\rm gas}$	2.72×10^9	8.47×10^8 $M_\odot$
Halo mass	M_{200}	9.78×10^{10}	5.15×10^{10} $M_\odot$
Concentration	c	6.2 (-2.3σ)	13.6 ($+0.9\sigma$)
DM cross-section	$\sigma_{\rm T}/m_\chi$	3	3 cm^2 g^{-1}
NFW radius	$r_{\rm s}$	15.4	5.65 kpc
NFW density	$\rho_{\rm s}$	1.9×10^{-3}	$0.013\,M_\odot\,{\rm pc}^{-3}$

Table 2.2: Parameters for the SIDM halos and baryonic potentials for the two galaxies in Fig. 2.5 and 2.6.
† The gaseous component as added in post-processing due to its disturbed nature, see also main text in Sec. 2.3.3.

comparison one can see Fig. 1 in Swaters et al., 2010 which has a slightly higher mass-to-light ratio).

For IC 2574 we use the rotation curve, gas and stellar densities from Oh et al. (2011). We multiply the stellar velocity contribution by 0.5 (mass-to-light ratio lower by a factor 4), so the stellar contribution lies between that in Sanders and McGaugh (2002) and Oh et al. (2011). For both cases our SIDM halo is run using a cross section for self-interactions of $\sigma_{\rm T}/m_\chi = 3\,{\rm cm}^2\,{\rm g}^{-1}$ following Kamada et al. (2017).

Our fitting process relied upon making an initial guess for the halo mass using $V_{\rm max}$ and sampling the concentration with $\pm 2.5\sigma$ of the mass-concentration relation in Eqn. (2.5). The combined stellar plus gaseous disks in these dwarfs are not well represented by a single MN disk (especially their gas profiles which exhibit a much more extended, nearly constant surface density), however since these differences are primarily in the outer regions where we expect the effects of self-interactions to be sub-dominant, we chose to approximate only the *stellar* distribution with an MN disk and apply the gas contribution to the rotation curve in a post-processing step (i.e. add in quadrature as in Eqn. 2.6), and after several iterations with the disk component we find the parameters indicated in Table 2.2. As noted in Appendix 2.5.2, the initial conditions are constructed with Hernquist profiles converted from the corresponding

NFW parameters, but if one is using a real NFW then in the higher concentration case using a lower r_s would give a slightly better match.

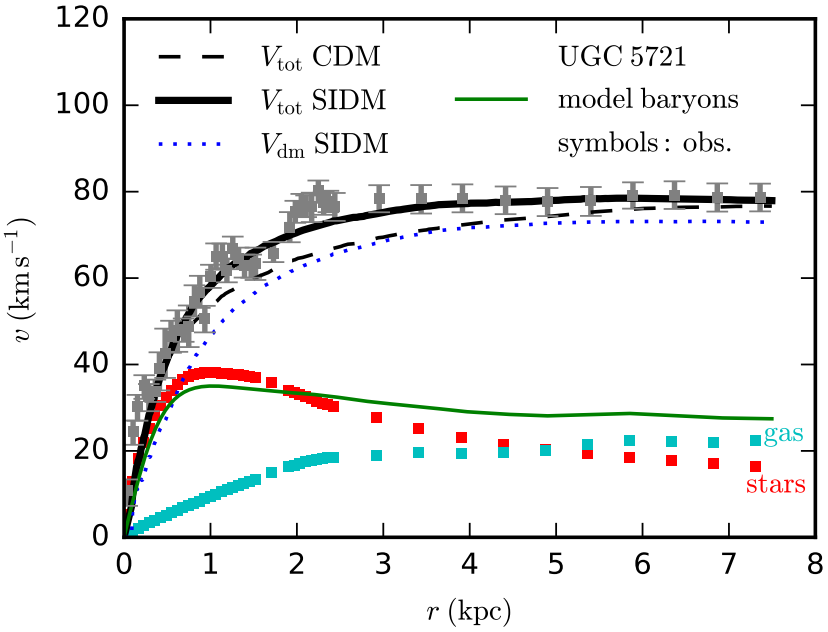

Figure 2.5: Observations for UGC 5721 along with SIDM and CDM simulations. *Red points* indicate the stellar contribution, *cyan* the gas and *grey squares with error bars* the observed rotation curve. The SIDM simulation (with parameters from Table 2.2) has the baryonic mass contribution indicated by the *green line*, which is a composition of the interpolated gas distribution along with an MN fit to the stellar disk. The halo contribution is given in the *dotted blue line* and the total curve in *solid black*. The comparison curve for CDM is given in the *dashed black line*.

Fig. 2.5 shows that the SIDM fit for UGC 5721 including all components has an overall "cuspy" profile (see black solid line), which is *steeper* than the circular velocity expected for the corresponding NFW halo without self-interactions (dashed line). For this fit we need a concentrated halo at $+1\sigma$ above the median mass-concentration relation, which together with the observed compact stellar disk (scale radius of 0.5 kpc) combine to create a steeply raising velocity curve. This is an excellent example of the importance of baryons in the shape of the rotation curves, even for dwarf galaxies. The χ^2/dof of the SIDM fit is 3.04 (4.44 below the initial, which is of course not the best individual CDM halo fit). The visual impression of a superior fit is likely due to This χ^2 is largely driven by the $\lesssim$0.3 kpc data with tight error bars

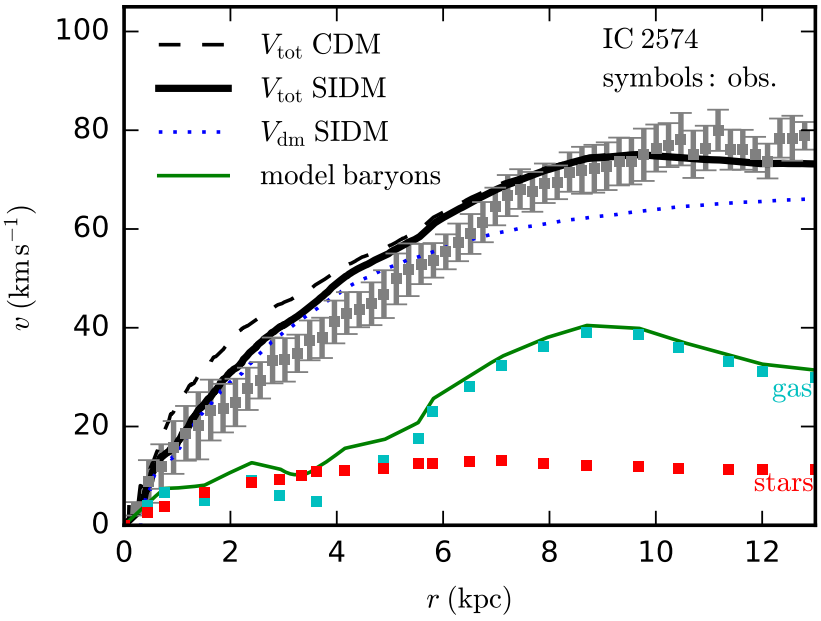

Figure 2.6: Observations for IC 2574 along with SIDM and CDM simulations. *Red points* indicate the stellar contribution, *cyan* the gas and *grey squares with error bars* the observed rotation curve. The SIDM simulation (with parameters from Table 2.2) has the baryonic mass contribution indicated by the *green line*, which is a composition of the interpolated gas distribution along with an MN fit to the stellar disk. The halo contribution is given in the *dotted blue line* and the total curve in *solid black*. The comparison curve for CDM is given in the *dashed black line.*

over a non-monotonic feature, contributing to a visually impression of a superior fit. Clearly a more accurate fit to such features would require additional parameters (particularly for the stellar components), however this is outside the scope of this paper. Without the presence of baryons, UGC 5721 is a challenge for SIDM due to the development of an extended low density core at the centre. In our simulations, however, the SIDM thermal transfer in cooperation with the baryon dominance in the central 1.5 kpc causes the halo to shrink even further than the pure NFW model. The compact stellar component excavates a potential well sufficient that thermalisation of the dark component leads to an almost-NFW final configuration (see also Kamada et al., 2017).

On the other hand, Fig. 2.6 presents the rotation curve fit for IC 2574 with an extended and slowly rising core in its centre. The gas has a disturbed profile, but the baryons as a whole contribute little to the total density except within the innermost 0.5 kpc, and make a modest

contribution at $r > 6$ kpc. For such a dark matter dominated galaxy to deviate so far from a cusp-like profile is clearly a challenge for vanilla CDM (Blais-Ouellette et al., 2001; Sanders and McGaugh, 2002; Swaters et al., 2003, 2010). Notice that any baryonic solution to this problem within CDM – for instance assuming that supernova feedback can create a core– would not work for such object, since the core extends well beyond where the stars are (see discussion in Oman et al. 2015). The χ^2/dof of the SIDM fit is 1.57, (1.39 below the initial conditions), which reflects the introduction of the core and quantifies the capacity of SIDM as a solution to this conundrum.

Whilst SIDM is relatively efficient in producing cores, this process becomes increasingly sedate as the core size approaches the scale radius of the halo (in this case 15.4 kpc) and so we have had to choose a relatively large scale radius (i.e. low concentration) halo. The $V_{2\,\mathrm{kpc}}$ of our CDM halo is around 35 $\mathrm{km\,s^{-1}}$ whilst in SIDM it is around 27 $\mathrm{km\,s^{-1}}$, bringing it in better agreement with the observed rotation curve $V_{2\,\mathrm{kpc}} \approx 23\ \mathrm{km\,s^{-1}}$.

We note that for IC 2574 both the low concentration and self-interactions are required to achieve a good fit. As such one way to test our model is to perform a statistical study of extreme outliers like IC 2574. Since we assume the SIDM model inherits the halo mass-concentration relation of the CDM one, such a study also provides a direct test for ΛCDM on galactic scales.

We have shown that the SIDM model in the presence of baryons can provide good fits to two extreme outliers. We demonstrate that with SIDM the halo concentration, the baryon concentration and the back-reaction of baryons on the density profile play roles in explaining the rotation curves of these two extremes. SIDM halo profiles are flexible enough to accommodate the diverse rotation curves of spiral galaxies.

2.4 Summary

The SIDM model modifies the CDM paradigm by inclusion of non-gravitational interactions between dark matter particles in the halo evolution, and these self-interaction effects are most significant in the regions of halos with the high densities and velocity dispersions, i.e. within

the scale radius of the halo. In the outer halo and at large scales SIDM is almost collisionless and retains the successes of ΛCDM. In the inner regions of halos the dark matter is redistributed into a central core, whose density and size depend on the microscopic particle interaction cross-section, the halo mass and even the baryon concentration. The mass profiles inferred from astronomical observations of the rotation curves of spiral galaxies thus offer an avenue to both constrain the self-interaction cross-section of dark matter and falsify or support specific self-interaction models.

Observationally, the shapes of the rotation curves of galaxies exhibit a wide diversity. We follow Oman et al. (2015) by quantifying the range in the rotation curves using the relation between the total circular velocity measured within 2 kpc and at the peak, $V_{2\,\mathrm{kpc}}$–V_{max}. For a given V_{max}, the spread in $V_{2\,\mathrm{kpc}}$ can be a factor of four, which is difficult to reconcile in the prevailing ΛCDM paradigm (Oman et al., 2015), where dark matter is assumed to be collisionless over the cosmological timescale. This problem stems from the hierarchical structure formation in ΛCDM which produces a self-similar halo density profile, which is essentially parameterised by one parameter, the halo mass (or concentration). After we determine the halo mass by V_{max}, the halo circular velocity is completely fixed at all radii, up to the scatter, including the inner density cusp that is in contrast to the shallow (cored) one preferred by many dwarf galaxies. In addition, the enclosed mass of a CDM halo cusp tends to overwhelm the baryonic contribution and consequently also the scatter in $V_{2\,\mathrm{kpc}}$ caused by the spread in the baryon concentration. This inflexibility in CDM may be alleviated by introducing particular prescriptions of baryonic feedback processes that can dynamically heat the dark matter (Navarro et al., 1996; Pontzen and Governato, 2012, and others), however SIDM offers an attractive alternative solution.

In this paper we have used controlled N-body simulations as a numerical experiment to test the SIDM model's ability to address the diversity problem. We use the AREPO code to run isolated simulations of a live halo in the presence of a static baryonic disk in order to assess the gravitational impact of gas and stars on the halo evolution. This approach is suited to the SIDM model as dark matter self-interactions thermalise the inner halo and the final (inner) density profile is largely insensitive to the formation history. We sample a wide range of halo masses

spanning about three orders of magnitude and vary the halo concentration within $\pm 2\sigma$ from the its mean value. For each halo mass, we use abundance matching relations to choose the disk mass and we take three disk scale radii to span the baryon distributions. This sampling of the model parameter domain enables us to make concrete predictions of the rotation curves in the SIDM model.

Our main conclusion (see Fig. 2.3) is that the SIDM mechanism accommodates galaxies with a wide range of $V_{2\,\mathrm{kpc}}$ over the domain of V_{max} from 30–250 $\mathrm{km\,s^{-1}}$. The spread in core densities is due in part to the variance in concentration (within $\pm 2\sigma$ from the mean), however this alone is insufficient to account for the large relative scatter of the observed values. Including self-interactions allows lower $V_{2\,\mathrm{kpc}}$, which requires low central densities in *both* baryons and dark matter. High values of $V_{2\,\mathrm{kpc}}$ are still achieved with compact baryonic disks where thermalisation into the deep baryonic potentials can induce NFW-like densities. As a result the predicted range of $V_{2\,\mathrm{kpc}}$ for a fixed V_{max} in SIDM is 50% larger than the CDM one, leading to a better agreement with the observed rotation curve distribution.

Some observed galaxies in the range $V_{\mathrm{max}} = 60$–80 $\mathrm{km\,s^{-1}}$ and $V_{2\,\mathrm{kpc}} = 20$–30 $\mathrm{km\,s^{-1}}$ are still challenging. These cases might require assumptions about the structure of the copula of the combination of halo concentrations and baryonic disk sizes, in particular that very extended disks populate the most under-concentrated halos to reproduce the very low $V_{2\,\mathrm{kpc}}$, which is not an unrealistic assumption to first order. Nevertheless, the SIDM prediction is an improvement over CDM in all cases.

To further test our results, we have performed simulations to provide individual fits for two of the most extreme outliers highlighted in Oman et al. (2015), UGC 5721 and IC 2574, cusp- and core- dominated galaxies respectively, both with similar $V_{\mathrm{max}} \approx 80$ $\mathrm{km\,s^{-1}}$ (see Figs. 2.5 and 2.6). Picking extreme $+0.9\sigma$ and -2.3σ concentrations from the halo concentration-mass relation, together with a compact $R_{\mathrm{d}} = 0.5$ kpc and extended $R_{\mathrm{d}} = 3.0$ kpc baryonic distribution respectively, we find good fits in the SIDM paradigm. Interestingly, we find that the SIDM density profile can be as dense as the NFW one in a baryon-concentrated galaxy such as UGC 5721, because SIDM particles follow an isothermal distribution within the deep baryon potential. Our

simulation result confirms the theoretical expectation first predicted in Kaplinghat et al. (2014). At the other extreme, IC 2574 with an inferred central dark matter dominated core is more straightforwardly tractable with a model that allows dark matter thermalisation, and is more challenging to the collisionless CDM model.

The implication of these elements is that with the inclusion of realistic baryonic components, SIDM models can produce quantitatively superior fits to rotation curves, both at the level of individual rotation curves and over the statistical distribution of a quantitative measure of their shapes. As one would expect, fitting the most extreme outliers requires an interplay between the combinations of halo concentration, the baryon distribution, and the influence of baryons on the SIDM halo profiles. The results from our numerical experiments fit well with the previous theoretical calculations of Kamada et al. (2017).

A number of avenues for future research are apparent. On the observational side, more detailed observations for mass modelling would allow tighter constraints on the dark matter distribution and consequently the interaction cross-section. Orthogonally, larger sample sizes would allow the $V_{2\,\mathrm{kpc}}$–V_{max} distribution to better discriminate between CDM and SIDM. On the computational side, we have ignored the effects of the hierarchical assembly of dark matter halos. Whilst this is not expected to play a large role in the inner halo, it will nevertheless introduce additional scatter as a function of assembly time. Finally, all these will likely show strong correlations with the baryonic statistics, and investigations of galaxy formation in SIDM using full hydrodynamical cosmological simulations with the baryonic feedback processes are already being explored (e.g. Vogelsberger et al., 2014a; Fry et al., 2015).

2.5 Appendix

2.5.1 Jeans analysis

In order to accelerate the analysis of the spherically symmetric cases we have employed 'Jeans analysis' (Kaplinghat et al., 2016) which gives a very good approximation to the final density distribution of halo-like systems. For the benefit of the astrophysics reader we discuss the self-

similar evolution of the dark matter only case here, for more complex cases one should consult the aforementioned reference.

For the spherically-symmetric dark matter only case, the distribution function of dark matter can be written as $f(r, v_{\parallel}, v_{\perp})$ with density $\rho_{\rm ini}(r)$. An approximation to the effects of self-interaction, referred to as Jeans analysis, is to assume that those regions of the halo with $\lesssim 1$ scattering over the evolution are unperturbed, whilst those with $\gtrsim 1$ have become fully collisional (i.e. act as an ideal gas) and isothermal (i.e. erased any thermal gradient). Whilst this approximation may seem relatively severe, one should recall that a dark matter halo encompasses many orders of magnitude in density and velocity dispersion, and so the majority of the volume is either highly collisional or nearly collisionless. Finding the radius r_1 at which approximately 1 scattering per evolution time T occurs is determined implicitly via

$$\frac{\langle \sigma_{\rm T} v \rangle}{m_\chi} \rho_{\rm ini}(r_1)\, T = 1\,, \tag{2.7}$$

and subsequently the evolved profile (assuming $f_{\rm ini}$ was a stationary state) is the piecewise solution

$$\rho(r) = \begin{cases} \rho_{\rm iso}(r) & r < r_1 \\ \rho_{\rm ini}(r) & r \geq r_1 \end{cases} \tag{2.8}$$

where $\rho_{\rm iso}(r)$ is the isothermal solution to the Jeans equation (see below) with $\rho_{\rm iso} \to$ a constant as $r \to 0$ that matches the density and mass enclosed ρ_1 and M_1 at r_1.

Solution for $\rho_{\rm iso}$

Consider Poisson's equation for an isothermal self gravitating spherically symmetric halo

$$\sigma_0^2 \nabla^2 \ln \rho = -4\pi G \rho \tag{2.9}$$

As a second order differential equation this has 2 unknowns, which extends to a third if we consider σ_0 (the velocity dispersion) to be unknown. If we know two values, e.g. ρ_1 and M_1

at some radius r_1, then we need an additional constraint, but this can be provided by choosing the 'cored' solution with $\rho \to$ a constant as $r \to 0$.

Denoting this constant ρ_c a good choice for similarity function turns out to be for the ratio of the mean enclosed density $\bar{\rho}$ to this, i.e. $\theta = \frac{\bar{\rho}}{\rho_c}$. Expanding the Taylor series about $r = 0$ tells us the leading order non-constant term is $O(r^2)$, i.e. w.l.o.g we can write $\theta \sim 1 - \frac{r^2}{r_c^2}$ (for some core size r_c) as $r \to 0$. This suggests the use of the dimensionless variable

$$\mu = \frac{r^2}{r_c^2}, \tag{2.10}$$

as a parameter for $\theta(\mu)$, and by substitution

$$\theta(0) = -\theta'(0) = 1 \tag{2.11}$$

where the prime denotes differentiation w.r.t. μ, and we have chosen r_c to satisfy

$$\sigma_0^2 = \frac{2\pi}{5} G r_c^2 \rho_c \,. \tag{2.12}$$

By substitution into Eqn. (2.9) we determine that $\theta(\mu)$ obeys the 2nd order nonlinear ODE

$$\theta = -\frac{3}{5} \frac{\mathrm{d}}{\mathrm{d}\mu} \ln\left(3\theta + 2\mu\theta'\right) . \tag{2.13}$$

We plot this function in the left panel of Fig. 2.7. In order to determine the density we may wish to tabulate θ along with the dimensionless density ratio function we will refer to as τ, determined from θ by

$$\tau(\mu) = \frac{\rho}{\bar{\rho}} = 1 + \frac{2\mu\theta'}{3\theta} \,. \tag{2.14}$$

which is monotonically decreasing.

Given some point r_1 at which we know the density ρ_1 and the mass enclosed M_1, then we

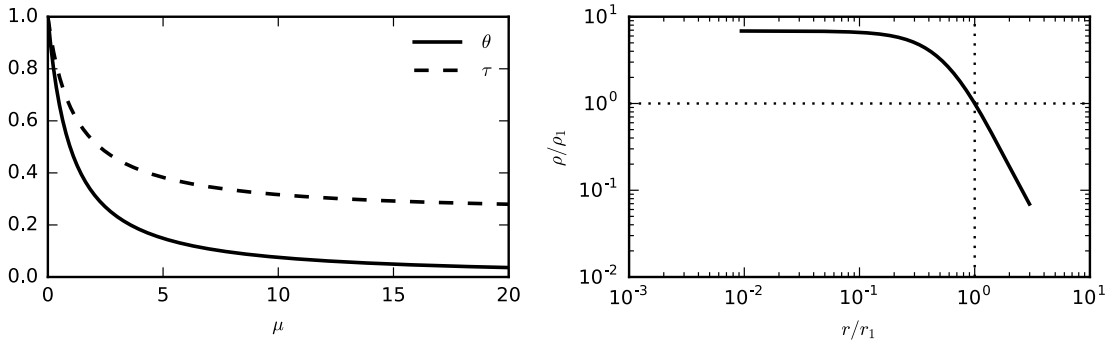

Figure 2.7: *Upper panel:* $\theta(\mu)$ and $\tau(\mu)$ functions. *Lower panel*, example Jeans solution for $\tau_1 = \frac{1}{2}$, i.e. at r_1 the density is half the mean density

know the mean density and can simply read off the μ_1 that gives us this τ_1, i.e.

$$\tau(\mu_1) = \tau_1 = \frac{4\pi r_1^3 \rho_1}{3M_1} \tag{2.15}$$

and then substitute to find the density at any $r < r_1$, i.e.

$$\rho_{\rm iso}(r) = \bar{\rho}\tau = \rho_1 \frac{\tau\left(\frac{\mu_1 r^2}{r_1^2}\right)}{\tau_1} \frac{\theta\left(\frac{\mu_1 r^2}{r_1^2}\right)}{\theta_1}\,. \tag{2.16}$$

and we plot an example in the right panel of Fig. 2.7

Scale dependence

Since the halos in cosmological simulations are self-similar, the features are broadly speaking common to all halo masses. In particular in Eqn. (2.7), for a fixed halo concentration (at all halo masses) the density $\rho_{\rm ini}(r/r_{200})$ is fixed, and so the scale dependent differences occur due to the increasing velocity dispersions and falling concentrations of larger halos. Increasing velocity dispersion increases the scattering rate and causes core formation to progress faster, whilst lower concentrations reduce the central densities, and consequently the scattering rate and core formation. Overall the velocity dispersion effect dominates and larger halos tend to grow their cores faster, up to some limit where velocity dependent cross-sections become important, although we do not discuss that case here.

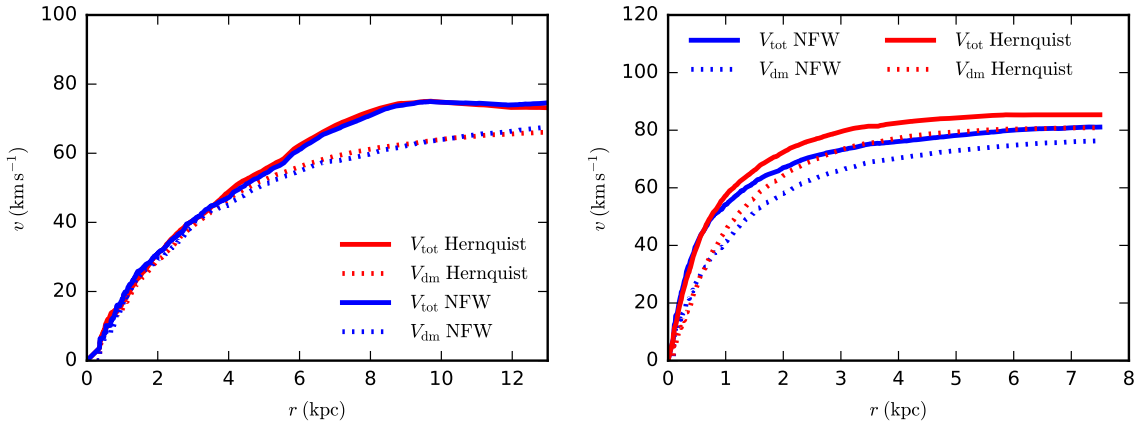

Figure 2.8: Comparison of the evolution of 'equivalent' Hernquist and NFW halos in the presence of baryonic disks. *Upper panel* is a low concentration halo very similar to our IC 2574 fit, whilst *lower panel* is high concentration setup similar to that of UGC 5721. The total rotation curves for the Hernquist halo are shown in *solid red* vs. the NFW in *solid blue*, with the dark matter contributions in *dotted lines* respectively.

2.5.2 NFW vs. Hernquist ICs

As mentioned in Section 2.2.2, the NFW and Hernquist initial conditions can evolve slightly differently in SIDM, driven by their velocity dispersion profiles (the NFW profile has somewhat increased velocity dispersion just beyond the scale radius r_s). In particular once the radius of unit scattering r_1 has saturated r_s, the Hernquist halo has slightly less 'heat' (i.e. velocity dispersion) for SIDM to transfer than NFW. Since halos in cosmological N-body simulations have profiles closer to NFW than to Hernquist, we wish to test whether there are systematic differences due to the use of Hernquist halos for our SIDM simulations.

In order to test this, we performed simulations similar to those of the IC 2574 and UGC 5721 cases (although not actually our final best-fits given in Table 2.2). We created NFW halos using the publicly available SPHERIC[4] code (Garrison-Kimmel et al., 2013) and equivalent Hernquist halos matched via Eqn. (2.3). Notably the mass distributions are not the same outside the scale radius r_s even in the ICs, so we do not expect perfect fits even ignoring the differences in velocity dispersion profiles. In Fig. 2.8 we have plotted the profiles after 10 Gyr of evolution with $\sigma_T/m_\chi = 3\ \mathrm{cm}^2\,\mathrm{g}^{-1}$ with the the dark matter contribution and the total rotation curves implied

[4] `https://bitbucket.org/migroch/spheric`

by a realistic baryonic contribution. One can see that for the low concentration halo (upper panel), the differences are truly negligible. On the other hand, for the higher concentration halo (lower panel, very similar to the $+0.9\sigma$ of UGC 5721), the extra velocity dispersion (and consequently larger core radius) of the evolved NFW case becomes apparent, albeit only at the level of $\approx 10\%$. From this we infer that the central densities from high concentration halos are overestimated with the Hernquist model, and if one wishes to use equivalent NFW halos one should increase the concentration (use a shorter r_s) by a few percentage points, including those parameters in Section 2.3.3.

Chapter 3

Impact of Dark Matter Self-Interactions On Milky Way-like Halos

3.1 Introduction

DM self-interactions kinematically thermalize the inner halo and lead to distinct features in the halo properties. For dwarf galaxies, where DM dominates over all radii, SIDM thermalization leads to a large density core, and the stellar distribution is more extended in SIDM than CDM and there is tight correlation between the DM core size and the stellar one (Vogelsberger et al., 2014b). Instead, for baryon-dominated systems, the thermalization can significantly increase the central SIDM density and the inner halo shape follows the baryonic distribution due to the influence of the baryonic potential (Kaplinghat et al., 2014), a radical deviation from SIDM-only simulations. Moreover, Kaplinghat et al. (2014) argued that once the inner halo reaches equilibrium the inner SIDM profile can be modeled as an isothermal distribution that is sensitive to the final baryonic potential, but not the formation history. This has motivated a number of isolated simulations to test the response of the SIDM halo to the baryonic potential (Elbert et al., 2018; Creasey et al., 2017), where they assumed a CDM halo and a stellar potential as the initial condition. Recently, Robertson et al. (2018b) performed cosmological hydrodynamical SIDM

simulations of galaxy clusters and explicitly confirmed this expectation. In addition, although in the presence of strong baryonic feedback both CDM and SIDM could lead to similar density profiles (Fry et al., 2015), the internal structure of the SIDM halo is more robust to the inclusion of baryonic feedback, compared to its CDM counterpart, due to the rapid energy redistribution caused by the DM collisions (Robles et al., 2017b).

In this chapter, we utilize isolated simulations to study the response of the SIDM halo in the presence of the baryonic potential for Milky Way (MW)-sized galaxies, where the baryonic contribution to the potential is important. Our goal is to understand the interplay between the DM self-scattering strength and the baryonic concentration in shaping the SIDM distribution, and the significance of the potential in altering evolution history of the SIDM halo. In the first two sets of simulations, we vary both the baryonic concentration and $\sigma_{\rm x}/m_{\rm x}$ in the range of 0.5–5 $\rm cm^2/g$, and study the variation of the SIDM predictions in the density profile and shape as a function of the cross section. In the presence of baryons, the central density of an SIDM halo no longer decreases monotonically with increasing $\sigma_{\rm x}/m_{\rm x}$, as expected in the SIDM-only case for $\sigma_{\rm x}/m_{\rm x}$ we take. Accordingly, the SIDM halo shape varies with $\sigma_{\rm x}/m_{\rm x}$ even for the same baryonic potential. Our results indicate that inferring $\sigma_{\rm x}/m_{\rm x}$ from stellar kinematics of luminous galaxies, where the baryons dominate the potential, could be challenging.

In our third set of simulations, we construct a realistic MW mass model, including an SIDM halo, a stellar bulge and disk. We fix $\sigma_{\rm x}/m_{\rm x} = 1$ $\rm cm^2/g$ and carefully adjust the model parameters to reproduce the mass model inferred from the stellar kinematics. We then make a detailed comparison between the halo shape predicted in our model and those inferred from observations.

The structure of this chapter is as follows. In Sec. 3.2, we discuss the numerical details of our simulations and the methodology used to quantify the halo shapes. In Sec. 3.3, we use our code to explore the evolution of a MW-sized halo with a stellar disk and measure the effect of the radial length scale of the disk. In Sec. 3.4, we compare our predictions for a SIDM MW halo against those from CDM simulations and those inferred from observations of stellar streams. We conclude and summarize our results in Sec. 3.5.

3.2 Simulations and halo shape algorithms

3.2.1 Numerical Simulations

We carry out N-body simulations using the code AREPO (Springel, 2010). Gravity modules in Arepo are a modified version of GADGET-2 and GADGET-3 (Springel, 2005). We use the algorithm developed in Vogelsberger et al. (2012, 2016) to model DM self-interactions. This is a Monte Carlo-based method, where at each time step a particle may pairwise scatter with any of its nearest neighbors. We assume a velocity-independent constant cross section in our simulations. This is a good approximation, since the observationally self-scattering cross section varies mildly across galactic scales (Kaplinghat et al., 2016) and we mainly focus on isolated simulations for a given halo mass. We evolve our simulations for 10 Gyr, slightly shorter than Hubble time scale ($H_0^{-1} \approx 13.96$ Gyr) in order to account for the assembly of the primordial galactic halo.

Following Creasey et al. (2017), we model the baryonic component in our simulations as a static potential. This approach ignores the back-reaction of the halo evolution on the baryons, an effect expected to be sub-dominant, since we are interested in the systems that the final baryonic distribution is known. We consider two models for the baryonic potential. One is the Miyamoto-Nagai (MN) disk (Miyamoto and Nagai, 1975),

$$\Phi_{\rm MN}(R,z) \;=\; \frac{-G\;M_{\rm d}}{\sqrt{R^2 \;+\left(R_{\rm d}+\sqrt{z_{\rm d}^2+z^2}\right)^2}}, \tag{3.1}$$

where $M_{\rm d}$ is the disk mass, $R_{\rm d}$ the disk scale length and $z_{\rm d}$ the disk scale height. The implementation of the MN disk in AREPO is as described in Creasey et al. (2017). We also consider a Hernquist bulge potential (Hernquist, 1990)

$$\Phi_{\rm Hernquist} = -\frac{GM_{\rm H}}{r+r_{\rm H}}\,, \tag{3.2}$$

where $M_{\rm H}$ is the bulge mass and $r_{\rm H}$ is the scale length.

We run three sets of simulations, varying the baryonic component and the strength of the cross section. In the first two sets, we only include the MN disk ($M_{\rm d} = 6.4 \times 10^{10}\ M_\odot$) with two disk scale lengths, $R_{\rm d} = 3$ kpc (compact disk) and $R_{\rm d} = 6$ kpc (extended disk). In both cases, we fix $z_{\rm d} = 0.3R_{\rm d}$. The DM self-scattering cross section is chosen to be $\sigma_{\rm x}/m_{\rm x} = 0$, 0.5, 1, 3, and 5 cm^2/g, i.e., 10 simulations in total. For the *initial* halo component, we assume a spherical NFW profile Navarro et al. (1997), and take the halo parameters as $r_{\rm s} = 37.03$ kpc and $\rho_{\rm s} = 2.95 \times 10^6 M_\odot/{\rm kpc}^3$. The mass ratio of the disk to the halo is motivated by the baryonic Tully-Fisher relation (Lelli et al., 2016). We use the publicly available code SPHERIC, introduced in Garrison-Kimmel et al. (2013), to generate the initial conditions. It truncates the outer halo profile exponentially at $r_{\rm cut}$ to avoid mass divergence. We take $r_{\rm cut} \approx 250$ kpc, close to the virial radius of our initial CDM halo. We fix the gravitational softening length to be $\epsilon = 125$ pc and the mass resolution $m_{\rm p} = 1.32 \times 10^6 M_\odot$. We include 2 million mass particles in our simulations, necessary for resolving the innermost regions, resulting in a halo mass of $2.64 \times 10^{12} M_\odot$.

For the third set, we include both an MN disk and a Hernquist bulge to model the baryon distribution in the MW. The disk parameters are $M_{\rm d} = 6.98 \times 10^{10}\ M_\odot$, $R_{\rm d} = 3.38$ kpc and $z_{\rm d} = 0.2R_{\rm d}$ for the disk. The bulge ones are $M_{\rm H} = 1.05 \times 10^{10}\ M_\odot$ and $r_{\rm H} = 0.46$ kpc. The *initial* halo parameters are $r_{\rm s} = 42.18$ kpc and $\rho_{\rm s} = 1.39 \times 10^6 M_\odot/{\rm kpc}^3$. We have chosen these parameters to reproduce the MW mass model presented in McMillan (2011) (hereafter McM11), see Sec. 3.4 for details. The baryon-model parameters used in our simulations are summarized in Table 3.1. We choose $r_{\rm cut} = 100$ kpc, $\epsilon = 125$ pc and $m_{\rm p} = 5.76 \times 10^5 M_\odot$. We simulate 2 million mass particles and the total halo mass is $1.15 \times 10^{12} M_\odot$.

Additionally, we have run cosmological zoom-in SIDM simulations for 5 MW-mass Aquarius halos (Springel et al., 2008) with the initial conditions taken from (Vogelsberger et al., 2012; Zavala et al., 2013). We will present these simulation results in Sec. 3.4 for comparison.

3.2.2 Halo shape algorithm

We use the method introduced in Dubinski and Carlberg (1991) (see also Allgood et al., 2006) to calculate the ellipticity of the simulated halos. It constructs the axial ratio for the best-fitting

Component	Mass ($10^{10}\ M_\odot$)	Length scale (kpc)
Extended Disk	6.4	6.0
Compact Disk	6.4	3.0
MW-like Disk	6.98	3.38
MW-like Bulge	1.05	0.46

Table 3.1: Parameters of static potentials used in the three sets of simulations.

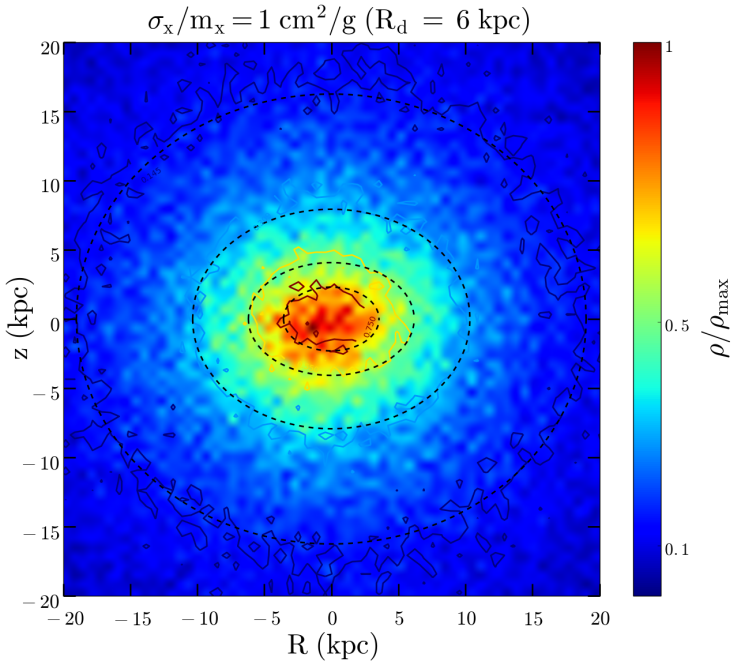

Figure 3.1: Comparison between ellipsoids (dashed) and isodensity contours (solid) for the simulation with $\sigma_x/m_x = 1\ cm^2/g$ and $R_d = 6$ kpc. The horizontal axis is the major axis, while the vertical one is the minor axis aligned with the symmetry axis of the baryonic disk. The color bar shows the density scale to ρ_{max}, the maximal central DM density.

ellipsoid as a function of the major axis length. This method is an iterative one where at each iteration the reduced inertia tensor is determined for the set of particles within the previous ellipsoid, and then a new ellipsoid is determined from this tensor. Specifically, if we denote the major axis length a, then at each iteration the reduced inertia tensor is given by

$$I_{ij} = \sum_{k:d_k<a} \frac{r_{k,i} \times r_{k,j}}{d_k^2} \tag{3.3}$$

where $r_{\rm k,i}$ denotes the coordinate i of particle k, and $d_{\rm k}$ is the elliptical radius found from the previous inertia tensor. We have $d_{\rm k} = \sqrt{x_k^2 + (y_k/q)^2 + (z_k/s)^2}$, where x, y and z are the coordinates along the major-, intermediate- and minor-axes of the ellipsoid, and $q = b/a$, $s = c/a$ are the axial ratios of the intermediate- and minor-to-major axes, respectively. After diagonalizing the inertia tensor with eigenvalues (ascending) $\{\lambda_1, \lambda_2, \lambda_3\}$, we have $q = \sqrt{\lambda_2/\lambda_3}$ and $s = \sqrt{\lambda_1/\lambda_3}$. In the initial iteration, the ellipsoid is set to a sphere, i.e. $q = s = 1$. This process is continued until some convergence criteria, which we take it to be 10^{-6} on the difference between successive iterations is satisfied. We note that if the number of DM particles in an ellipsoid is too small, typically less than 1000, the result from this method is not accurate.Fig. 3.1 shows a comparison between isodensity contours and ellipsoids for an example, where $R_{\rm d} = 6$ kpc and $\sigma_{\rm x}/m_{\rm x} = 1$ cm^2/g. We see the overall agreement between the two methods is excellent.

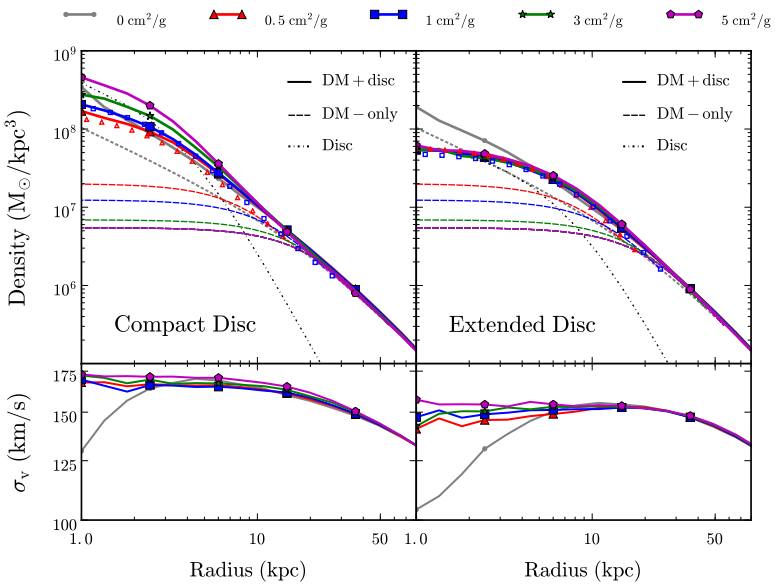

Figure 3.2: Simulated DM density (top, solid) and velocity dispersion (bottom) profiles for $\sigma_{\rm x}/m_{\rm x} = 0$ (gray), 0.5 (red triangles), 1 (blue squares), 3 (green stars), and 5 cm^2/g (magenta pentagons), in the presence of compact (left) and extended (right) discs. On the top panels, we also plot the corresponding NFW initial condition (short dashed) and the SIDM density profiles derived from the analytical method without including the stellar potential (long dashed, the same color scheme as the solid ones), together with the disc mass profile (dash dotted). For comparison, we also show the SIDM density profiles derived from the analytical method with a thin-disc model for $\sigma_{\rm x}/m_{\rm x} = 0.5$ and 1 cm^2/g (open triangles and squares).

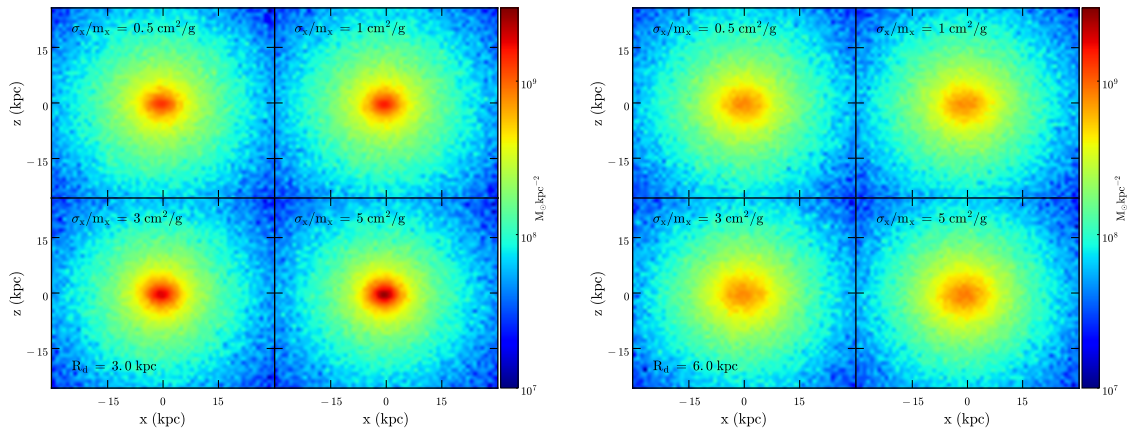

Figure 3.3: Projected SIDM distributions in edge-on views for compact (left) and extended (right) disks with different SIDM cross sections as given in the legend.

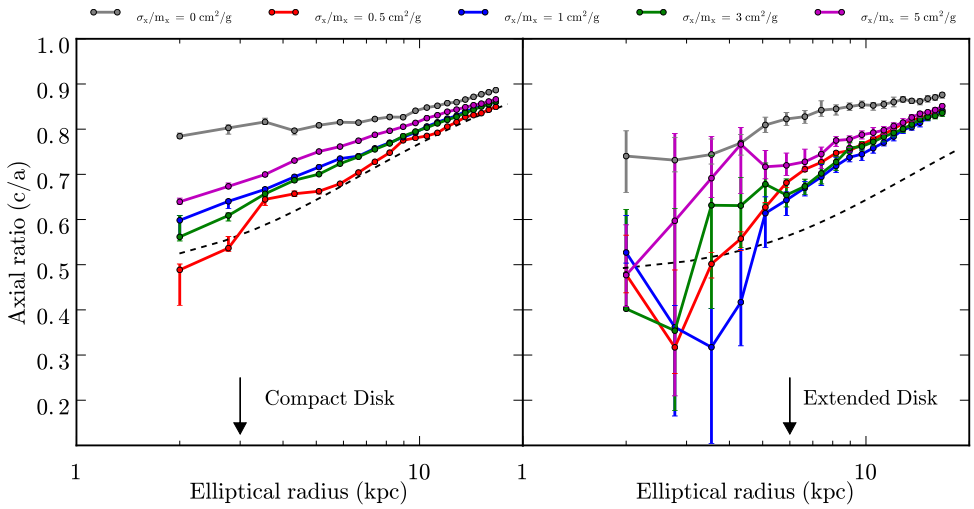

Figure 3.4: Ratio of minor-to-major axes, c/a, vs. the elliptical radius for the compact (left) and extended (right) disks with different cross sections (solid). We also plot c/a for the isothermal profile when the disk dominates the gravitational potential (dashed), $\rho_{\rm DM} \propto \exp[-\Phi_{\rm MN}(R,z)/\sigma_{\rm v}^2]$, where we take the central DM velocity dispersion for $\sigma_{\rm x}/m_{\rm x} = 0.5$ cm^2/g, i.e., $\sigma_{\rm v} = 168$ (compact) and 150 km/s (extended), as shown in Fig. 3.2 (bottom). The arrow denotes the scale radius of the stellar disk. We calculate the numerical errors using the bootstrapping method.

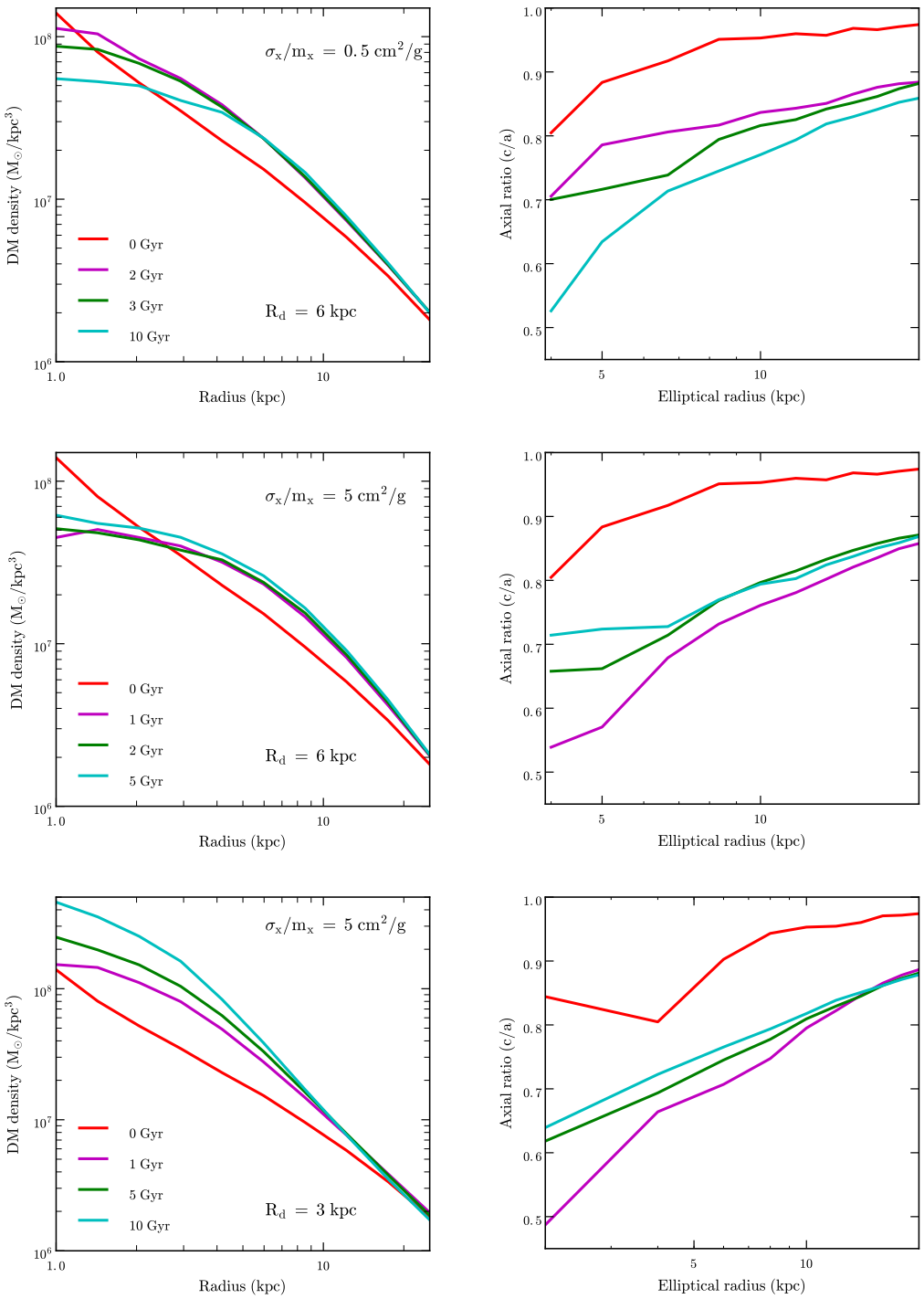

Figure 3.5: Time evolution of the DM density (left) and the halo shape (right) profiles for three representative examples, including simulations with the extended disc for $\sigma_x/m_x = 0.5$ cm^2/g (top) and 5 cm^2/g (middle), and the compact one for $\sigma_x/m_x = 5$ cm^2/g (bottom). Different colors and marker styles denote different evolution epochs, and both left and right panels have the same color and marker scheme.

3.3 SIDM halo properties with a stellar disk

3.3.1 Density profiles

Fig. 3.2 shows the DM density (top) and velocity dispersion (bottom) profiles for $R_{\rm d} = 3$ kpc (left) and 6 kpc (right). The solid curves are from our simulations for different values of $\sigma_{\rm x}/m_{\rm x}$ in the presence of the stellar disk. For comparison, we also plot the SIDM density profiles (dashed) without the disk potential, calculated with the analytical method in Kaplinghat et al. (2014, 2016).

In both cases, the presence of a baryonic potential increases the SIDM density profile and reduces the core size, and the effect is more significant if the baryonic concentration is higher. For $R_{\rm d} = 3$ kpc, a larger cross section leads to a higher DM density (0.5–5 cm^2/g), opposite to the case without baryons. For the extended disk with $R_{\rm d} = 6$ kpc, the SIDM density profiles are almost identical, even though the $\sigma_{\rm x}/m_{\rm x}$ value changes by a factor of 10. A deep baryonic potential also increases the DM velocity dispersion in the inner halo, as shown in the bottom panels. In the case of compact disk, it is evident that the SIDM halos are close to the threshold of mild core collapse, as the velocity dispersion profiles start to develop a negative gradient. The significance is continuously enhanced when $\sigma_{\rm x}/m_{\rm x}$ changes from 0.5 to 5 cm^2/g. We have checked simulation results using the analytical method, where we assume a thin disk model and use the numerical templates developed in Kamada et al. (2017). They agree within 5–20% in the central DM density and velocity dispersion.

The SIDM halo has a distinct evolution history. It first undergoes a core expansion phase, during which the DM collisions transport heat towards the inner region and a central density core forms. Since a self-gravitating system has a negative heat capacity, the core will eventually contract and collapse to a singular state (Balberg et al., 2002). In cosmological SIDM-only simulations, mild core collapse is observed within 10 Gyr when $\sigma_{\rm x}/m_{\rm x} \gtrsim 10$ cm^2/g (Vogelsberger et al., 2012; Elbert et al., 2015). There is also a hint that mild core collapse could occur in hydrodynamical SIDM simulations with $\sigma_{\rm x}/m_{\rm x} = 10$ cm^2/g (Di Cintio et al., 2017)[1]. We have

[1] The simulation results in Di Cintio et al. (2017) are consistent with the predictions from the analytical method in Kaplinghat et al. (2014) when the baryon distribution is properly taken into account.

also checked that for isolated SIDM-only ones with an NFW profile as the initial condition, the core contraction does not occur within 10 Gyr for $\sigma_{\rm x}/m_{\rm x} = 0.5$–$5$ cm^2/g, consistent with the results in Koda and Shapiro (2011). However, the SIDM thermalization with a deep baryonic potential can speed up this process, as shown in our simulations (see also Elbert et al., 2018).

We see that the presence of the stellar potential breaks the monotonic relation between the value of $\sigma_{\rm x}/m_{\rm x}$ and the central SIDM density. The effect depends on the baryon concentration and the size of the self-scattering cross section. Our results indicate that it could be challenging to extract the $\sigma_{\rm x}/m_{\rm x}$ information from stellar kinematics of galaxies dominated by baryons.

3.3.2 Halo shapes

In Fig. 3.3, we show the SIDM halo surface densities for $R_{\rm d} = 3$ kpc (left) and $R_{\rm d} = 6$ kpc (right). The density contrast for the compact case is higher for different cross sections, compared to the extended one, as expected from the density profiles shown in Fig. 3.2. It is also evident that the simulated halos are not spherically symmetric, although their initial conditions are exactly spherical.

Fig. 3.4 shows the ratio of minor-to-major axes vs. elliptical radius $\sqrt{R^2 + (z/s)^2}$ for $R_{\rm d} =$ 3 kpc and $R_{\rm d} = 6$ kpc with different cross sections (solid). In all cases, the c/a value deviates from 1 and decreases towards the center (b/a remains close to 1). However, the SIDM halos are more responsive to the presence of the baryonic disk than their collisionless counterpart, and their shapes are more aligned with the axisymmetric disk potential (dashed). Interestingly, for the compact case, c/a increases when the cross section increases from 0.5 to 5 cm^2/g and the inner halo becomes *rounder* mildly. We can see a similar trend in the case of $R_{\rm d} = 6$ kpc, although the errors in measuring c/a, calculated using bootstrap method, for $r \lesssim R_{\rm d}$ are large due to the lack of enough DM particles in the central region of the halos.

The behavior in Fig. 3.4 can be understood as follows. Since the DM self-interactions thermalize the inner halo, the DM density can modeled by the isothermal distribution (Kaplinghat et al., 2014), $\rho_{\rm DM} \propto \exp\left[-(\Phi_{\rm DM} + \Phi_{\rm MN})/\sigma_{\rm v}^2\right]$, where $\Phi_{\rm DM}$ and $\Phi_{\rm MN}$ are the DM and disk potentials, respectively. $\Phi_{\rm MN}$ induces the deviation from spherical symmetry of the initial NFW

halo, as indicated in Fig. 3.4 (dashed), and the significance depends on its magnitude relative to $\Phi_{\rm DM}$ and $\sigma_{\rm v}^2$. In the compact-disk case, the central DM density increases when $\sigma_{\rm x}/m_{\rm x}$ increases from 0.5 to 5 cm^2/g, as well as the DM dispersion (very mildly), as shown in Fig. 3.2 (left). Accordingly, the baryonic potential becomes less dominant and the inner halo becomes more spherical. Note in the compact-disk case the simulated c/a profile for $\sigma_{\rm x}/m_{\rm x} = 0.5$ cm^2/g agrees well with the isothermal profile due to the baryonic potential, because of the strong dominance of the disk in the inner regions. In addition, for $\sigma_{\rm x}/m_{\rm x} = 5$ cm^2/g (compact), both the inner DM density and velocity dispersion are higher, compared to the CDM case, but the SIDM halo is more aspherical and aligned with the disk than the CDM one. In the extended-disk case, the halo c/a profiles also follow the disk one, but not as close as the compact case, since the disk does not dominate the potential at all radii, as shown in Fig. 3.2 (right).

3.3.3 Evolution history

In this section, we take a closer look at the evolution of the SIDM halo and explicitly show that the presence of the baryonic potential does speed up core contraction and shorten the expansion phase.

Fig. 3.5 shows the density and c/a profiles at different epochs for three examples: the lowest (top) and highest (middle) cross sections in the simulations with the extended disk, and the highest cross section for the compact disk case (bottom). For $R_{\rm d} = 6$ kpc and $\sigma_{\rm x}/m_{\rm x} = 0.5$ cm^2/g, the simulated halo is on the core expansion phase over the 10 Gyr span of the simulation. In this case both central DM density and the c/a ratio decrease continuously. When we increase the cross section to 5 cm^2/g (middle), the duration of the core expansion phase becomes much shorter. After about 1 Gyr, the halo enters the core contraction phase and the central DM density increases, as well as the ratio of minor-to-major axes. A more compact stellar disk can change the halo evolution even more dramatically, as shown in the bottom panel. The simulated halo almost never gets into the expansion phase and the central density and c/a in the regions increases over time monotonically. In this case, the inner SIDM halo contains even more DM mass than its CDM counterpart.

We conclude that the evolution history of the SIDM halo is sensitive to the presence of the baryonic potential. The final halo properties, such as the density profile and the ellipticity, depend on the baryonic concentration and the strength of DM self-interactions.

3.4 Implications for the shape of the Milky Way Halo

The effect of baryons on the SIDM halo can potentially be tested with observations of the MW. Here, we construct a model for the MW potential consisting of an SIDM halo, a baryonic bulge and disk. The DM halo is chosen initially as a spherical NFW profile with $r_s = 42.18$ kpc and $\rho_s = 1.39 \times 10^6 M_\odot/\mathrm{kpc}^3$. We model the disk following an MN potential as in Eq. 3.1, with disk length scale and mass specified in Table 3.1 and bulge following a spherical Hernquist profile. We take the cross section as $\sigma_x/m_x = 1\ \mathrm{cm}^2/\mathrm{g}$.

Top panel of Fig. 3.6 shows the DM density profiles for our SIDM halo (blue), the initial NFW model (gray), and the halo model in McM11 (black). Our MW model reproduces well the estimates for the local DM density near the solar neighborhood from Bovy and Tremaine (2012) (red). Note the initial halo concentration is about 1.5 σ lower than the average for the MW mass object according to Dutton and Macciò (2014) and also lower than that in McM11. This is a necessary choice to be consistent with observations, since SIDM thermalization significantly increases the DM density in the inner regions due to the presence of the baryonic potential. Although the inner density profile of the SIDM halo deviates from the McM11 one, our MW mass model produces a circular velocity profile, consistent with the one in McM11 within 10 % uncertainties, as shown in Fig. 3.6 (bottom).

Fig. 3.7 shows the ratio of minor-to-major axes as a function of the elliptical radius, predicted in our SIDM MW halo model with $\sigma_x/m_x = 1\ \mathrm{cm}^2/g$ (blue solid). Since we assume a spherical NFW initial halo, the deviation from $c/a = 1$ is caused by the disk potential. We see the disk induces a mild asphericity in the inner regions of the halo, $c/a \sim 0.7$–0.8, in good agreement with the result based on the analytical model in Kaplinghat et al. (2014), where the spherical boundary condition is imposed at 10 kpc. Our simulations also show the effect is quite extended,

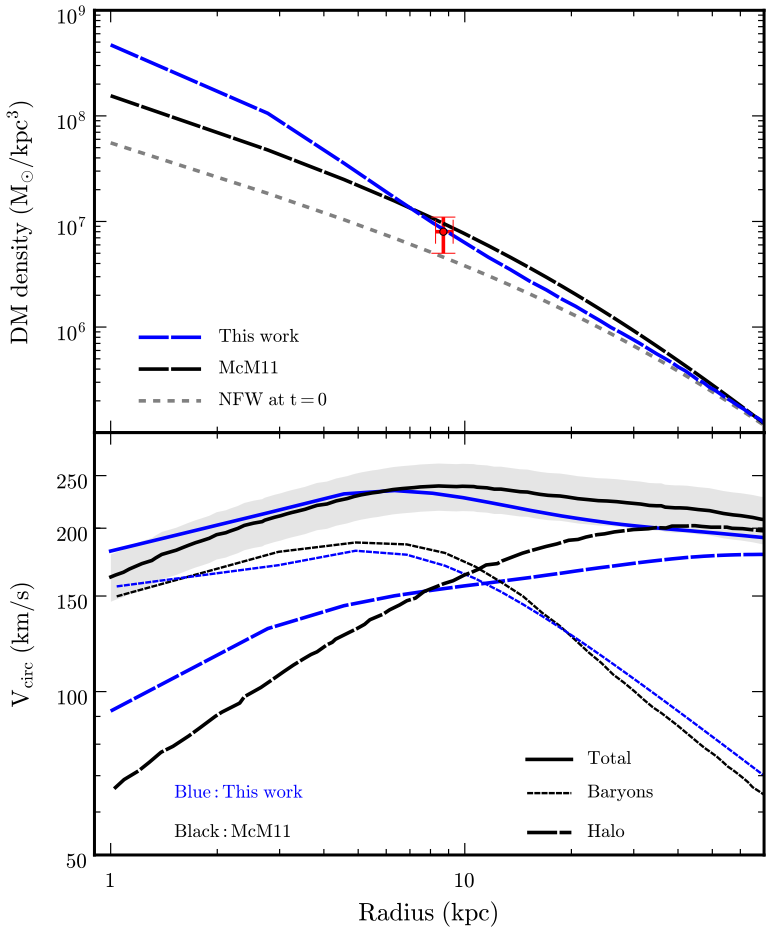

Figure 3.6: Top: DM density profiles of simulated SIDM halo with baryons (blue dashed), best-fitting halo model in McM11 (black dashed), and the NFW initial condition (gray dashed). The data point with error bars indicates the local DM density near the solar position from Bovy and Tremaine (2012). Bottom: Total circular velocity profiles of our MW mass model (blue solid) and best-fitting model in McM11 (black solid) with 10% uncertainties (shaded band). Plotted also DM halo (dashed) and baryon (thin dashed) contributions.

with c/a converging back to unity only at the distance $\sim$ 50 kpc. We also present cosmological SIDM-only simulations of 5 Aquarius halos with $\sigma_x/m_x = 1$ cm^2/g. Our results are in agreement with the previous ones (Peter et al., 2013; Brinckmann et al., 2018). For the roundest halos (Aq-A and Aq-C), $c/a \gtrsim 0.85$ for $r \lesssim 30$ kpc, lending support to our assumption of an initially spherical

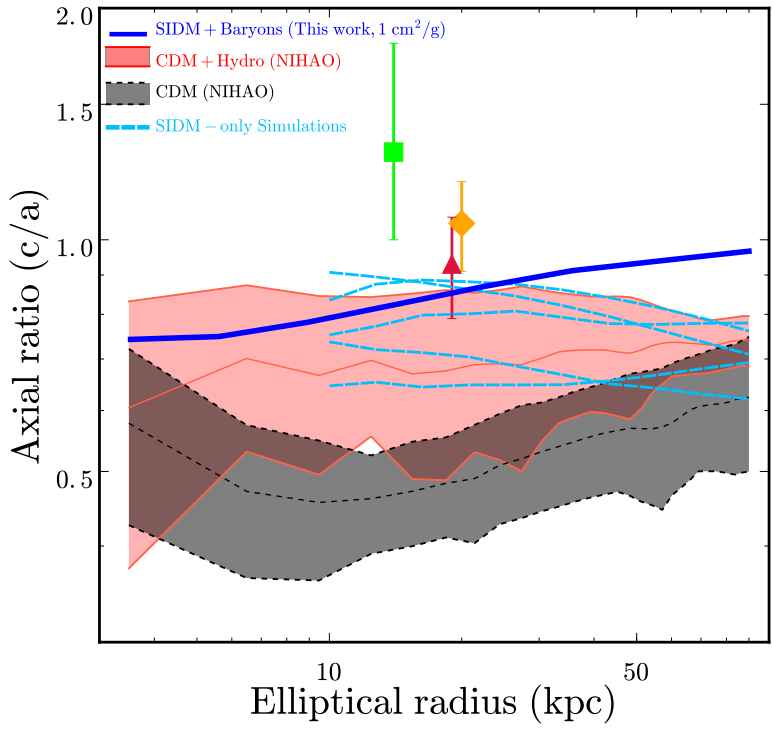

Figure 3.7: Halo shape measurement in different numerical simulations: our MW SIDM halo model (blue solid), cosmological CDM-only (black dashed) and hydrodynamical simulations (orange solid) from the NIHAO project (Butsky et al., 2016) (the shaded area represents the 1σ scatter for the halos with mass $\sim 10^{12}\ M_\odot$), and zoom-in cosmological SIDM-only simulations of 5 Aquarius halos (long dashed). Data points with error bars are the measurements of the MW halo shape using the stellar streams, GD-1 ($c/a = 1.3^{+0.5}_{-0.3}$ at $r \approx 14$ kpc, square), Pal 5 ($c/a = 0.93 \pm 0.16$ at $r \approx 19$ kpc, pentagon), and the combined analysis of the two ($c/a = 1.05 \pm 0.14$ for $r \lesssim 20$ kpc, diamond), taken from Bovy et al. (2016).

NFW halo. Since the DM self-scattering rate increases by a factor of 100 from 30 kpc to inner few kpc, as indicated by the DM density profile shown in Fig. 3.6 (top), we expect the spherical assumption is well-justified in the inner halo.

The MW halo shape has been inferred from observations of stellar streams such as GD-1 and Pal 5 (e.g., Koposov et al., 2010; Bowden et al., 2015; Pearson et al., 2015; Küpper et al., 2015; Bovy et al., 2016). In Fig. 3.7, we show the results presented in Bovy et al. (2016) for GD-1, Pal 5 and the combined one, where an axisymmetric NFW density profile with $b/a = 1$ was used to model the DM distribution in the MW. We see that the phase-space tracks of the

streams are consistent with a spherical DM halo in the MW at intermediate radii, $r \sim 20$ kpc, which indicates any asphericity either intrinsic to the DM distribution or induced by the disk should be at most weak on that scale in order to accommodate the measurements. Our model predicts $c/a \sim 0.85$ at $r \approx 20$ kpc, consistent with the combined constraint on c/a within $\sim 1.5\sigma$. Note that our scale height in the MN disk is $z_{\rm d} \approx 0.68$ kpc, higher than the best-fit value ~ 0.3 kpc in Bovy et al. (2016). We have estimated that taking their $z_{\rm d}$ value would reduce c/a by 5% at most in the inner regions and the difference becomes negligible around 10 kpc. In addition, in our MW model, the total halo mass within 20 kpc is $1.28 \times 10^{11} M_\odot$, consistent with $M_{\rm halo}(r < 20 \text{ kpc}) = 1.1 \pm 0.1 \times 10^{11} M_\odot$ measured in Bovy et al. (2016), although our initial NFW halo has lower concentration, compared to theirs ($r_s = 18.0 \pm 7.5$ kpc). It would be interesting to analyze the stream data with the SIDM halo model.

For comparison, we also plot cosmological CDM-only (gray) and hydrodynamical (red) simulations from the NIHAO project (Butsky et al., 2016). As is well-known, CDM halos from cosmological simulations are strongly triaxial (Frenk et al., 1988; Jing and Suto, 2002; Hayashi et al., 2007; Kuhlen et al., 2007; Vera-Ciro et al., 2011; Diemand and Moore, 2011). Taken at face value, CDM predictions (gray) could look at odds with the observations. However, baryons can make the CDM halo shapes more spherical (red) (see also, Dubinski, 1994; Debattista et al., 2008; Kazantzidis et al., 2010; Abadi et al., 2010; Tissera et al., 2010), an effect partially attributed to the change of orbits from boxy to tube or rounder loop as a result of the central concentration of baryons (Debattista et al., 2008). In the NIHAO simulations, the mean value of c/a is 0.7 for the CDM halos after including baryons, and it can reaches 0.8 at the 1σ level of the scatter, consistent with the observations reasonably well.

Although the sphericity created by the baryons helps CDM to accommodate more easily the observational constraints, the trend with radius could be different in the two models. It seems that CDM halos plus baryons become more spherical at all radii, whereas the effects explored here in SIDM plus baryons would anticipate a flattening of the shapes towards the inner regions that follows that of the disk. Such premise, of course, ignores any effect of feedback or cosmological assembly, which may cause deviations of the system from equilibrium. Therefore, the

exciting premise of using halo shape profiles to differentiate DM candidates awaits confirmation from cosmological hydrodynamical SIDM simulations. We hope such experiments will become available in the near future.

3.5 Summary

We use isolated N-body simulations of DM halos with static disk potentials to explore the gravitational effect of baryons on SIDM halos. We model the disk as a Miyamoto-Nagai potential embedded within an initially NFW halo with mass $\sim 10^{12}\ M_{\odot}$. We consider different self-scattering cross sections, $\sigma_{\rm x}/m_{\rm x} = 0.5,\ 1,\ 3$, and 5 cm^2/g besides the special case, $\sigma_{\rm x}/m_{\rm x} = 0$ cm^2/g. In addition, we vary the radial length scale of the disk, $R_{\rm d}$, to study in detail how the DM halo responds to the baryons as a function of how relevant their contribution is to the total potential at a given radius.

In the absence of baryons, SIDM halos develop a central flat core with its density and size that depend mostly on the self-scattering cross section. We confirm that the inclusion of a disk potential can change this behavior due to SIDM thermalization with the potential, resulting in a higher core density and a smaller core than expected without the disk, a crucial effect in solving the diversity problem in SIDM (Kamada et al., 2017; Creasey et al., 2017),

We highlight two phases of evolution during our numerical experiments: a first stage of *core expansion*, during which the density core gets established due to the turn-on of the self-interactions, and a second stage of *core contraction* due to the gravitational effects of the baryons. The timescale for these two phases of evolution is a function of both, the cross section and the relative importance of the baryons inside the core. Higher cross sections and more compact baryonic disks (encoded in a smaller length scale) speed up the transition between the two phases and make the timescale of core expansion shorter.

We have also studied the role of the disk potential in shaping the SIDM halo. To explore this subtle effect, we assumed an exact spherical initial NFW profile such that any departure from sphericity is due to the influence of the baryonic potential. Compared to the case of

$\sigma_x/m_x = 0$ cm^2/g, the SIDM halos are more responsive to the potential due to the thermalization, and their final flattening is more aligned with the orientation of the disk, consistent with the expectation from the analytical method. Our simulations clearly demonstrate that the induced asphericity is mainly sensitive to the contribution of the disk to the total potential, relative to the DM one. We further confirmed this by checking the evolution history of the SIDM halos. The flattening effect is maximized during the epoch when the core has the lowest density, which coincides with the time when the disk contribution to the total potential is also maximized.

We have constructed a mass model for the MW and explored the shape prediction with observations. The model consists of a stellar disk and a bulge, embedded within a spherical SIDM halo. It reproduces observed stellar kinematics of the Galaxy within the uncertainties and the local DM density reported in the solar neighborhood. We find that the baryons are able to induce a mild flattening ($c/a \sim 0.7$–0.8) in the inner regions but the effect weakens at larger radii. At $r \sim 20$ kpc where observational constraints seem to suggest an almost spherical halo, the effects of the disk are not strong, in agreement with the observations. We propose that the quasi sphericity of the halo at large distance is easier to accommodate in SIDM models than within the strongly triaxial structures predicted by CDM, although considering the effects of baryons might help to reconcile CDM models with observed spherical halos. Furthermore, we argue that a study of halo shapes as a function of radius might be able to help distinguish the nature of DM, although a more stringent comparison to cosmological simulations are needed to confirm this last point. On the observational side, future surveys capable of inferring the shape of the Galactic halo within the inner 20 kpc regions are promising avenues to make progress on establishing the non-canonical nature of DM.

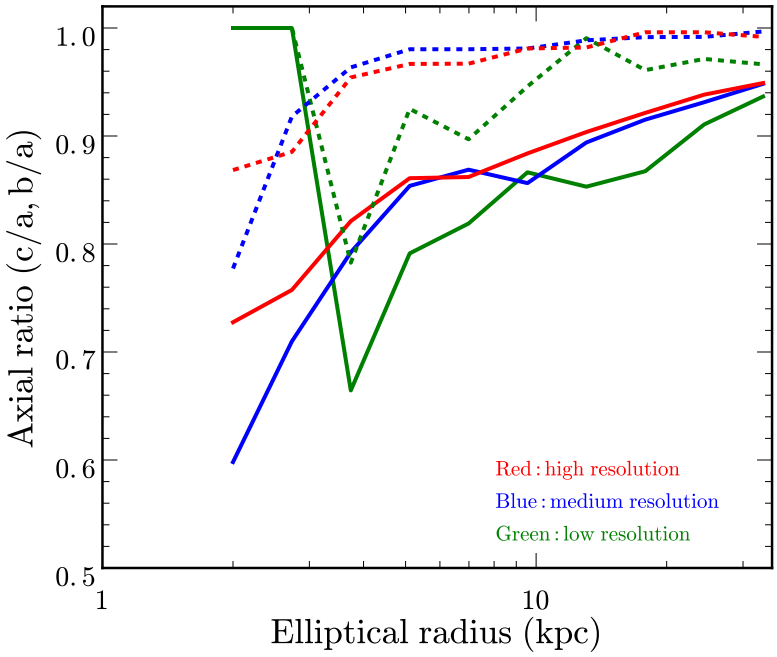

Figure 3.8: Ratio of minor- (solid) and intermediate-to-major (dashed) axes for the convergence test runs.

3.6 Appendix

3.6.1 Convergence test for halo shape analysis

To evaluate accuracy of the shape measurement, we follow Vera-Ciro et al. (2011) to determine the convergence radius where shape measurements are robust in our simulations. We consider the convergence radius $r_{\rm conv}$ (Power et al., 2003; Navarro et al., 2010),

$$\kappa(r_{\rm conv}) \equiv \frac{t_{\rm relax}}{t_{\rm cir}(r_{200})} = \frac{\sqrt{200}}{8}\frac{N(r_{\rm conv})}{\ln N(r_{\rm conv})}\left(\frac{\overline{\rho}(r_{\rm conv})}{\rho_{\rm crit}}\right)^{-1/2}$$

where $t_{\rm relax}$ is the two-body relaxation time scale due to gravitational encounters, $t_{\rm cir}$ is the circular orbit timescale at r_{200}, N is number of DM particles and $\overline{\rho}$ is the average density inside the convergence radius. We take $\kappa(r_{\rm conv}) = 7$ as in Vera-Ciro et al. (2011). In addition, we require $\sim$ 70% of the particles to be inside the virial sphere and at least 2000 DM particles

Resolution Level	m_p ($M_\odot$)	N_{tot}	ϵ (pc)	r_{conv} (kpc)	N_{conv}
Low	2.18×10^8	1.6×10^5	500	6.08	1190
Intermediate	3.97×10^6	8.8×10^5	250	2.99	1813
High	1.31×10^6	2×10^6	125	2.18	2192

Table 3.2: Summary of simulations for convergence test. m_p is mass of each particle in each simulation, N_{tot} is total number of particles, ϵ is gravitational softening length, r_{conv} is convergence radius, and N_{conv} is number of particles inside r_{conv}.

inside of convergence radius.

The first requirement is satisfied if we choose a large cutoff radius in the SPHERIC code, at which the density profile transits from an NFW one to an exponentially decaying one to avoid the divergence of the mass. Then we run three simulations with different values of the DM particle number and the gravitational softening length as a convergence test with details summarized in Table 3.2. The convergence radius decreases with increasing the number of total DM particles. Thus, to probe the shape of the inner halo, down to few kpc, we need at least 2 million particles in simulations. Fig. 3.8 shows the b/a (top) and c/a (bottom) profiles for different resolutions, we take a static MN potential as stellar disk similar to Sec. 3.3, with a MW-sized halo with $M_{200} \simeq 2.6 \times 10^{12}\ M_\odot$. We see that the convergence improves when N_{tot} increases. We take high-resolution run in the results presented in Sec. 3.3 and 3.4.

Chapter 4

Self-interacting dark matter subhalos in the Milky Way's tides

4.1 Introduction

Self-interacting dark matter models provide novel solution to puzzles associated with dwarf spheroidal galaxies (dSphs) in the Milky Way (MW), e.g., the most massive subhalos predicted in CDM are too massive to host the bright MW dSphs (Boylan-Kolchin et al., 2011; Boylan-Kolchin et al., 2012). SIDM simulations show that dark matter self-interactions can lower the central density of the subhalos and alleviate the tension (Vogelsberger et al., 2012; Zavala et al., 2013). Despite this success, a detailed analysis of stellar kinematics of the bright MW dSphs shows the preferred dark matter self-scattering cross section per mass, σ/m, varies within a wide range (Valli and Yu, 2018). The spread in the cross section reflects diverse dark matter contents of MW dSphs' halos, beyond the scatter predicted in CDM-only simulations as in Vogelsberger et al. (2016). For example, Draco and Ursa Minor are much denser than Fornax and Sextans (Valli and Yu, 2018; Read et al., 2019; Read et al., 2018; Kaplinghat et al., 2019). Unlike spiral galaxies in the field, we expect environmental effects to play a relevant role in shaping MW subhalos. Indeed, in the case of CDM, the tidal effects can lower central densities for massive subhalos (Hayashi et al., 2003; Peñarrubia et al., 2008, 2010; Brooks and Zolotov,

2014; Wetzel et al., 2016) and reduce the number of small ones (Sawala et al., 2016; Fattahi et al., 2016; Garrison-Kimmel et al., 2017; Robles et al., 2019).

Cosmological simulations have shown that SIDM subhalos have a larger spread in the inner dark matter content for $\sigma/m = 10\ \mathrm{cm}^2/\mathrm{g}$ Vogelsberger et al. (2012), compared to the CDM case. In particular, with such a large cross section, subhalos could experience SIDM core collapse, resulting in high central densities. More recently, it has been suggested that Draco's host could be in the core-collapse phase for $\sigma/m \gtrsim 5\ \mathrm{cm}^2/\mathrm{g}$ (Nishikawa et al., 2019), as it has a small pericenter distance to the MW estimated from Gaia data (Fritz et al., 2018) and the tidal effect could trigger the core collapse. Intriguingly, for the bright MW dSphs, there is an anti-correlation relation between their central densities and pericenters Kaplinghat et al. (2019), which seems to support this scenario.

In this chapter, we explore tidal evolution of SIDM subhalos in the MW's tides, using N-body simulations implemented with realistic MW potentials. The SIDM thermalization coupled with the MW tidal field can lead to diverse dark matter distributions in subhalos. And they can be in either core-collapse or -expansion phases, depending on the cross section, pericenter and initial halo concentration. We demonstrate that Draco and Fornax, two extremes in the dark matter content among the bright MW dSphs, can be explained in the SIDM model with $\sigma/m = 3\ \mathrm{cm}^2/\mathrm{g}$, the value used to fit the diverse rotation curves of spiral galaxies in the field (Kamada et al., 2017; Creasey et al., 2017; Ren et al., 2018). We further explicitly show the mechanism leading to core collapse in the tidal field and study mass loss for both SIDM and CDM subhalos.

4.2 Simulation setup.

We carry out N-body simulations using the code AREPO (Springel et al., 2001) with a module developed in Vogelsberger et al. (2012) for modeling dark matter self-interactions, and use SUBFIND (Springel et al., 2001) to follow the evolutionary track of the subhalo, defined as the set of gravitationally self-bound particles. Following (Sameie et al., 2018), we model the baryon and dark matter distributions of the MW with static potentials, while treating dwarf subhalos

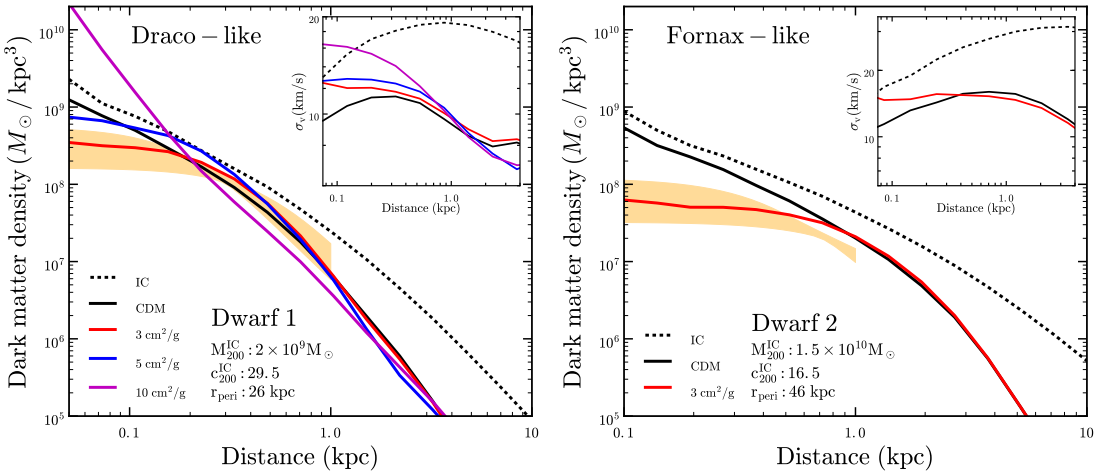

Figure 4.1: Dark matter density and velocity-dispersion (inset) profiles at $t = 10$ Gyr for Dwarf 1 (left) and Dwarf 2 (right). The orange bands show cored isothermal density profiles from the fits to stellar kinematics of Draco (left) and Fornax (right) at 95% CL (Kaplinghat et al., 2019).

with the N-body code.

We include both the disk and bulge components in our MW model since they present in the MW and can play a significant role in tidal evolution of the subhalos (Robles et al., 2019). For the stellar disk, we use the Miyamoto-Nagai potential $\Phi_{\rm MN} = -GM_{\rm d}/\sqrt{R^2 + (R_{\rm d} + \sqrt{z_{\rm d}^2 + z^2})^2}$ (Miyamoto and Nagai, 1975), where $M_{\rm d} = 6.98 \times 10^{10}\ M_\odot$ is the disk mass, $R_{\rm d} = 3.38$ kpc is the disk scale length, and $z_{\rm d} = 0.3$ kpc is the disk scale height. In addition, we include a Hernquist bulge potential $\Phi_{\rm H} = -GM_{\rm H}/(r + r_{\rm H})$ (Hernquist, 1990), where $M_{\rm H} = 1.05 \times 10^{10}\ M_\odot$ is the bulge mass and $r_{\rm H} = 0.46$ kpc. We model the main halo using an NFW profile (Navarro et al., 1996) with the maximal velocity $V_{\rm max} = 200.5$ km/s and the associated radius $r_{\rm max} = 43.4$ kpc, and the corresponding halo mass is $M_{200} = 1.4 \times 10^{12}\ M_\odot$. With these parameters chosen for the main halo and the baryonic component, we can reproduce the MW mass model presented in McMillan (2011), in accord with measurements of MW stellar kinematics and the local dark matter density. In principle, one should also include the self-scattering effect for the main halo. However, for a MW-like galaxy, where the baryons dominate the central regions, an SIDM halo profile can be similar to an NFW one, because SIDM thermalization with the baryonic potential increases the central dark matter density (Kaplinghat et al., 2014; Elbert et al., 2018; Sameie et al., 2018; Robles et al., 2019). We have checked that the NFW halo we take here is a good approximation

to the SIDM MW halo constructed in Sameie et al. (2018). We also note that the host potential does not evolve with time.

We use an NFW profile to model the initial dark matter distribution in subhalos and choose the following three sets of initial conditions. Dwarf 1: its characteristic maximal circular velocity and associated radius are $V_{\rm max} = 28.8$ km/s and $R_{\rm max} = 1.9$ kpc, respectively. And the corresponding halo mass is $M_{200} = 2 \times 10^9 M_\odot$ and concentration $c_{200} = 29.5$, evaluated at redshift 0; Dwarf 2: $V_{\rm max} = 47.6$ km/s and $R_{\rm max} = 6.8$ kpc, or equivalently $M_{200} = 1.5 \times 10^{10}\ M_\odot$ and $c_{200} = 16.5$; Dwarf 3: $V_{\rm max} = 26.7$ km/s and $R_{\rm max} = 2.5$ kpc, or $M_{200} = 2 \times 10^9\ M_\odot$ and $c_{200} = 22.9$. Note Dwarf 3 has the same initial halo mass as Dwarf 1, but its concentration is slightly lower. We use the code SPHERIC (Garrison-Kimmel et al., 2013) to generate initial conditions for the subhalos.

For Dwarf 1 and 3, we simulate CDM and SIDM cases with $\sigma/m = 3$ cm^2/g, 5 cm^2/g and 10 cm^2/g, and fix the pericenter as 26.5 kpc to be consistent with Draco's, 28^{+12}_{-7} kpc, estimated from Gaia DR 2 Fritz et al. (2018). For Dwarf 2, we perform the CDM run as well as SIDM with $\sigma/m = 3$ cm^2/g, and take the pericenter as 46 kpc, motivated by Fornax's 58^{+26}_{-18} kpc (Fritz et al., 2018). We place the initial subhalo at a distance of 230 kpc from the center of the main halo at $t = 0$, and confine the orbit in the plane of the stellar disk. For each subhalo, we choose a "kick" velocity, which is perpendicular to the line connecting the center of the main halo and the subhalo, so that we can obtain the desired pericenter distance; see Appendix for the orbital trajectory of Dwarf 1. We perform simulations with total number of particles $N_{\rm p} = 2 \times 10^6$ for Dwarf 1 and 3, and $N_{\rm p} = 5 \times 10^6$ for Dwarf 2, yielding equivalent-Plummer gravitational softening length of 25 pc.

4.3 A case for Draco and Fornax.

We first highlight that the SIDM model with a fixed cross section could explain both Draco and Fornax, although their central dark matter densities differ significantly.

Fig. 4.1 (left) shows the density and velocity-dispersion profiles (solid) at $t = 10$ Gyr for

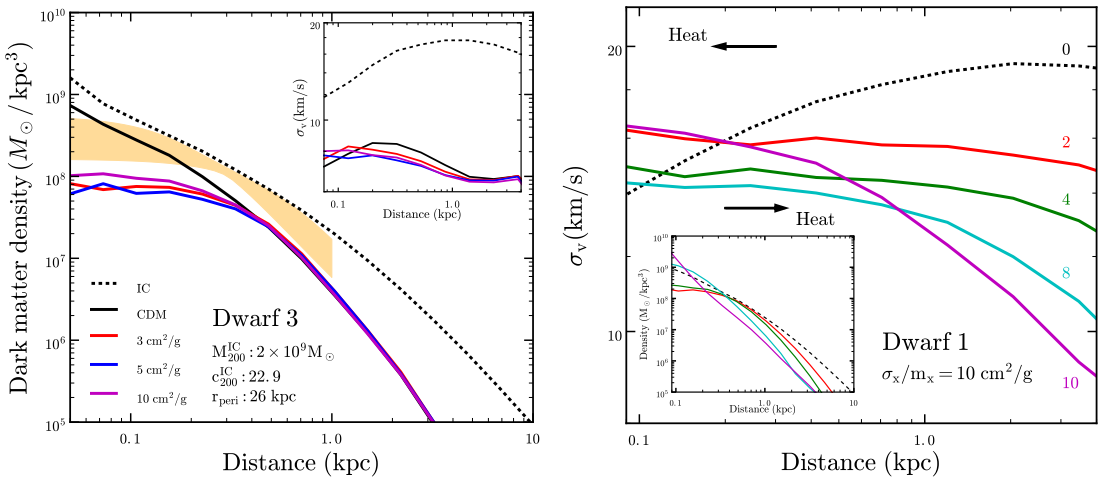

Figure 4.2: Left: Dark matter density and velocity-dispersion (inset) profiles for Dwarf 3. It has the same initial mass as Dwarf 1, but slightly lower concentration. The orange band is the same as the left panel of Fig. 4.1. Right: dark matter velocity-dispersion and density (inset) profiles at different evolution times, $t = 0,\ 2,\ 4,\ 8$ and 10 Gyr for Dwarf 1 with $\sigma/m = 10$ cm^2/g. The symbol "←" ("→") denotes the heat-flow direction in the SIDM core-expansion (-collapse) phase.

Dwarf 1. In all cases, the MW's tides significantly strip away halo masses and lower densities in the outer regions. All of them have similar density profiles for $r \gtrsim 1$ kpc, but their central densities are different. For CDM, the inner profile is resilient to tidal stripping and remains cuspy as the initial one (dashed), consistent with earlier findings (Hayashi et al., 2003; Peñarrubia et al., 2008, 2010). While for SIDM, the central density increases with the cross section, opposite to the trend found in field halos (Elbert et al., 2015; Vogelsberger et al., 2016). In fact, all the SIDM halos are in the core-collapse phase after 10 Gyr's tidal evolution, as their velocity dispersions are larger than the CDM counterpart and profiles have negative gradients in the inner regions, $r \lesssim 1$ kpc, an indication of SIDM core collapse (Balberg et al., 2002; Elbert et al., 2015; Essig et al., 2018; Nishikawa et al., 2019). For a field halo with the same halo parameters as Dwarf 1, we can use equation 4 in Essig et al. (2018) to estimate the core-collapse time to be $t_c \sim 16$ Gyr for $\sigma/m = 10$ cm^2/g and it becomes even longer for a smaller cross section, as $t_c \propto 1/(\sigma/m)$. Thus, the MW tides can significantly accelerate the onset of core collapse for SIDM subhalos.

For SIDM with $\sigma/m = 3$ cm^2/g, the dark matter density profile after tidal evolution agrees with the cored isothermal density profile inferred from the stellar kinematics of Draco (Kapling-

hat et al., 2019). For a field halo with the same initial NFW profile as Dwarf 1, dark matter self-interactions create a large density core and the central density is $8.5 \times 10^7 M_\odot/\mathrm{kpc}^3$ estimated using the analytical model in (Kaplinghat et al., 2016), too low to be consistent with observations of Draco. This explains why the earlier analyses (Valli and Yu, 2018; Read et al., 2018), which did not take into account the tidal effects, found $\sigma/m \lesssim 0.3\ \mathrm{cm}^2/\mathrm{g}$ for Draco. While for two other SIDM simulations with larger cross sections, the predicted central densities are actually too high to explain Draco, opposite to the expectation for the field halo. We have also checked that for Dwarf 1 with $\sigma/m = 3\ \mathrm{cm}^2/\mathrm{g}$, the inner density is reduced by 20% if we allow for pre-evolution for 3 Gyr outside of the main halo and then another 10 Gyr's tidal evolution.

Fig. 4.1 (right) shows the density and velocity-dispersion profiles at $t = 10$ Gyr for Dwarf 2. We take $\sigma/m = 3\ \mathrm{cm}^2/\mathrm{g}$ for the SIDM run, and the halo is still in the core-expansion phase after 10 Gyr's evolution. Dwarf 2 has higher halo initial mass but lower concentration, compared to Dwarf 1. In this case, the interplay between dark matter self-interactions and gravitational tides leads to a large SIDM density core and a shallow density profile, reproducing the cored density profile inferred from Fornax Kaplinghat et al. (2019) reasonably well. We could adjust its halo parameters and pericenter to further improve the agreement in the range of 0.5–1 kpc.

We have demonstrated that the interplay between SIDM thermalization and tidal stripping can lead to diverse central densities for subhalos, in accord with observations. Draco's host has high concentration and experiences core collapse when it evolves in the MW's tidal field, resulting in a high central density. On the other hand, Fornax's host halo concentration is lower, and it is in the core-expansion phase after tidal evolution, leading to a shallow density core. Thus, we expect SIDM can accommodate diverse dark matter contents in MW dSphs, as we have shown for the two extremes, Draco and Fornax, consistent with theoretical predictions (Nishikawa et al., 2019; Kaplinghat et al., 2019). In our simulations, we have deliberately chosen the halo parameters for Dwarf 1 and 2 such that the SIDM model with $\sigma/m = 3\ \mathrm{cm}^2/\mathrm{g}$ (Kamada et al., 2017; Ren et al., 2018; Creasey et al., 2017) can reproduce the observations after the tidal evolution. For other σ/m values, we would need to adjust the initial parameters to match observations.

Dwarf 1's initial halo concentration is on the higher end of the distribution predicted in

cosmological simulations (Pilipenko et al., 2017), but we emphasize this is a necessary condition for the core collapse to occur, as t_c is extremely sensitive to c_{200} (Nishikawa et al., 2019; Essig et al., 2018; Kaplinghat et al., 2019), $t_c \propto (\sigma/m)^{-1} M_{200}^{-1/3} c_{200}^{-7/2}$. A small difference in c_{200} could lead to a huge difference in t_c. To see this, we simulate Dwarf 3 that has the same initial mass as Dwarf 1 but slightly lower concentration. As shown in Fig. 4.2 (left), all SIDM cases have similar shallow density profiles and there is no clear evidence of core collapse, even though c_{200} is only reduced by 20%. In this case, even CDM predicts a density too low to be consistent with observations for $r \gtrsim 0.2$ kpc, indicating that Draco's host could be indeed highly-concentrated. On the other hand, since there is a degeneracy between t_c and σ/m, one may reduce c_{200} mildly by increasing σ/m. In addition, smaller c_{200} could be allowed if the actual pericenter distance is smaller than the one we take in simulations.

4.4 Tidal evolution and core collapse.

To further appreciate dynamics triggering SIDM core collapse in the tidal field, we take a close look at the evolution history of Dwarf 1 with $\sigma/m = 10$ cm^2/g, the most extreme case in our study.

Fig. 4.2 (right) shows the velocity-dispersion profiles at different times during the evolution. Overall, the $\sigma_{\rm v}$ value at large radii, say $r = 1$ kpc, decreases gradually, due to tidal stripping from the MW. Initially, inner $\sigma_{\rm v}$ has a positive gradient in the radius as predicted by the NFW profile. At early stages of the evolution, dark matter self-interactions lead to heat transfer from the outer to inner regions, denoted by the "←" symbol, the core size increases and the central density decreases, similar to the case of a field SIDM halo. At the same time, the maximal value of $\sigma_{\rm v}$, the height of the heat reservoir of the dwarf halo, decreases over time due to the mass loss of the dwarf halo in the MW tidal field. Thus, a negative gradient, a necessary condition for the onset of SIDM core collapse, can be more easily satisfied for a subhalo than a field halo. For the example we consider, the transition occurs around 4 Gyr, at a time when the inner dispersion profile is almost flat. Then, the heat flow reverses its direction towards the outer region ("→").

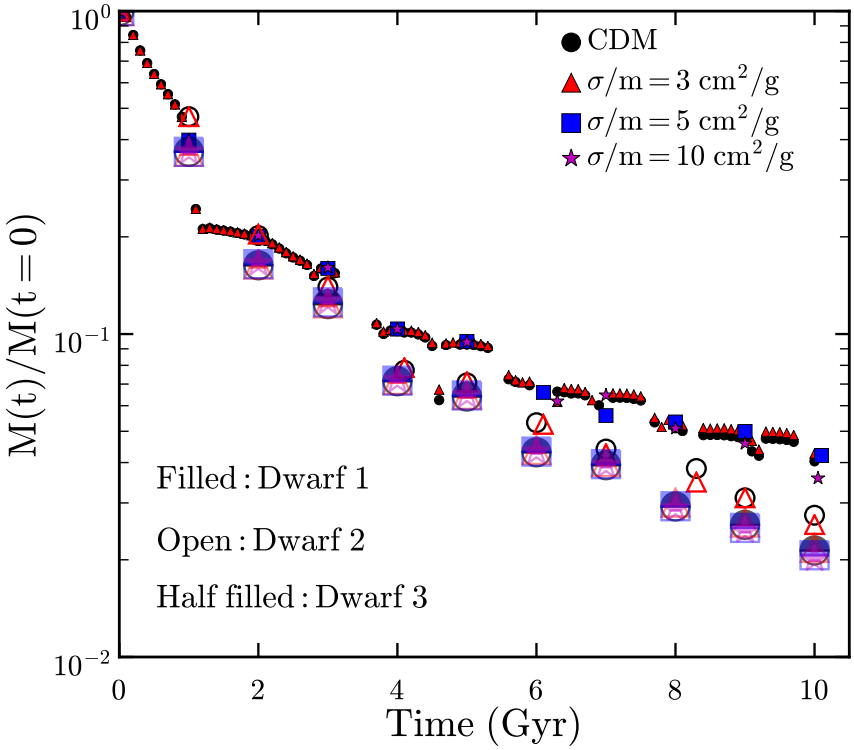

Figure 4.3: Time evolution of the bound mass, normalized to the initial halo mass.

As a self-gravitating system, the inner halo has negative heat capacity, the more heat is extracted by dark matter collisions, the further it collapses to convert its gravitational energy to kinetic energy (Binney and Tremaine, 2008). Thus, both the inner dispersion and density increases at late stages, $t = 8$–10 Gyr. We have also simulated Dwarf 1 with $\sigma/m = 10$ cm^2/g, but a larger pericenter, 46 kpc, and found the core-collapse transition occurs around 8 Gyr.

4.5 Mass loss of Milky Way Subhalos

As we have shown, the interplay between dark matter self-interactions and the MW's tides can lead to diverse inner density profiles. However, overall tidal evolution histories for the cases we consider are remarkably similar. Fig. 4.3 shows the ratio of the total mass of bound particles to the initial halo mass vs. time. For CDM and SIDM ($\sigma/m = 3$ cm^2/g) simulations of Dwarf 1, we present high-frequency time output results, while low-frequency ones for the others. In

all cases, the halo loses 80% of its initial mass within the first 2 Gyr. Moreover, for a given initial halo and its pericenter, the mass loss rate is almost independent of the self-scattering cross section for the cases we study.

We also find that the mass-loss rate is sensitive to the halo concentration. For example, Dwarf 1 has a smaller pericenter than Dwarf 2, but its mass-loss rate at later stages is less pronounced than Dwarf 2. And Dwarf 1 and Dwarf 3 have the same pericenter and initial mass, but the former is a factor of 2 more massive than the later after $t = 10$ Gyr's tidal evolution as Dwarf 1 has a higher initial c_{200} value. These results reflect the fact that a subhalo with high concentration is more resilient to tidal stripping.

4.6 Summary

We have shown that the interaction between the SIDM subhalos and the MW's tides can lead to diverse dark matter density profiles in the inner region. The significance of the tidal effects depends on several factors, including the subhalo concentration, mass, self-scattering cross section, pericenter and infall time. In particular, our simulations show the SIDM core-collapse condition is extremely sensitive to the initial halo concentration. After including the tidal effects, we have demonstrated that the SIDM model with a fixed cross section, proposed for field galaxies, can accommodate the MW dSphs Draco and Fornax as well, although their dark matter contents differ significantly. For the cases we studied, the overall mass loss rates are almost identical for SIDM and CDM subhalos. With our choice of orbits, all simulated dwarf halos lose 96–98% of their original mass after 10 Gyr's tidal evolution.

There are several promising directions we can explore in the future. It is natural to extend our work to other MW dwarfs, including ultra-faint dwarf galaxies, to see if SIDM can fully reproduce the observed trends in these systems (Kaplinghat et al., 2019). Moreover, we can study the stellar distribution of MW dwarf galaxies and its correlation with the core size and the pericenter. It would also be of great interest to perform hydrodynamical simulations to follow the formation and growth of a MW-like galaxy and study the tidal effects on SIDM subhalos in

the cosmological setup.

4.7 Appendix

4.7.1 Orbital trajectory

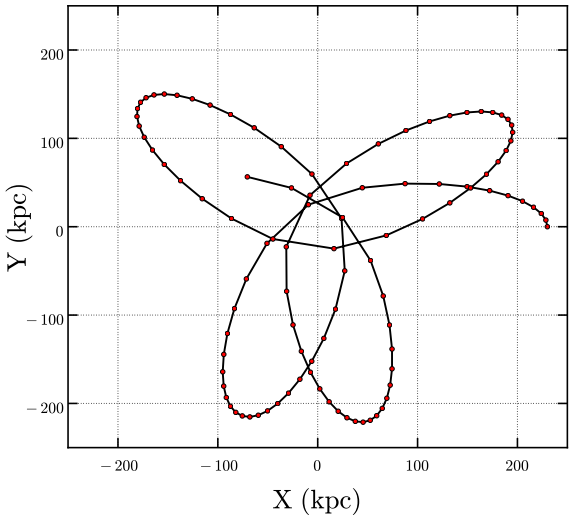

Figure 4.4: Orbital trajectory for Dwarf 1 with $\sigma/m = 3$ cm^2/g.

Fig. 4.4 shows the orbital trajectory for Dwarf 1, which has a pericenter of 26 kpc. In our simulations, we place the initial subhalo at a distance of 230 kpc from the center of the main halo and confine the orbit in the plane of the disk.

Chapter 5

Halo abundance in self-interacting dark matter models

5.1 Introduction

Despite the huge success of CDM on explaining large scale observations, there have been various reports pointing toward both small-scale (Moore, 1994; Flores and Primack, 1994; Klypin et al., 1999; Moore et al., 1999; Boylan-Kolchin et al., 2011; Oman et al., 2015) and large-scale issues (MacCrann et al., 2015; Riess et al., 2016; Addison et al., 2018). While these anomalies on different scales could be due to either systematic observational uncertainties (Kitching et al., 2016; Joudaki et al., 2017; Kim et al., 2017a) or baryonic physics (Pontzen and Governato, 2012; Brooks et al., 2013; Santos-Santos et al., 2018; Garrison-Kimmel et al., 2017), there has been a growing interest in work within the framework of non-CDM models to address these difficulties (e.g. see Abazajian, 2017; Tulin and Yu, 2018; Buen-Abad et al., 2018).

For example, DM with non-zero free streaming velocities suppresses the matter power spectrum and delays halo formation, resulting in a lower number density of virialized structures and less concentrated DM haloes (Lovell et al., 2014; Menci et al., 2018). Moreover, strong DM self-interactions, through kinematic thermalization, tie the DM distributions to the baryonic ones (Kaplinghat et al., 2014; Elbert et al., 2018; Sameie et al., 2018) such that it potentially reduces

the tension in some of the small-scale puzzles (Vogelsberger et al., 2012; Zavala et al., 2013; Rocha et al., 2013; Peter et al., 2013; Kamada et al., 2017; Creasey et al., 2017; Robertson et al., 2018a,b; Vogelsberger et al., 2019; Valli and Yu, 2018; Ren et al., 2018). DM could also be coupled to dark radiation such that this extra relativistic component could potentially explain the tension in the measurements of H_0 from local and CMB observations, and also, through damping the power spectrum via *dark acoustic oscillations* (DAO), reduce the tension in σ_8 measurements and possibly the missing satellites problem (e.g. see Vogelsberger et al., 2016; Chacko et al., 2016; Brust et al., 2017). This rich phenomenology of “interacting" DM models has led several authors to categorize different DM interactions based on their astrophysical predictions (Cyr-Racine et al., 2016; Murgia et al., 2017), and study the astrophysical constraints on their model parameters (Vogelsberger et al., 2016; Lovell et al., 2018; Huo et al., 2018; Pan et al., 2018; Díaz Rivero et al., 2018).

A main feature of these DM models when compared to standard CDM is their predictions for the abundance of DM structures in different mass regimes. Numerical simulations, and semi-analytical modeling based on the extended Press-Schechter approach (Press and Schechter, 1974; Bond et al., 1991; Bower, 1991; Lacey and Cole, 1993) have been utilized to study halo and subhalo mass functions within the context of non-CDM scenarios (Benson et al., 2013; Schneider et al., 2013; Buckley et al., 2014; Schneider, 2015; Schneider et al., 2017). These authors have shown that the cutoff in the linear theory power spectrum suppresses the halo mass function at low masses, and hence it is possible to test these models with observations to constrain the mass function. In practice, the semi-analytical approach needs to be calibrated with numerical simulations to make reliable prediction for mass functions. Moreover, it is well-known that the choice of window function in Press-Schechter formalism has a significant impact on the predictions of the model for the suppression of the mass function in the small mass regime where deviations from CDM are expected (see e.g. Benson et al., 2013; Leo et al., 2018).

In this paper, we use both the semi-analatyical method and N-body simulations to study mass functions for interacting DM models, where DM is coupled to dark radiation via a force mediator. For the sake of convenience, we mainly focus on the power spectra used in the ETHOS

project (Cyr-Racine et al., 2016; Vogelsberger et al., 2016), and perform the calibration analysis by comparing the analytical predictions with the simulations in the halo mass range above 3×10^{10} $M_\odot$ at $z = 0$. We further perform cosmological simulations with improved mass resolution to test the model in the low mass regime, 10^8–10^{10} $M_\odot$, at different redshifts. The analytical model exhibits remarkable universality, i.e., once calibrated with respect to joint data points from CDM and ETHOS1 simulations in the high mass range at $z = 0$, it accurately predicts the halo mass functions for other ETHOS models in different mass regimes at higher redshifts/earlier times.

The prediction of the halo abundance at high redshifts is particularly interesting. Using the observed abundance of ultra-faint high redshift galaxies (Menci et al., 2017; Livermore et al., 2017), we apply our analytical model to constrain the interacting DM models and compare the results with those derived from the Lyman-α observations (Huo et al., 2018). In addition, we use the model to study the impact of suppression in matter power spectrum on the low mass tail of the stellar-halo mass relation. We take the observed stellar mass function at $z = 4$ from Song et al. (2016) and perform an “abundance matching" analysis (Vale and Ostriker, 2004, 2006; Moster et al., 2010; Guo et al., 2010; Moster et al., 2013; Behroozi et al., 2013) to assign halo mass to the observed galaxies at the redshift for each of the DM models considered in this work. Our goal is to show how these non-trivial DM interactions changes DM content of galactic systems through the matching procedure.

The structure of this chapter is organized as follows: In Sec. 5.2, we introduce interacting DM models and ingredients for constructing halo mass functions in the Press-Schechter framework, and we also discuss cosmological simulations carried out in this work. We present our main results in Sec. 5.3 and summarize in Sec. 5.4.

5.2 Methodology

We work within the framework of the Press-Schechter formalism to compute halo mass functions. We use the following cosmological parameters: $\Omega_m = 0.302$, $\Omega_\Lambda = 0.698$, $\Omega_b = 0.046$,

$h = 0.69$, $\sigma_8 = 0.839$, and $n_s = 0.967$ consistent with Planck Collaboration et al. (2016). Throughout this work, we define halo mass as the mass enclosed by a sphere with average density equal to the virial overdensity $\Delta_{vir}(z)$ (Bryan and Norman, 1998) times the critical density. This mass definition resembles closely the redshift evolution predicted by the analytic model Despali et al. (2016). The Press-Schechter formalism requires three elements, i.e., the matter power spectrum, barrier height in the excursion set approach and the solution for the distribution of first crossing events, as we will discuss in detail later. In our analysis, we use cosmological simulations in Vogelsberger et al. (2016, hereafter V16) to calibrate the fitting formula for distribution of first crossing in mass scales above 3×10^{10} $M_\odot$.

In order to resolve halo abundances on lower mass scales and at different redshifts, we run cosmological N-body simulations for the benchmark models in V16. Note that we do not include DM-DM self-interactions in the simulations, as their effect is negligible on the abundance of the haloes. We compute the power spectra using a modified version of the Boltzmann code CAMB (Lewis and Bridle, 2002; Cyr-Racine et al., 2016) to include DM-dark radiation interactions, and generate the initial conditions at $z = 127$ with two different periodic box sizes L = 10 Mpc/h and 20 Mpc/h with the code N-GenIC (Springel et al., 2001; Springel, 2005). Our simulations are performed using 256^3 and 512^3 particles yielding DM particle mass resolutions of 9.04×10^5 $M_\odot$ and 7.18×10^6 $M_\odot$ and spatial resolutions of $\epsilon = 2.5$ kpc/h and 5 kpc/h (Plummer-equivalent softening length). In order to compare the halo mass functions predicted in the Press-Schechter model, we use results from simulations with L=10 Mpc/h and $m_p = 7.18 \times 10^6 M_\odot$ (referred to as L_{10}). Other simulations are used to perform convergence and resolution tests as shown in Appendix 5.5.1. Table 5.1 summarizes the details of our simulations. We use the code Arepo (Springel, 2010) to run simulations. Haloes and subhaloes are identified by the friends-of-friends (Davis et al., 1985) and SUBFIND (Springel et al., 2001) algorithms which we use to construct mass functions.

Table 5.1: Parameters for our cosmological simulations.

DM model	L (Mpc/h)	$N_{\rm p}$	$m_{\rm p}(\mathrm{M}_\odot)$
ETHOS1	10	256^3	7.18×10^6
ETHOS1	10	512^3	9.04×10^5
ETHOS2	10	256^3	7.18×10^6
ETHOS3	10	256^3	7.18×10^6
ETHOS3	20	512^3	7.18×10^6

Note. The second column (L) is the simulation box size in Mpc/h, the third column ($N_{\rm p}$) is the total number of particles, and the last column ($m_{\rm p}$) is the mass resolution in $\mathrm{M}_\odot$. Our simulations take matter power spectra of the ethos models, but do not include DM self-interactions that have negligible effects on the halo mass functions for the mass scales that we are interested.

5.2.1 Power spectrum

In Fig. 5.1, we show the power spectra for the benchmark models in V16, as well as one in Huo et al. (2018). In these models, DM particles are strongly coupled to relativistic particles ("dark radiation") in the early universe which results in oscillatory features in their power spectra, analogous to baryonic acoustic oscillations. The damping effect on the power spectra can be characterized by the kinetic decoupling temperature $T_{\rm kd}$ (van den Aarssen et al., 2012; Cyr-Racine et al., 2016; Huo et al., 2018), at which DM particles kinematically decouple from the radiation plasma ($T_{\rm kd}$ here is defined in terms of the photon temperature, as in Feng et al. (2009)). For three ETHOS models, their kinetic decoupling temperatures are $T_{\rm kd} = 0.19$ keV (ETHOS1), 0.33 keV (ETHOS2) and 0.51 keV (ETHOS3), and the model taken from Huo et al. (2018) has $T_{\rm kd} = 1$ keV. Fig. 5.1 that the suppression on the power spectrum becomes significant as $T_{\rm kd}$ decreases. This is because small $T_{\rm kd}$ indicates a tight coupling between DM and dark radiation, leading to a strong damping effect on the power spectrum. Since the shape and amplitude of DAOs depends on the underlying particle physics of the DM models mostly through the combination that results in the kinetic decoupling temperature, $T_{\rm kd}$ is a viable single parameter to categorize different interacting DM models.

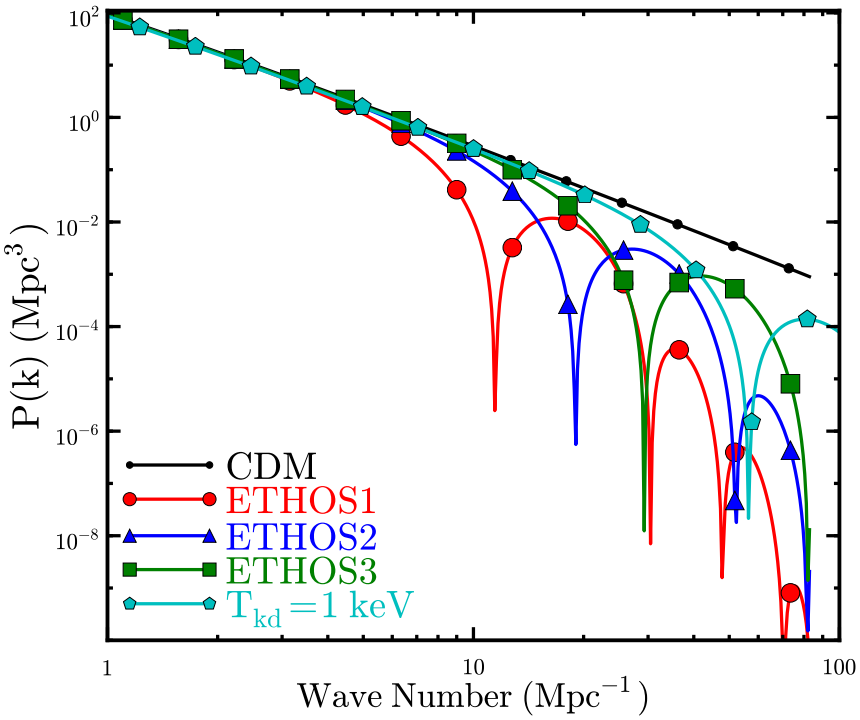

Figure 5.1: Matter power spectra of CDM and interacting DM models, i.e., ETHOS1 ($T_{\rm kd}$ = 0.19 keV), ETHOS2 ($T_{\rm kd}$ = 0.33 keV) and ETHOS3 ($T_{\rm kd}$ = 0.51 keV) from V16, as well as a model from Huo et al. (2018) ($T_{\rm kd}$ = 1 keV).

5.2.2 Mass variance and window function

An important ingredient in the Press-Schechter formalism is the mean-squared amplitude of density fluctuations,

$$\sigma^2(M) \equiv S(M) = \frac{1}{2\pi^2}\int_0^\infty {\rm d}k k^2 P(k)\widetilde{W}^2(k), \tag{5.1}$$

where $\widetilde{W}(k)$ is the Fourier transform of the window function. In general, we need to fix $\widetilde{W}(k)$ by comparing the model predictions with N-body simulations. The top-hat filer is a commonly used window function that can successfully reproduce the halo mass function for CDM, see, e.g., Tinker et al. (2008); Despali et al. (2016). It does, however, produce spurious haloes for DM models with a suppressed power spectrum such as warm DM (Benson et al., 2013). An

alternative is the sharp-k filter

$$\widetilde{W}_{\text{sharp-k}}(k) = \begin{cases} 1 & \text{if } k \leq k_{\text{s}}(M) \\ \\ 0 & \text{if } k > k_{\text{s}}(M) \end{cases}, \tag{5.2}$$

where $k_{\text{s}} = c/R_0$ with $R_0 \equiv (3M/4\pi\rho_{\text{mean}})^{1/3}$. The free parameter c can be fixed by comparing with simulations. However, the sharp-k filter fails to reproduce the halo abundance for the interacting DM models we consider, since it neglects contributions of the modes larger than k_{s}, as we will discuss in the next section and Appendix 5.5.2. Leo et al. (2018) proposed another window function, named as the smooth filter,

$$\widetilde{W}_{\text{smooth}}(k) = \frac{1}{1 + (k/k_{\text{s}})^{\beta}}, \tag{5.3}$$

which has two free parameters β and c (implicit in k_{s}) to be fixed. For large modes (small k), it approaches to 1, similar to the top-hat and sharp-k filters. While for small modes (large k), it has non-zero values. Thus, it takes into account large k modes, which are absent in the sharp-k case. On the other hand, we can eliminate spurious haloes by choosing comparably large value of β, avoiding the shortcomings of the top-hat filter. In this work, we will take the smooth filter for our main results.

Lastly, we comment on the filter-independent approach proposed in Chan et al. (2017). It constructs the shape of the window function using the density profiles of overdense regions, destined to collapse to halos, in the initial linear density field. While this approach provides an independent way to directly measure the shape of the filter, we find that for the interacting DM models it tends to produce spurious haloes. This is because the reconstructed effective filter is essentially the top-hat filter but with edges smoothed by a Gaussian profile and it over predicts the halo abundance for DM models with a cutoff in their power spectra.

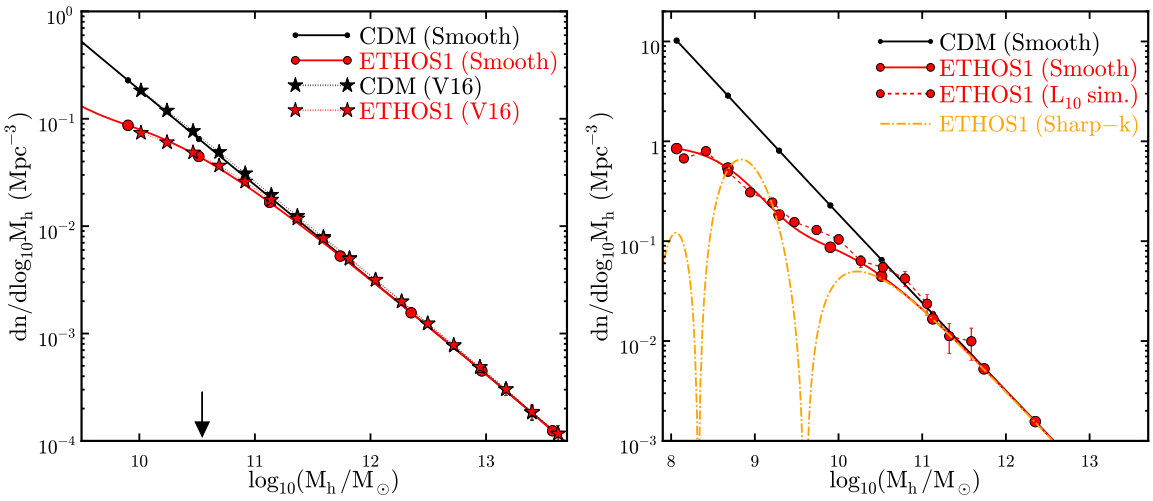

Figure 5.2: Top: Halo mass functions from the calibrated Press-Schechter model with the smooth filter (solid) and the simulations (dashed) in V16. Error bars are estimated by assuming that the halo abundance in each mass bin follows Poisson statistics. The black arrow shows 300 times particle mass $m_{\rm p}$ for simulations inV16, the lower limit of the mass range we considered for our calibration analysis. Bottom: halo mass functions from the analytical model for ETHOS1 with the smooth (red solid) and sharp-k filters (orange dot-dashed) vs. $\mathrm{L_{10}}$ simulations carried out in this work (red circles). Our analytical predictions agree with the simulations for the smooth filter. While, the sharp-k filter fails to reproduce the simulation results in the low-mass regimes.

5.3 Results

5.3.1 Calibrating the model for mass functions

We employ the fitting formula for the distribution of first crossing (Sheth and Tormen, 1999; Sheth et al., 2001)

$$\nu f(\nu) = 2A_0\Big(1+\frac{1}{\nu'^{2p}}\Big)\Big(\frac{\nu'^2}{2\pi}\Big)^{1/2}\mathrm{e}^{-\frac{\nu'^2}{2}}, \tag{5.4}$$

where $\nu' = \sqrt{a}\ \nu$ and $\nu = \delta_c/\sigma(M)$, to compute the number density of collapsed overdensity peaks per logarithmic mass bins

$$\frac{\mathrm{d}n}{\mathrm{d}\ln(M)} = \frac{1}{2}\frac{\rho_{\rm mean}}{M}\nu f(\nu)\frac{\mathrm{d}\log(\nu)}{\mathrm{d}\log(M)}. \tag{5.5}$$

We determine the parameters (A_0, a, p) along with c and β in Eq. 5.3 by calibrating the analytical predictions to the N-body simulations. To fix (c, β) completely, it is necessary to *simultaneously* include both CDM and interacting DM halo abundances in the calibration analysis.

We compute analytical halo mass functions and perform a χ^2 analysis using the joint data points of the CDM and ETHOS1 mass functions from simulations in V16. We assume that the abundance of the simulated haloes in each mass bin follows a Poisson distribution and, most importantly, we only include in the calibration those mass bins larger than $300m_{\rm p} \simeq 3.34 \times 10^{10}$ $\mathrm{M}_\odot$, where $m_{\rm p} \simeq 1.13 \times 10^8$ $\mathrm{M}_\odot$ is the particle mass in the ETHOS simulations. We also require the mass bins to contain at least 30 haloes to minimize the noise from cosmic variance at the high-mass end. Our best-fit values are $(A_0, a, p) = (0.3, 0.81, 0.3)$ and $(c, \beta) = (3.7, 3.5)$ for the smooth filter, see Fig. 5.2 (top) for the comparison. We emphasize that although the fit is performed for haloes more massive than $M_{\rm h} \sim 3 \times 10^{10}$ $\mathrm{M}_\odot$ in CDM and ETHOS1 simulations at $z = 0$, we will use the model to *predict* the abundances of lower mass haloes as well, for different ETHOS models at different redshifts and for wider range of halo masses.

To better understand the effects of different filters on the predicted halo mass functions, we compare our simulated results (L_{10}) with analytical predictions for the smooth and sharp-k filters given a wider range of halos masses, as shown in Fig. 5.2 (bottom). Although the analytical mass function with the sharp-k filter ($c = 3.2$) is in reasonable agreement with the simulated one at the high-mass end, it exhibits significant oscillatory features and fails in low-mass halo regimes. Indeed, for the sharp-k filter, $\mathrm{d}n(M)/\mathrm{d}\log_{10}(M) \propto P(k_{\rm s})$, i.e., the shape of mass function closely follows the power spectrum. On the other hand, the smooth filter smoothes out the dark acoustic peaks and the result agrees with the simulations remarkably well. It has been shown that non-linear evolution of the modes erases the peaks in the power spectrum predicted in interacting DM models (Buckley et al., 2014), resulting in a smooth decay in halo number density. It seems the smooth filter accurately captures this effect by including contributions of all modes to the mass variance, as we have shown.

Fig. 5.3 shows excellent agreement between our analytical predictions and L_{10} simulations introduced in Sec. 5.2 at different redshifts. We emphasize again that our model parameters are

constrained to reproduce ETHOS1 and CDM simulations at $z = 0$ for halo masses larger than $\sim 3 \times 10^{10}$ $M_\odot$, and the higher redshift and lower-mass comparison demonstrate how well this single model extends to these regimes. The analytical model slightly over predicts the number density of haloes at $z = 6$. This 20–30% discrepancy toward high redshifts has been noted in other works (e.g. Courtin et al., 2011; Despali et al., 2016). It is evident that the halo abundance is more suppressed for DM models with a lower kinetic decoupling temperature, as expected.

Our model will allow us to make predictions for halo abundances at low and high redshifts and for different cosmology assumptions. This is particularly interesting in light of the availability of the Wide Field Camera 3 (WFC3) on the Hubble Space Telescope (HST) combined with gravitational lensing effects from clusters in the Hubble Frontier Fields, which have provided exquisite measurements of the galaxy luminosity function on the UV down to magnitudes of $M_{UV} \simeq -15$ (e.g. see McLure et al., 2013; Bouwens et al., 2015; Finkelstein et al., 2015), comparable to what is possible only within the Local Volume. In what follows, we take advantage of these high-z, volume-complete observational constraints for faint galaxies and use our analytical approach to compare with the abundance of low mass haloes predicted for different DM models.

5.3.2 Constraining the DM models with galaxy abundance at $z = 6$

In Fig. 5.4, we show the cumulative number density of haloes $n(> M)$ derived from our analytical model, together with the constraints on the number density of galaxies from Menci et al. (2017), which is based on the luminosity functions in Livermore et al. (2017). The horizontal lines denote the confidence levels of the observational constraints. In the shaded region, where the mass is below 10^8 $M_\odot$, we expect DM haloes to have lost most of their baryons due to photoheating caused by the ionizing background UV radiation at $z = 6$ (see, e.g., Okamoto et al., 2008; Ocvirk et al., 2016). We see that ETHOS1 and ETHOS2 are outside of the 3σ and 2σ limits, respectively, and ETHOS3 is marginally consistent within the 1σ limit, Whilst the model with $T_{kd} = 1$ keV is fully within the observational constraints. Interestingly, these lower bounds

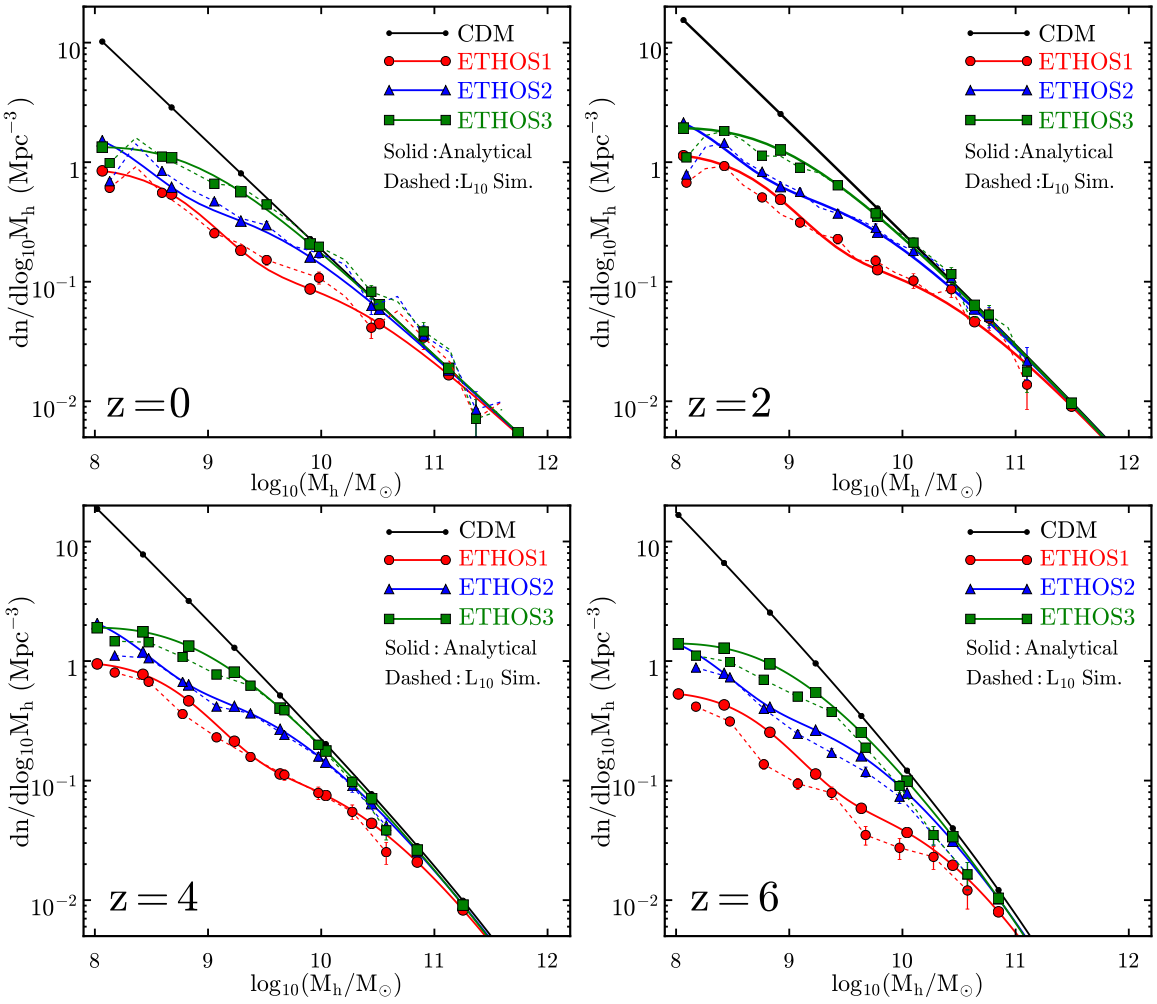

Figure 5.3: Analytical halo mass functions (solid) vs. simulation results (dashed) at four different redshifts $z = 0$, 2, 4 and 6. The analytical model, after calibrated with the simulated mass functions of CDM and ETHOS1 down to 3×10^{10} $M_\odot$ at $z = 0$, can successfully reproduce the simulations with halo masses down to 10^8 $M_\odot$ at different redshifts for two other interacting DM models, ETHOS2 and ETHOS3. It slightly over predicts the halo abundances at $z = 6$.

on $T_{\rm kd}$ from the galaxy counts are coincident with those from the Lyman-α forest observations (Huo et al., 2018).

5.3.3 Stellar mass-halo mass relation

As another application, we derive the stellar-halo mass relation for the interacting DM models using the abundance matching technique, i.e., matching cumulative halo plus subhalo mass

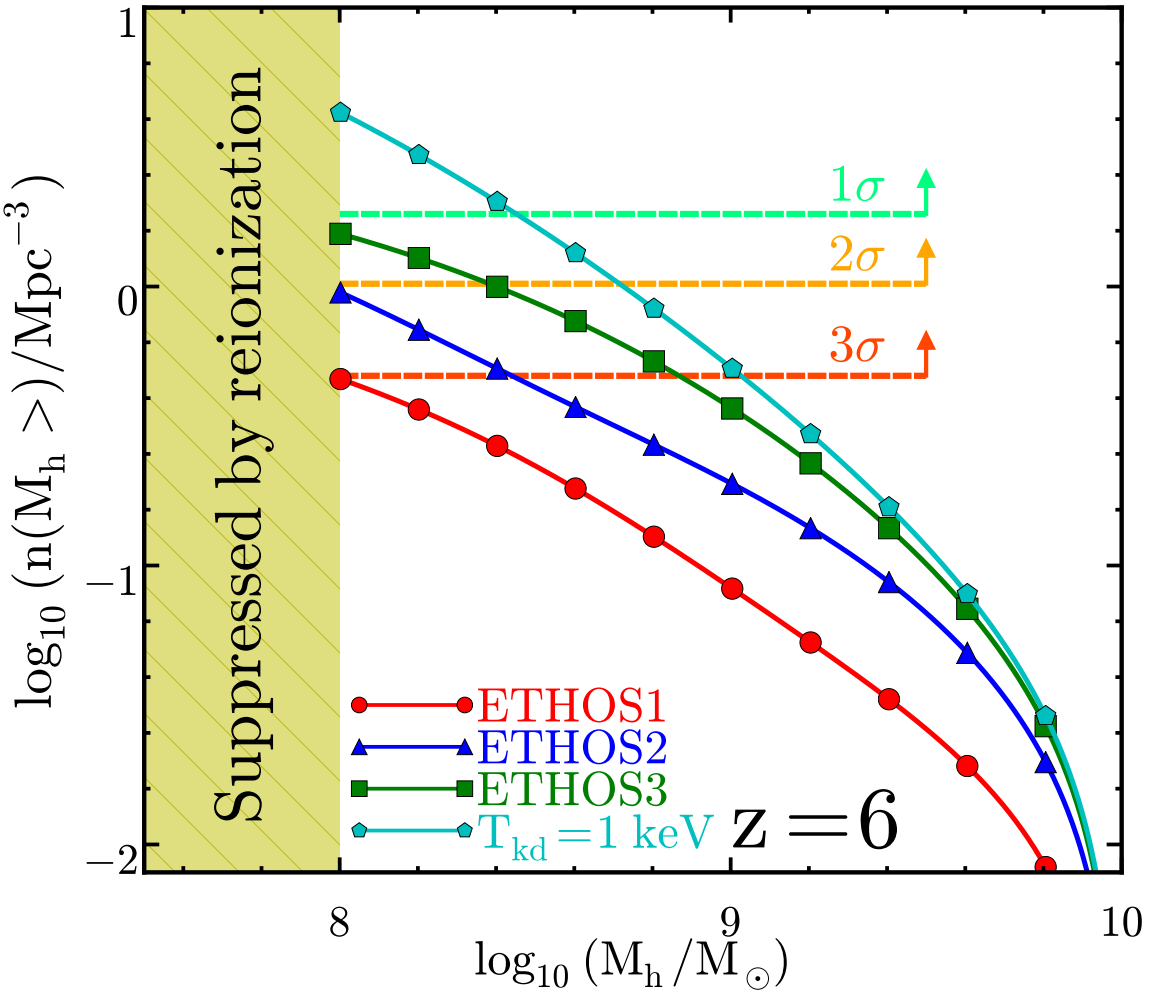

Figure 5.4: Cumulative number density of haloes, $n(>M)$, for different interacting DM models vs. cumulative galaxy number density estimated from observed UV luminosity function $n_{\rm obs}(>M)$ at $z = 6$ (Menci et al., 2016), where the horizontal lines denote the confidence levels of the lower bound on the galaxy counts. The shaded region denotes the halo mass scales, i.e. $M_{\rm h} \leq 10^8$ M$_\odot$, which have lost most of their baryons due to background UV radiation (Okamoto et al., 2008; Ocvirk et al., 2016).

functions to the observed number density of galaxies in each stellar mass bin,

$$n(>M_*) = n_{\rm h}(>M) + n_{\rm sh}(>M). \tag{5.6}$$

Our analytical model does not include the presence of subhaloes deemed subdominant but important for these kinds of calculations. We therefore aim at estimating their effects as follows.

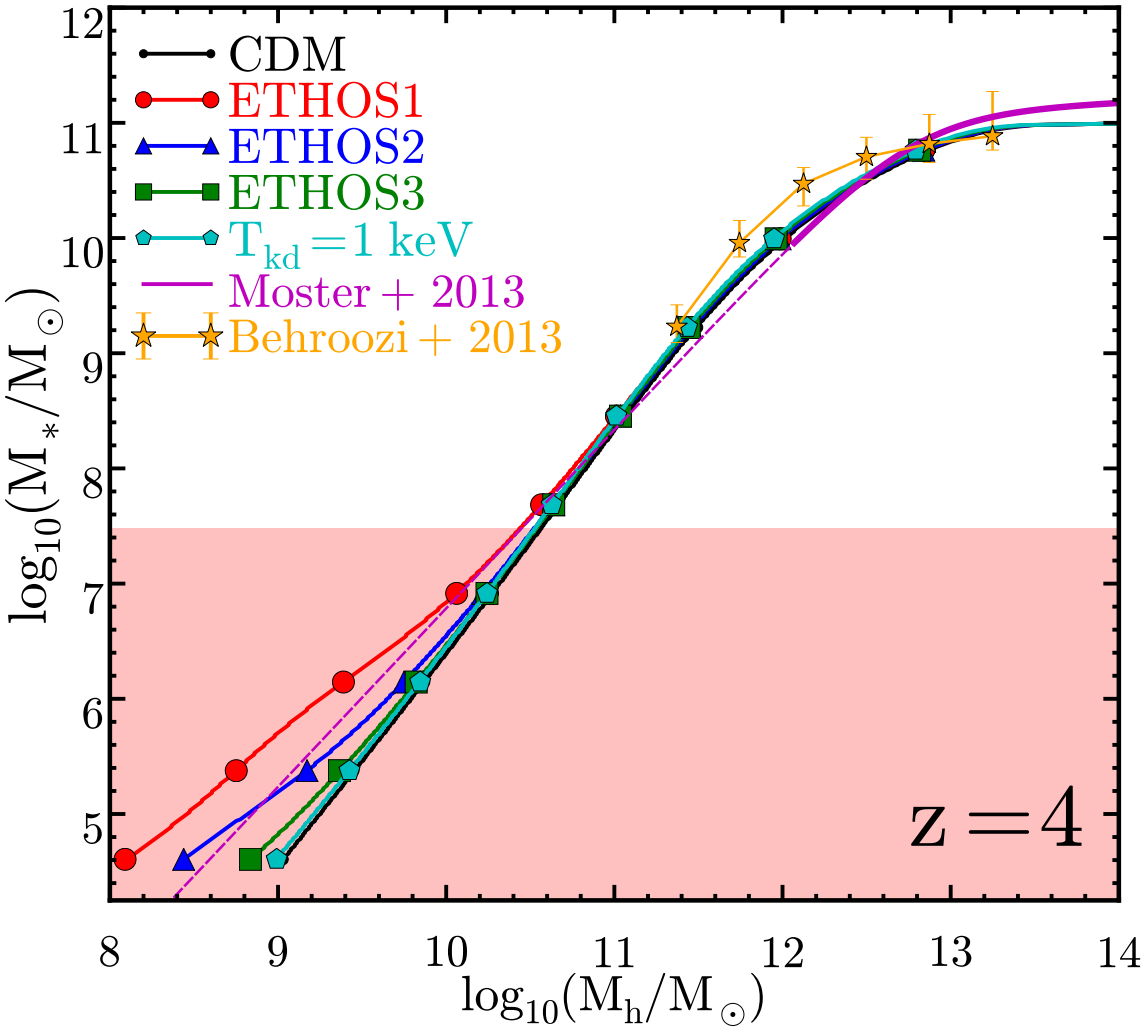

Figure 5.5: Predicted stellar-halo mass relations for CDM, ETHOS models and the DM model with $T_{kd} = 1$ keV at $z = 4$. We also show the results for CDM in Behroozi et al. (2013) and Moster et al. (2013) (magenta dashed: extrapolated). The shaded region indicates the mass scales with the extrapolated stellar mass function.

The CDM subhalo mass function in each mass is calculated as

$$n_{\mathrm{sh;CDM}}(m,z) = \int_0^\infty N(m|M,z) n_{\mathrm{h}}(M,z) \mathrm{d}M, \tag{5.7}$$

where $N(m|M,z)\mathrm{d}m = N(m|M,z=0)f(z)\mathrm{d}m$ is the total number of subhaloes in the mass range $m + \mathrm{d}m$ for a parent halo with mass M at given redshift z. We take the analytical formula

for the subhalo distribution for a given parent halo at $z = 0$ from Giocoli et al. (2008),

$$N(m|M, z = 0) = \frac{N_0}{m} x^{-\alpha} \mathrm{e}^{-6.283x^3}, x = \frac{m}{\alpha M}, \tag{5.8}$$

where $\alpha = 0.8$ and $N_0 = 0.21$. To extend this to earlier times we normalise Eq. 5.8 by the redshift evolution factor $f(z) \equiv f_{\rm sub}(z)/f_{\rm sub}(z = 0) = 1 - z/6$ (Conroy and Wechsler, 2009) and neglect mild dependence of $f(z)$ on the halo mass. Note that the subhalo distribution function given in Eq. 5.8 is calibrated with CDM simulations. In principle, one needs to recalibrate it for the interacting DM models as well. For simplicity, we assume the depletion rate of subhaloes in the non-CDM models is as the same as that of main halos, and estimate the subhalo distribution as

$$n_{\rm sh;non\text{-}CDM}(m, z) = \frac{n_{\rm h;non\text{-}CDM}(M, z)}{n_{\rm h;CDM}(M, z)} n_{\rm sh,CDM}(m, z). \tag{5.9}$$

We also neglect the effect on the subhalo mass function caused by the finite resolution of simulations (Guo and White, 2014). Since subhaloes have sub-dominant contributions to the total mass function, we expect that our estimate of $n_{\rm sh;non\text{-}CDM}(m, z)$ will provide a reasonable approximation.

For the number density of observed galaxies, we take the Schechter (Schechter, 1976) function

$$\frac{\mathrm{d}n(M_*)}{\mathrm{d}\log_{10}(M_*)} = \ln(10)\phi^* \mathrm{e}^{-\frac{M_*}{M_0}} \Big(\frac{M_*}{M_0}\Big)^{\alpha+1}, \tag{5.10}$$

where $(\log_{10}(M_0), \alpha, \log_{10}(\phi^*)) = (10.5, -1.55, -3.59)$ are the best-ft values after fitting to the stellar mass function for their sample of galaxies at $z \sim 4$ (Song et al., 2016).

In Fig. 5.5, we show the stellar-halo mass relations for the DM models we consider after matching the number density of galaxies to that of haloes. For comparison, we also plot the CDM results from Behroozi et al. (2013) and Moster et al. (2013) (magenta solid: stellar-halo mass relation in the mass range where observational data points exist; magenta dashed: extrapolation to lower masses). Overall, our result for CDM is in reasonable agreement with previous works in the mass region spanned by the observational data points. The small offset could be caused

by different choices of galaxy samples, halo mass definitions and window functions. We have checked that using a top-hat filter slightly improves the agreement for the CDM case.

The suppression of the halo mass function results in more massive galaxies inhabiting a given DM halo or, in other words, a higher star formation efficiency in the low mass end. This can be seen clearly for the interacting DM models in Fig. 5.5, with ETHOS1 being the most strongly suppressed and therefore exhibiting larger deviations from the CDM results. The red shaded region shows the regime where the observed luminosity function has been extrapolated using the Schechter function. Our results indicate that significant deviations from the other models in the case of ETHOS1 could be achieved by reaching observational completeness in the range $M_* \sim 10^6$-10^7 $M_\odot$, about a dex fainter than current limits. On the other hand, the limits are fainter for ETHOS2 ($M_* \sim 10^5$ $M_\odot$), while ETHOS3 and the DM model with $T_{\rm kd} = 1$ keV seem indistinguishable from CDM stellar-halo mass relation down to very faint limits of $M_* \sim 10^4$ $M_\odot$. The effort, coupled with an alternative measurement of halo masses, such as clustering and kinematics, could be used to further test DM models with suppressed matter power spectra. And our methodology and prescriptions to fast compute halo mass functions may prove useful for these kinds of assessments.

5.4 Summary

We have used the Press-Schechter formalism to study the halo mass functions for interacting DM models with matter power spectra damped by dark acoustic oscillations. Taking three ETHOS models as benchmark examples, we have demonstrated that this analytical approach can accurately reproduce the result of N-body simulation results. The choice of a proper window function plays a critical role in such as success. We found the smooth filter proposed in Leo et al. (2018) works well in capturing relevant physics. The sharp-k filter, despite being a viable choice for warm DM, fails in the low-mass regimes for interacting DM. Our model parameters are constrained to match the CDM and ETHOS1 simulations at the high mass end of the $z = 0$ mass functions. In order to validate these we performed our own cosmological simulations with

improved mass resolution. Our results indicate that the Press-Schechter formalism with the smooth filter provides a simple but powerful tool to understand the suppression effect on the halo mass functions induced by DM-dark radiation interactions, presented in many new DM models beyond the CDM paradigm.

We have further applied our calibrated model to derive constraints on the DM models using the observed stellar mass functions at high redshifts available in the literature. After comparing the cumulative number density of haloes predicted in the DM models with that of galaxies inferred from the measured UV luminosity functions at $z = 6$ (Menci et al., 2017; Livermore et al., 2017), we found both ETHOS1 ($T_{\rm kd} = 0.19$ keV) and ETHOS2 ($T_{\rm kd} = 0.33$ keV) strongly disfavored, as they produce too few halos due to host the observed galaxies, due to strong dark acoustic damping. While ETHOS3 ($T_{\rm kd} = 0.51$ keV) and the model with $T_{\rm kd} = 1$ keV are within the observational constraints. Interestingly, these UV luminosity constraints on the kinetic decoupling temperature of the interacting DM models are similar to those from the Lyman-α forest measurements reported in Huo et al. (2018).

We have also performed an abundance matching analysis to derive the stellar-halo mass relation for the interacting DM models, using the observed stellar mass functions of galaxies at $z = 4$ (Song et al., 2016). Our results indicate appreciable suppression in the halo mass of hosted galaxies at $M_* \lesssim 10^5$-10^7 $M_\odot$ for ETHOS1 and ETHOS2 models, and ETHOS3 shows mild suppression of halo mass only in the low-mass tail $M_* \lesssim 10^5$ $M_\odot$. In contrast, the DM model with $T_{\rm kd} = 1$ keV is almost indistinguishable from CDM. While it is of great interest to further push observational limits to dwarf galaxies below $M_* \sim 10^5$ $M_\odot$, our model provides a valuable tool to explore interacting DM models quickly and with low computational demands; facilitating the comparison between observations and theoretical expectations in the quest to determine the nature of dark matter.

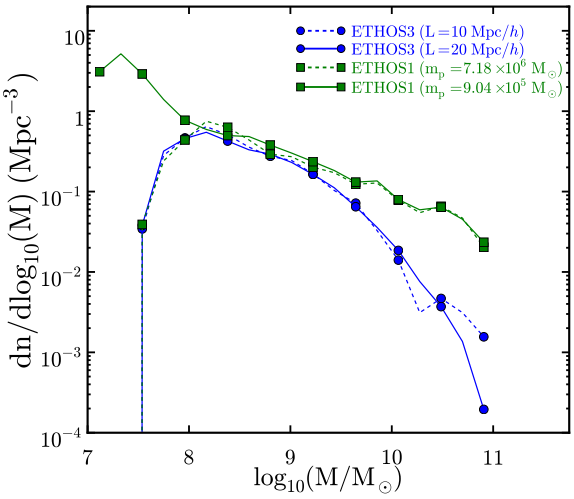

Figure 5.6: Convergence test of our cosmological simulations for two different DM models at different redshifts. Green lines denote the halo mass functions for ETHOS1 with box size $\mathrm{L} = 10$ Mpc/h and particle mass resolution $m_\mathrm{p} = 7.18 \times 10^6$ $\mathrm{M}_\odot$ (dashed) and 9.04×10^5 $\mathrm{M}_\odot$ (solid) at $z = 0.2$. Blue lines denote ETHOS3 simulations with box sizes $\mathrm{L} = 10$ Mpc/h (dashed) and 20 Mpc/h (solid) and the same mass resolution $m_\mathrm{p} = 7.18 \times 10^6$ $\mathrm{M}_\odot$ at $z = 8$.

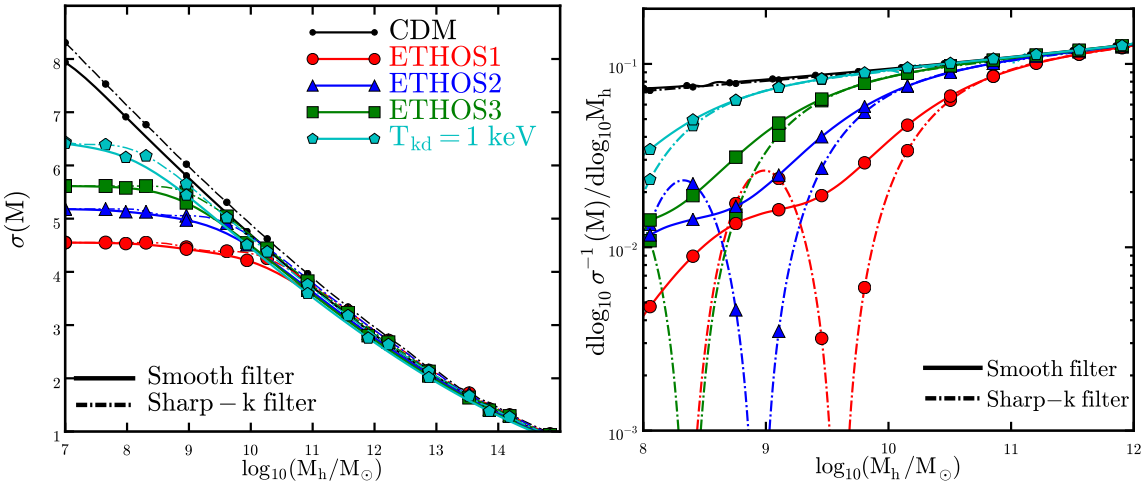

Figure 5.7: Top: Mass variance calculated for the interacting DM models with the sharp-k (dot-dashed) and smooth filters (solid). Bottom: $\mathrm{d}\log_{10}\sigma^{-1}(M)/\mathrm{d}\log_{10} M$ for the DM models. Marker styles and color schemes are the same as in Fig. 5.1.

5.5 Appendix

5.5.1 Convergence and resolution test

We test the numerical convergence of our simulations. In Fig. 5.6, we show simulated halo mass functions for ETHOS1 with two different levels of mass resolution: $m_{\rm p} = 7.18 \times 10^6$ M$_\odot$ (green dashed) and 9.04×10^5 M$_\odot$ (green solid) at redshift $z \sim 0.2$. The cosmological box size is L = 10 Mpc. We find good numerical convergence down to 10^8 M$_\odot$. For lower halo masses, the low resolution simulation cannot populate halos, while the high resolution one suffers from spurious haloes. We also test the effect of cosmic variance by comparing the halo mass function for two ETHOS3 simulations with the same mass resolution ($m_{\rm p} = 7.18 \times 10^6$ M$_\odot$) but with different box sizes L = 10 Mpc/h (blue dashed) and 20 Mpc/h (blue solid) at $z = 8$. They are well converged toward the low-mass end, but deviate for high halo masses because the simulations with a small box size suffers from cosmic variance. We find good convergence of the mass functions in the mass range 10^8–10^{10} M$_\odot$, and we take this range in our analysis in Sec. 3.

5.5.2 Mass variance and window function-continued

In Fig. 5.7 (top), we show the mass variance for the DM models considered in this work for both the sharp-k space ($c = 3.2$; dot-dashed) and smooth filters ($c = 3.7$ and $\beta = 3.5$; solid). As we have discussed in the Sec. 5.3.1, the prediction of the analytical model in the low-mass regime is sensitive to the choice of the filter. To demonstrate the origin of this effect, we compute $\mathrm{d}\log_{10}\sigma^{-1}(M)/\mathrm{d}\log_{10}M$, the key factor in Eq. 5.5, for each DM model with both smooth and sharp-k filters, as shown in Fig. 5.7 (bottom). When computed with the sharp-k filter, the factor has an oscillatory feature in the low mass end, a reminiscent of the acoustic peaks in the power spectrum.

Chapter 6

Conclusions

Throughout my Ph.D. I studied the effects of non-gravitational DM interactions on the formation and abundance of DM halos and their substructures. To this end, I used a combination of numerical simulations and analytical methods. My findings can be summarized in four different sections as follows:

6.1 Creating diverse rotation curves via baryonic and dark matter self-interaction effects

We performed a series of isolated N-body simulations for CDM and SIDM models with a wide range of halo masses $V_{\rm max} = 30 - 250$ kms^{-1} to study the shape of galactic rotation curves in the SIDM models. The stellar disk is modeled as an static Miyamoto-Nagai potential. The DM distribution at the center of each simulated system is quantified via its circular velocity at 2 kpc, $V_{\rm circ}(2\ {\rm kpc})$. We compared the scatter in the plane of $V_{\rm circ}(2\ {\rm kpc})$-$V_{\rm max}$ for simulated halos and observed galaxies. According to our results, the spread in $V_{\rm circ}(2\ {\rm kpc})$ for a fixed $V_{\rm max}$ in SIDM models is larger than the CDM counterpart.

We have performed simulations to provide individual fits to the most extreme cases, UGC5721 and IC2574, with either a very cuspy or cored inner circular velocity, both with similar $V_{\rm max} \approx$ 80 kms^{-1}. These halos can be fitted well in the SIDM models with a constant cross section 3

cm^2g^{-1}, in good agreement with the regime allowed by independent Tully-Fisher constraints. The SIDM models may offer a closer match to the diversity observed in galaxies than the traditional CDM.

6.2 The impact of stellar disks on the shape and density profile of dark matter halos

We performed a series of controlled N-body simulations to study the impact of baryonic distributions on the evolution and final distribution of DM particles in the SIDM halos. The 3D shape of the DM density profiles is sensitive to not only the strength of DM self-interactions, modeled as σ/m, but also the baryonic distribution. A sub-dominant contribution of baryons to the total gravitational potential leads to a constant DM density core and an almost spherical halo shape. Significant contribution from baryons, on the other hand, causes a more rapid thermalization of the central region which in turn results in a high-central density and flattened shape for the DM distribution, similar to the shape of baryons.

We applied our setup to the special case of the MW. We performed two simulations with the CDM and SIDM models for a galactic system that comprises a DM halo, a stellar disk, and a bulge. Our simulations indicate that the effect of the baryons counteracts those of the self-interactions, resulting in a relatively high density inner cusp. Our model predicts that the addition of self interactions and central baryons will tend to make dark matter halos spherical, in good agreement with the current estimates of our own Galaxy.

6.3 Self-interacting dark matter subhalos in the Milky Way's tides

The DM content of the MW satellites can be inferred from their stellar kinematic measurements. Interestingly, the luminous MW satellites show a large scatter in their central DM densities. Using numerical simulations, we conducted the first study to investigate the tidal evolution of the SIDM subhalos associated with the MW Dwarf Spheroidals. We modeled the host by a static

potential and considered subhalos with different orbits and pre-infall halo parameters. In the presence of DM self-interactions *and* tidal fields, the central DM density in the subhalo can vary from shallow to cuspy. While these subhalos suffer mass loss at all radii, a high pre-infall halo concentration can trigger core-collapse, developing a high central DM density. On the other hand, most of the accreted subhalos with lower pre-infall concentrations never enter the core-collapse phase. For these subhalos, the interplay between tidal fields and DM self-interactions establishes a shallow density core.

using two examples of the most extreme MW Dwarf Spheroidals, we constructed their orbits and considered their evolutions under tidal fields of a MW-like halo. Interestingly, a constant cross section with $\sigma/m = 3$ cm^{2}g^{-1} can reproduce the observed DM density profiles. The novel mechanism proposed and implemented in our simulations can well explain the diversity observed in halo properties of the MW satellites.

6.4 Halo Abundance in self-interacting dark matter models

Although DM-DM self-interactions only changes the distribution of DM particles at the center of the halos, these SIDM models can be refined to alter the overall halo abundance in specific mass regimes. I led a project which targeted the computation of halo abundance in models with an extra relativistic particle such that it can scatter off from DM. These DM-dark photon interactions will suppress the matter power spectrum at early time and consequently deplete the abundance of collapsed halos in corresponding mass regime at later times. After a calibration to the cosmological numerical simulations in the mass range $M_{\rm vir} \geq 10^{10}\ M_\odot$, we verified that our model also predicts the correct halo abundance in a lower mass regime, $M_{\rm vir} \sim 10^8$–$10^{10}\ M_\odot$. Our calibrated model was used to constrain the interaction rate between DM and dark photons. We concluded that DM models with “kinetic decoupling temperature", $T_{\rm kd}$ less than 0.5 keV are disfavored based on galaxy counts at $z = 6$. Additionally, we computed the stellar-halo mass relation through abundance matching. Our analysis shows that the suppression in the matter power spectrum must be compensated with a higher star formation efficiency to fully

capture a one-to-one mapping between galaxies and halos. Our simulations predict that to potentially detect any effects in the dwarf halo abundances, which depend on the channels of DM interactions, observations should reach stellar masses of $10^5 - 10^6\ M_\odot$.

In this Dissertation, I studied different DM interaction channels and their impacts on halo formation and galaxy evolution. I discussed how inclusion of the baryonic gravitational potentials and/or environmental effects into SIDM numerical simulations can lead to diverse 3D shapes and central DM densities. I also developed a Press-Schechter analytical model to compute the halo abundance in the SIDM models. Overall, I conclude that SIDM models provide a novel explanation for some of the small-scale puzzles of the cosmology, which can be further tested by the upcoming generations of surveys.

References

Abadi, M. G., Navarro, J. F., Fardal, M., Babul, A., and Steinmetz, M.: 2010, *MNRAS* **407**, 435

Abazajian, K. N.: 2017, *physical Reports* **711**, 1

Addison, G. E., Watts, D. J., Bennett, C. L., Halpern, M., Hinshaw, G., and Weiland, J. L.: 2018, *ApJ* **853**, 119

Allgood, B., Flores, R. A., Primack, J. R., Kravtsov, A. V., Wechsler, R. H., Faltenbacher, A., and Bullock, J. S.: 2006, *MNRAS* **367**, 1781

Balberg, S., Shapiro, S. L., and Inagaki, S.: 2002, *ApJ* **568**, 475

Behroozi, P. S., Wechsler, R. H., and Conroy, C.: 2013, *ApJ* **770**, 57

Benson, A. J., Farahi, A., Cole, S., Moustakas, L. A., Jenkins, A., Lovell, M., Kennedy, R., Helly, J., and Frenk, C.: 2013, *MNRAS* **428**, 1774

Binney, J., Gerhard, O., and Silk, J.: 2001, *MNRAS* **321(3)**, 471

Binney, J. and Tremaine, S.: 2008, *Galactic Dynamics: Second Edition*, Princeton University Press

Blais-Ouellette, S., Amram, P., and Carignan, C.: 2001, *The Astronomical Journal* **121(4)**, 1952

Blumenthal, G. R., Faber, S. M., Flores, R., and Primack, J. R.: 1986, *ApJ* **301**, 27

Boddy, K. K., Feng, J. L., Kaplinghat, M., and Tait, T. M. P.: 2014, *physical Review D* **89(11)**, 115017

Boddy, K. K., Kaplinghat, M., Kwa, A., and Peter, A. H. G.: 2016, *physical Review D* **94(12)**, 123017

Bond, J. R., Cole, S., Efstathiou, G., and Kaiser, N.: 1991, *ApJ* **379**, 440

Bose, S., Frenk, C. S., Jenkins, A., Fattahi, A., Gómez, F. A., Grand , R. J. J., Marinacci, F., Navarro, J. F., Oman, K. A., and Pakmor, R.: 2019, *MNRAS* **486(4)**, 4790

Bouwens, R. J., Illingworth, G. D., Oesch, P. A., Trenti, M., Labbé, I., Bradley, L., Carollo, M., van Dokkum, P. G., Gonzalez, V., Holwerda, B., Franx, M., Spitler, L., Smit, R., and Magee, D.: 2015, *ApJ* **803**, 34

Bovy, J., Bahmanyar, A., Fritz, T. K., and Kallivayalil, N.: 2016, *ApJ* **833**, 31

Bovy, J. and Tremaine, S.: 2012, *ApJ* **756**, 89

Bowden, A., Belokurov, V., and Evans, N. W.: 2015, *MNRAS* **449**, 1391

Bower, R. G.: 1991, *MNRAS* **248**, 332

Boylan-Kolchin, M., Bullock, J. S., and Kaplinghat, M.: 2011, *MNRAS* **415**, L40

Boylan-Kolchin, M., Bullock, J. S., and Kaplinghat, M.: 2012, *Mon. Not. Roy. Astron. Soc.* **422**, 1203

Brinckmann, T., Zavala, J., Rapetti, D., Hansen, S. H., and Vogelsberger, M.: 2018, *MNRAS* **474**, 746

Brook, C. B.: 2015, *MNRAS* **454(2)**, 1719

Brook, C. B., Santos-Santos, I., and Stinson, G.: 2016, *MNRAS* **459(1)**, 638

Brooks, A. M., Kuhlen, M., Zolotov, A., and Hooper, D.: 2013, *ApJ* **765**, 22

Brooks, A. M. and Zolotov, A.: 2014, *Astrophys. J.* **786**, 87

Brust, C., Cui, Y., and Sigurdson, K.: 2017, **8**, 020

Bryan, G. L. and Norman, M. L.: 1998, *ApJ* **495**, 80

Buckley, M. R. and Fox, P. J.: 2010, *physical Review D* **81(8)**, 083522

Buckley, M. R., Zavala, J., Cyr-Racine, F.-Y., Sigurdson, K., and Vogelsberger, M.: 2014, *physical Review D* **90(4)**, 043524

Buen-Abad, M. A., Schmaltz, M., Lesgourgues, J., and Brinckmann, T.: 2018, *Journal of Cosmology and Astro-Particle Physics* **2018(1)**, 008

Bullock, J. S. and Boylan-Kolchin, M.: 2017, *Annual Reviews of Astronomy and Astrophysics* **55**, 343

Butsky, I., Macciò, A. V., Dutton, A. A., Wang, L., Obreja, A., Stinson, G. S., Penzo, C., Kang, X., Keller, B. W., and Wadsley, J.: 2016, *MNRAS* **462**, 663

Ceverino, D. and Klypin, A.: 2009, *ApJ* **695(1)**, 292

Chacko, Z., Cui, Y., Hong, S., Okui, T., and Tsai, Y.: 2016, *Journal of High Energy Physics* **12**, 108

Chan, K. C., Sheth, R. K., and Scoccimarro, R.: 2017, *physical Review D* **96(10)**, 103543

Colín, P., Avila-Reese, V., Valenzuela, O., and Firmani, C.: 2002, *ApJ* **581**, 777

Conroy, C. and Wechsler, R. H.: 2009, *ApJ* **696**, 620

Côté, S., Carignan, C., and Freeman, K. C.: 2000, *The Astronomical Journal* **120**, 3027

Courtin, J., Rasera, Y., Alimi, J.-M., Corasaniti, P.-S., Boucher, V., and Füzfa, A.: 2011, *MNRAS* **410**, 1911

Creasey, P., Sameie, O., Sales, L. V., Yu, H.-B., Vogelsberger, M., and Zavala, J.: 2017, *MNRAS* **468**, 2283

Cyr-Racine, F.-Y., Sigurdson, K., Zavala, J., Bringmann, T., Vogelsberger, M., and Pfrommer, C.: 2016, *physical Review D* **93(12)**, 123527

Davé, R., Spergel, D. N., Steinhardt, P. J., and Wandelt, B. D.: 2001, *ApJ* **547**, 574

Davis, M., Efstathiou, G., Frenk, C. S., and White, S. D. M.: 1985, *ApJ* **292**, 371

de Blok, W. J. G., McGaugh, S. S., and Rubin, V. C.: 2001, *The Astronomical Journal* **122(5)**, 2396

de Blok, W. J. G., Walter, F., Brinks, E., Trachternach, C., Oh, S. H., and Kennicutt, R. C., J.: 2008, *The Astronomical Journal* **136(6)**, 2648

Debattista, V. P., Moore, B., Quinn, T., Kazantzidis, S., Maas, R., Mayer, L., Read, J., and Stadel, J.: 2008, *ApJ* **681**, 1076

Despali, G., Giocoli, C., Angulo, R. E., Tormen, G., Sheth, R. K., Baso, G., and Moscardini, L.: 2016, *MNRAS* **456**, 2486

Di Cintio, A., Brook, C. B., Dutton, A. A., Macciò, A. V., Stinson, G. S., and Knebe, A.: 2014, *MNRAS* **441(4)**, 2986

Di Cintio, A. and Lelli, F.: 2016, *MNRAS* **456**, L127

Di Cintio, A., Tremmel, M., Governato, F., Pontzen, A., Zavala, J., Bastidas Fry, A., Brooks, A., and Vogelsberger, M.: 2017, *Mon. Not. Roy. Astron. Soc.* **469(3)**, 2845

Díaz Rivero, A., Dvorkin, C., Cyr-Racine, F.-Y., Zavala, J., and Vogelsberger, M.: 2018, *ArXiv e-prints*

Diemand, J. and Moore, B.: 2011, *Advanced Science Letters* **4**, 297

D'Onghia, E. and Burkert, A.: 2003, *ApJ* **586(1)**, 12

D'Onghia, E., Springel, V., Hernquist, L., and Keres, D.: 2010, *ApJ* **709(2)**, 1138

Dubinski, J.: 1994, *ApJ* **431**, 617

Dubinski, J. and Carlberg, R. G.: 1991, *ApJ* **378**, 496

Dutton, A. A. and Macciò, A. V.: 2014, *MNRAS* **441**, 3359

Elbert, O. D., Bullock, J. S., Garrison-Kimmel, S., Rocha, M., Oñorbe, J., and Peter, A. H. G.: 2015, *MNRAS* **453**, 29

Elbert, O. D., Bullock, J. S., Kaplinghat, M., Garrison-Kimmel, S., Graus, A. S., and Rocha, M.: 2018, *ApJ* **853**, 109

Essig, R., Yu, H.-B., Zhong, Y.-M., and Mcdermott, S. D.: 2018

Fattahi, A., Navarro, J. F., Sawala, T., Frenk, C. S., Sales, L. V., Oman, K., Schaller, M., and Wang, J.: 2016

Feng, J. L., Kaplinghat, M., Tu, H., and Yu, H.-B.: 2009, *Journal of Cosmology and Astroparticle Physics* **7**, 004

Feng, J. L., Kaplinghat, M., and Yu, H.-B.: 2010, *physical Review D* **82(8)**, 083525

Ferrero, I., Abadi, M. G., Navarro, J. F., Sales, L. V., and Gurovich, S.: 2012, *MNRAS* **425(4)**, 2817

Ferrero, I., Navarro, J. F., Abadi, M. G., Sales, L. V., Bower, R. G., Crain, R. A., Frenk, C. S., Schaller, M., Schaye, J., and Theuns, T.: 2017, *MNRAS* **464(4)**, 4736

Finkelstein, S. L., Ryan, Jr., R. E., Papovich, C., Dickinson, M., Song, M., Somerville, R. S., Ferguson, H. C., Salmon, B., Giavalisco, M., Koekemoer, A. M., Ashby, M. L. N., Behroozi, P., Castellano, M., Dunlop, J. S., Faber, S. M., Fazio, G. G., Fontana, A., Grogin, N. A., Hathi, N., Jaacks, J., Kocevski, D. D., Livermore, R., McLure, R. J., Merlin, E., Mobasher, B., Newman, J. A., Rafelski, M., Tilvi, V., and Willner, S. P.: 2015, *ApJ* **810**, 71

Firmani, C., D'Onghia, E., Chincarini, G., Hernández, X., and Avila-Reese, V.: 2001, *MNRAS* **321(4)**, 713

Fitts, A., Boylan-Kolchin, M., Bozek, B., Bullock, J. S., Graus, A., Robles, V., Hopkins, P. F., El-Badry, K., Garrison-Kimmel, S., Faucher-Giguère, C.-A., Wetzel, A., and Kereš, D.: 2018, *arXiv e-prints*

Flores, R. A. and Primack, J. R.: 1994, *ApJl* **427**, L1

Frenk, C. S., White, S. D. M., Davis, M., and Efstathiou, G.: 1988, *ApJ* **327**, 507

Fritz, T. K., Battaglia, G., Pawlowski, M. S., Kallivayalil, N., van der Marel, R., Sohn, S. T., Brook, C., and Besla, G.: 2018, *Astronomy & Astrophysics* **619**, A103

Fry, A. B., Governato, F., Pontzen, A., Quinn, T., Tremmel, M., Anderson, L., Menon, H., Brooks, A. M., and Wadsley, J.: 2015, *Mon. Not. Roy. Astron. Soc.* **452(2)**, 1468

Garrison-Kimmel, S., Rocha, M., Boylan-Kolchin, M., Bullock, J. S., and Lally, J.: 2013, *MNRAS* **433**, 3539

Garrison-Kimmel, S., Wetzel, A., Bullock, J. S., Hopkins, P. F., Boylan-Kolchin, M., Faucher-Giguère, C.-A., Kereš, D., Quataert, E., Sanderson, R. E., Graus, A. S., and Kelley, T.: 2017, *MNRAS* **471**, 1709

Giocoli, C., Tormen, G., and van den Bosch, F. C.: 2008, *MNRAS* **386**, 2135

Gnedin, O. Y., Ceverino, D., Gnedin, N. Y., Klypin, A. A., Kravtsov, A. V., Levine, R., Nagai, D., and Yepes, G.: 2011, *arXiv e-prints* p. arXiv:1108.5736

Gnedin, O. Y. and Ostriker, J. P.: 2001, *ApJ* **561(1)**, 61

Gnedin, O. Y. and Zhao, H.: 2002, *MNRAS* **333(2)**, 299

Governato, F., Brook, C., Mayer, L., Brooks, A., Rhee, G., Wadsley, J., Jonsson, P., Willman, B., Stinson, G., Quinn, T., and Madau, P.: 2010, *Nature* **463(7278)**, 203

Guo, Q. and White, S.: 2014, *MNRAS* **437**, 3228

Guo, Q., White, S., Li, C., and Boylan-Kolchin, M.: 2010, *MNRAS* **404**, 1111

Hayashi, E., Navarro, J. F., Power, C., Jenkins, A., Frenk, C. S., White, S. D. M., Springel, V., Stadel, J., and Quinn, T. R.: 2004, *MNRAS* **355**, 794

Hayashi, E., Navarro, J. F., and Springel, V.: 2007, *MNRAS* **377**, 50

Hayashi, E., Navarro, J. F., Taylor, J. E., Stadel, J., and Quinn, T. R.: 2003, *Astrophys. J.* **584**, 541

Hernquist, L.: 1990, *Astrophys. J.* **356**, 359

Hernquist, L.: 1993, *ApJl Supp.* **86**, 389

Hopkins, P. F., Wetzel, A., Kereš, D., Faucher-Giguère, C.-A., Quataert, E., Boylan-Kolchin, M., Murray, N., Hayward, C. C., Garrison-Kimmel, S., Hummels, C., Feldmann, R., Torrey, P., Ma, X., Anglés-Alcázar, D., Su, K.-Y., Orr, M., Schmitz, D., Escala, I., Sanderson, R., Grudić, M. Y., Hafen, Z., Kim, J.-H., Fitts, A., Bullock, J. S., Wheeler, C., Chan, T. K., Elbert, O. D., and Narayanan, D.: 2018, *MNRAS* **480(1)**, 800

Huang, S., Haynes, M. P., Giovanelli, R., and Brinchmann, J.: 2012, *ApJ* **756(2)**, 113

Huo, R., Kaplinghat, M., Pan, Z., and Yu, H.-B.: 2018, *Physics Letters B* **783**, 76

Jing, Y. P. and Suto, Y.: 2002, *ApJ* **574**, 538

Johnston, K. V., Spergel, D. N., and Hernquist, L.: 1995, *ApJ* **451**, 598

Joudaki, S., Blake, C., Heymans, C., Choi, A., Harnois-Deraps, J., Hildebrandt, H., Joachimi, B., Johnson, A., Mead, A., Parkinson, D., Viola, M., and van Waerbeke, L.: 2017, *MNRAS* **465**, 2033

Kahlhoefer, F., Schmidt-Hoberg, K., Frandsen, M. T., and Sarkar, S.: 2014, *MNRAS* **437(3)**, 2865

Kamada, A., Kaplinghat, M., Pace, A. B., and Yu, H.-B.: 2017, *Physical Review Letters* **119(11)**, 111102

Kaplinghat, M., Keeley, R. E., Linden, T., and Yu, H.-B.: 2014, *Physical Review Letters* **113(2)**, 021302

Kaplinghat, M., Tulin, S., and Yu, H.-B.: 2016, *Physical Review Letters* **116(4)**, 041302

Kaplinghat, M., Valli, M., and Yu, H.-B.: 2019

Katz, H., Lelli, F., McGaugh, S. S., Di Cintio, A., Brook, C. B., and Schombert, J. M.: 2017, *MNRAS* **466(2)**, 1648

Kazantzidis, S., Abadi, M. G., and Navarro, J. F.: 2010, *ApJl* **720**, L62

Kazantzidis, S., Zentner, A. R., Kravtsov, A. V., Bullock, J. S., and Debattista, V. P.: 2009, *ApJ* **700(2)**, 1896

Kim, S. Y., Peter, A. H. G., and Hargis, J. R.: 2017a, *ArXiv e-prints*

Kim, S. Y., Peter, A. H. G., and Wittman, D.: 2017b, *MNRAS* **469(2)**, 1414

Kitching, T. D., Verde, L., Heavens, A. F., and Jimenez, R.: 2016, *MNRAS* **459**, 971

Klypin, A., Kravtsov, A. V., Valenzuela, O., and Prada, F.: 1999, *ApJ* **522**, 82

Koda, J. and Shapiro, P. R.: 2011, *MNRAS* **415**, 1125

Koposov, S. E., Rix, H.-W., and Hogg, D. W.: 2010, *ApJ* **712**, 260

Kuhlen, M., Diemand, J., and Madau, P.: 2007, *ApJ* **671**, 1135

Küpper, A. H. W., Balbinot, E., Bonaca, A., Johnston, K. V., Hogg, D. W., Kroupa, P., and Santiago, B. X.: 2015, *ApJ* **803**, 80

Kuzio de Naray, R., Martinez, G. D., Bullock, J. S., and Kaplinghat, M.: 2010, *Astrophys. J.* **710**, L161

Kuzio de Naray, R., McGaugh, S. S., and de Blok, W. J. G.: 2008, *ApJ* **676(2)**, 920

Lacey, C. and Cole, S.: 1993, *MNRAS* **262**, 627

Lelli, F., McGaugh, S. S., and Schombert, J. M.: 2016, *ApJl* **816**, L14

Leo, M., Baugh, C. M., Li, B., and Pascoli, S.: 2018, **4**, 010

Lewis, A. and Bridle, S.: 2002, *physical Review D* **66(10)**, 103511

Livermore, R. C., Finkelstein, S. L., and Lotz, J. M.: 2017, *ApJ* **835**, 113

Loeb, A. and Weiner, N.: 2011, *Physical Review Letters* **106(17)**, 171302

Lovell, M. R., Frenk, C. S., Eke, V. R., Jenkins, A., Gao, L., and Theuns, T.: 2014, *MNRAS* **439**, 300

Lovell, M. R., Zavala, J., Vogelsberger, M., Shen, X., Cyr-Racine, F.-Y., Pfrommer, C., Sigurdson, K., Boylan-Kolchin, M., and Pillepich, A.: 2018, *MNRAS* **477**, 2886

Ludlow, A. D., Navarro, J. F., Angulo, R. E., Boylan-Kolchin, M., Springel, V., Frenk, C., and White, S. D. M.: 2014, *MNRAS* **441(1)**, 378

MacCrann, N., Zuntz, J., Bridle, S., Jain, B., and Becker, M. R.: 2015, *MNRAS* **451**, 2877

Mashchenko, S., Couchman, H. M. P., and Wadsley, J.: 2006, *Nature* **442(7102)**, 539

Mashchenko, S., Wadsley, J., and Couchman, H. M. P.: 2008, *Science* **319(5860)**, 174

McCarthy, I. G., Schaye, J., Font, A. S., Theuns, T., Frenk, C. S., Crain, R. A., and Dalla Vecchia, C.: 2012, *MNRAS* **427**, 379

McLure, R. J., Dunlop, J. S., Bowler, R. A. A., Curtis-Lake, E., Schenker, M., Ellis, R. S., Robertson, B. E., Koekemoer, A. M., Rogers, A. B., Ono, Y., Ouchi, M., Charlot, S., Wild, V., Stark, D. P., Furlanetto, S. R., Cirasuolo, M., and Targett, T. A.: 2013, *MNRAS* **432**, 2696

McMillan, P. J.: 2011, *MNRAS* **414**, 2446

Menci, N., Grazian, A., Castellano, M., and Sanchez, N. G.: 2016, *ApJl* **825**, L1

Menci, N., Grazian, A., Lamastra, A., Calura, F., Castellano, M., and Santini, P.: 2018, *ApJ* **854**, 1

Menci, N., Merle, A., Totzauer, M., Schneider, A., Grazian, A., Castellano, M., and Sanchez, N. G.: 2017, *ApJ* **836**, 61

Miralda-Escudé, J.: 2002, *ApJ* **564**, 60

Miyamoto, M. and Nagai, R.: 1975, *PASP* **27**, 533

Mo, H. J. and Mao, S.: 2004, *MNRAS* **353(3)**, 829

Moore, B.: 1994, *Nature* **370**, 629

Moore, B., Ghigna, S., Governato, F., Lake, G., Quinn, T., Stadel, J., and Tozzi, P.: 1999, *ApJl* **524**, L19

Moster, B. P., Naab, T., and White, S. D. M.: 2013, *MNRAS* **428**, 3121

Moster, B. P., Somerville, R. S., Maulbetsch, C., van den Bosch, F. C., Macciò, A. V., Naab, T., and Oser, L.: 2010, *ApJ* **710**, 903

Muñoz, R. R., Majewski, S. R., and Johnston, K. V.: 2008, *ApJ* **679(1)**, 346

Murgia, R., Merle, A., Viel, M., Totzauer, M., and Schneider, A.: 2017, **11**, 046

Navarro, J. F., Eke, V. R., and Frenk, C. S.: 1996, *MNRAS* **283(3)**, L72

Navarro, J. F., Frenk, C. S., and White, S. D. M.: 1996, *Astrophys. J.* **462**, 563

Navarro, J. F., Frenk, C. S., and White, S. D. M.: 1997, *ApJ* **490**, 493

Navarro, J. F., Ludlow, A., Springel, V., Wang, J., Vogelsberger, M., White, S. D. M., Jenkins, A., Frenk, C. S., and Helmi, A.: 2010, *MNRAS* **402**, 21

Nishikawa, H., Boddy, K. K., and Kaplinghat, M.: 2019

Oñorbe, J., Boylan-Kolchin, M., Bullock, J. S., Hopkins, P. F., Kereš, D., Faucher-Giguère, C.-A., Quataert, E., and Murray, N.: 2015, *MNRAS* **454**, 2092

Ocvirk, P., Gillet, N., Shapiro, P. R., Aubert, D., Iliev, I. T., Teyssier, R., Yepes, G., Choi, J.-H., Sullivan, D., Knebe, A., Gottlöber, S., D'Aloisio, A., Park, H., Hoffman, Y., and Stranex, T.: 2016, *MNRAS* **463**, 1462

Oh, S.-H., de Blok, W. J. G., Brinks, E., Walter, F., and Kennicutt, Jr., R. C.: 2011, *The Astronomical Journal* **141**, 193

Oh, S.-H., Hunter, D. A., Brinks, E., Elmegreen, B. G., Schruba, A., Walter, F., Rupen, M. P., Young, L. M., Simpson, C. E., Johnson, M. C., Herrmann, K. A., Ficut-Vicas, D., Cigan, P., Heesen, V., Ashley, T., and Zhang, H.-X.: 2015, *The Astronomical Journal* **149(6)**, 180

Okamoto, T., Gao, L., and Theuns, T.: 2008, *MNRAS* **390**, 920

Oman, K. A., Navarro, J. F., Fattahi, A., Frenk, C. S., Sawala, T., White, S. D. M., Bower, R., Crain, R. A., Furlong, M., Schaller, M., Schaye, J., and Theuns, T.: 2015, *MNRAS* **452**, 3650

Pace, A. B.: 2016, *arXiv e-prints* p. arXiv:1605.05326

Pan, Z., Kaplinghat, M., and Knox, L.: 2018, *ArXiv e-prints*

Papastergis, E., Giovanelli, R., Haynes, M. P., and Shankar, F.: 2015, *Astronomy and Astrophysics* **574**, A113

Papastergis, E. and Shankar, F.: 2016, *Astronomy and Astrophysics* **591**, A58

Peñarrubia, J., Benson, A. J., Walker, M. G., Gilmore, G., McConnachie, A. W., and Mayer, L.: 2010, *MNRAS* **406**, 1290

Peñarrubia, J., Navarro, J. F., and McConnachie, A. W.: 2008, *Astrophys. J.* **673**, 226

Pearson, S., Küpper, A. H. W., Johnston, K. V., and Price-Whelan, A. M.: 2015, *ApJ* **799**, 28

Percival, W. J., Nichol, R. C., Eisenstein, D. J., Frieman, J. A., Fukugita, M., Loveday, J., Pope, A. C., Schneider, D. P., Szalay, A. S., Tegmark, M., Vogeley, M. S., Weinberg, D. H., Zehavi, I., Bahcall, N. A., Brinkmann, J., Connolly, A. J., and Meiksin, A.: 2007, *ApJ* **657**, 645

Persic, M., Salucci, P., and Stel, F.: 1996, *MNRAS* **281(1)**, 27

Peter, A. H. G., Rocha, M., Bullock, J. S., and Kaplinghat, M.: 2013, *MNRAS* **430**, 105

Pilipenko, S. V., Sánchez-Conde, M. A., Prada, F., and Yepes, G.: 2017, *Mon. Not. Roy. Astron. Soc.* **472**, 4918

Pineda, J. C. B., Hayward, C. C., Springel, V., and Mendes de Oliveira, C.: 2017, *MNRAS* **466(1)**, 63

Planck Collaboration, Ade, P. A. R., Aghanim, N., Armitage-Caplan, C., Arnaud, M., Ashdown, M., Atrio-Barandela, F., Aumont, J., Baccigalupi, C., Banday, A. J., and et al.: 2014, *Astronomy and Astrophysics* **571**, A16

Planck Collaboration, Ade, P. A. R., Aghanim, N., Arnaud, M., Ashdown, M., Aumont, J., Baccigalupi, C., Banday, A. J., Barreiro, R. B., Bartlett, J. G., and et al.: 2016, *Astronomy and Astrophysics* **594**, A13

Planck Collaboration, Aghanim, N., Akrami, Y., Ashdown, M., Aumont, J., Baccigalupi, C., Ballardini, M., Banday, A. J., Barreiro, R. B., Bartolo, N., Basak, S., Battye, R., Benabed, K., Bernard, J. P., Bersanelli, M., Bielewicz, P., Bock, J. J., Bond, J. R., Borrill, J., Bouchet, F. R., Boulanger, F., Bucher, M., Burigana, C., Butler, R. C., Calabrese, E., Cardoso, J. F., Carron, J., Challinor, A., Chiang, H. C., Chluba, J., Colombo, L. P. L., Combet, C., Contreras, D., Crill, B. P., Cuttaia, F., de Bernardis, P., de Zotti, G., Delabrouille, J., Delouis, J. M., Di Valentino, E., Diego, J. M., Doré, O., Douspis, M., Ducout, A., Dupac, X., Dusini, S., Efstathiou, G., Elsner, F., Enßlin, T. A., Eriksen, H. K., Fantaye, Y., Farhang, M., Fergusson, J., Fernandez-Cobos, R., Finelli, F., Forastieri, F., Frailis, M., Franceschi, E., Frolov, A., Galeotta, S., Galli, S., Ganga, K., Génova-Santos, R. T., Gerbino, M., Ghosh, T., González-Nuevo, J., Górski, K. M., Gratton, S., Gruppuso, A., Gudmundsson, J. E., Hamann, J., Hand ley, W., Herranz, D., Hivon, E., Huang, Z., Jaffe, A. H., Jones, W. C., Karakci, A., Keihänen, E., Keskitalo, R., Kiiveri, K., Kim, J., Kisner, T. S., Knox, L., Krachmalnicoff, N., Kunz, M., Kurki-Suonio, H., Lagache, G., Lamarre, J. M., Lasenby, A., Lattanzi, M., Lawrence, C. R., Le Jeune, M., Lemos, P., Lesgourgues, J., Levrier, F., Lewis, A., Liguori, M., Lilje, P. B., Lilley, M., Lindholm, V., López-Caniego, M., Lubin, P. M., Ma, Y. Z., Macías-Pérez, J. F., Maggio, G., Maino, D., Mandolesi, N., Mangilli, A., Marcos-Caballero, A., Maris, M., Martin, P. G., Martinelli, M., Martínez-González, E., Matarrese, S., Mauri, N., McEwen, J. D., Meinhold, P. R., Melchiorri, A., Mennella, A., Migliaccio, M., Millea, M., Mitra, S., Miville-Deschênes, M. A., Molinari, D., Montier, L., Morgante, G., Moss, A., Natoli, P., Nørgaard-Nielsen, H. U., Pagano, L., Paoletti, D., Partridge, B., Patanchon, G., Peiris, H. V., Perrotta, F., Pettorino, V., Piacentini, F., Polastri, L., Polenta, G., Puget, J. L., Rachen, J. P., Reinecke, M., Remazeilles, M., Renzi, A., Rocha, G., Rosset, C., Roudier, G., Rubiño-Martín, J. A., Ruiz-Granados, B., Salvati, L., Sandri, M., Savelainen, M., Scott, D., Shellard, E. P. S., Sirignano, C., Sirri, G., Spencer, L. D., Sunyaev, R., Suur-Uski, A. S., Tauber, J. A., Tavagnacco, D., Tenti, M., Toffolatti, L., Tomasi, M., Trombetti, T., Valenziano, L., Valiviita, J., Van Tent, B., Vibert, L., Vielva, P., Villa, F., Vittorio, N., Wand elt, B. D., Wehus, I. K., White, M., White, S. D. M., Zacchei, A., and Zonca, A.: 2018, *arXiv e-prints* p. arXiv:1807.06209

Pontzen, A. and Governato, F.: 2012, *MNRAS* **421**, 3464

Power, C., Navarro, J. F., Jenkins, A., Frenk, C. S., White, S. D. M., Springel, V., Stadel, J., and Quinn, T.: 2003, *MNRAS* **338**, 14

Press, W. H. and Schechter, P.: 1974, *ApJ* **187**, 425

Randall, S. W., Markevitch, M., Clowe, D., Gonzalez, A. H., and Bradač, M.: 2008, *ApJ* **679(2)**, 1173

Read, J. I., Agertz, O., and Collins, M. L. M.: 2016a, *MNRAS* **459(3)**, 2573

Read, J. I. and Gilmore, G.: 2005, *MNRAS* **356(1)**, 107

Read, J. I., Iorio, G., Agertz, O., and Fraternali, F.: 2016b, *MNRAS* **462**, 3628

Read, J. I., Walker, M. G., and Steger, P.: 2018, *Mon. Not. Roy. Astron. Soc.* **481(1)**, 860

Read, J. I., Walker, M. G., and Steger, P.: 2019, *Mon. Not. Roy. Astron. Soc.* "**484**", ”1401

Ren, T., Kwa, A., Kaplinghat, M., and Yu, H.-B.: 2018, *ArXiv e-prints*

Rhee, G., Valenzuela, O., Klypin, A., Holtzman, J., and Moorthy, B.: 2004, *ApJ* **617**, 1059

Riess, A. G., Macri, L. M., Hoffmann, S. L., Scolnic, D., Casertano, S., Filippenko, A. V., Tucker, B. E., Reid, M. J., Jones, D. O., Silverman, J. M., Chornock, R., Challis, P., Yuan, W., Brown, P. J., and Foley, R. J.: 2016, *ApJ* **826**, 56

Robertson, A., Harvey, D., Massey, R., Eke, V., McCarthy, I. G., Jauzac, M., Li, B., and Schaye, J.: 2018a, *ArXiv e-prints*

Robertson, A., Massey, R., and Eke, V.: 2017, *MNRAS* **465(1)**, 569

Robertson, A., Massey, R., Eke, V., Tulin, S., Yu, H.-B., Bahé, Y., Barnes, D. J., Bower, R. G., Crain, R. A., Dalla Vecchia, C., Kay, S. T., Schaller, M., and Schaye, J.: 2018b, *MNRAS* **476**, L20

Robles, V. H., Bullock, J. S., Elbert, O. D., Fitts, A., González-Samaniego, A., Boylan-Kolchin, M., Hopkins, P. F., Faucher-Giguère, C.-A., Kereš, D., and Hayward, C. C.: 2017a, *ArXiv e-prints*

Robles, V. H., Bullock, J. S., Elbert, O. D., Fitts, A., González-Samaniego, A., Boylan-Kolchin, M., Hopkins, P. F., Faucher-Giguère, C.-A., Kereš, D., and Hayward, C. C.: 2017b, *MNRAS* **472**, 2945

Robles, V. H., Kelley, T., Bullock, J. S., and Kaplinghat, M.: 2019

Rocha, M., Peter, A. H. G., Bullock, J. S., Kaplinghat, M., Garrison-Kimmel, S., Oñorbe, J., and Moustakas, L. A.: 2013, *MNRAS* **430**, 81

Rubin, V. C. and Ford, W. Kent, J.: 1970, *ApJ* **159**, 379

Sales, L. V., Navarro, J. F., Oman, K., Fattahi, A., Ferrero, I., Abadi, M., Bower, R., Crain, R. A., Frenk, C. S., Sawala, T., Schaller, M., Schaye, J., Theuns, T., and White, S. D. M.: 2017, *MNRAS* **464(2)**, 2419

Sameie, O., Creasey, P., Yu, H.-B., Sales, L. V., Vogelsberger, M., and Zavala, J.: 2018, *MNRAS* **479**, 359

Sameie, O., Yu, H.-B., Sales, L. V., Vogelsberger, M., and Zavala, J.: 2019, *arXiv e-prints* p. arXiv:1904.07872

Sanders, R. H. and McGaugh, S. S.: 2002, *Annual Reviews of Astronomy and Astrophysics* **40**, 263

Santos-Santos, I. M., Brook, C. B., Stinson, G., Di Cintio, A., Wadsley, J., Domínguez-Tenreiro, R., Gottlöber, S., and Yepes, G.: 2016, *MNRAS* **455(1)**, 476

Santos-Santos, I. M., Di Cintio, A., Brook, C. B., Macciò, A., Dutton, A., and Domínguez-Tenreiro, R.: 2018, *MNRAS* **473**, 4392

Sawala, T. et al.: 2016, *Mon. Not. Roy. Astron. Soc.* **457(2)**, 1931

Sawala, T., Frenk, C. S., Fattahi, A., Navarro, J. F., Bower, R. G., Crain, R. A., Dalla Vecchia, C., Furlong, M., Jenkins, A., McCarthy, I. G., Qu, Y., Schaller, M., Schaye, J., and Theuns, T.: 2015, *MNRAS* **448(3)**, 2941

Schaller, M., Frenk, C. S., Bower, R. G., Theuns, T., Jenkins, A., Schaye, J., Crain, R. A., Furlong, M., Dalla Vecchia, C., and McCarthy, I. G.: 2015, *MNRAS* **451(2)**, 1247

Schaye, J., Crain, R. A., Bower, R. G., Furlong, M., Schaller, M., Theuns, T., Dalla Vecchia, C., Frenk, C. S., McCarthy, I. G., Helly, J. C., Jenkins, A., Rosas-Guevara, Y. M., White, S. D. M., Baes, M., Booth, C. M., Camps, P., Navarro, J. F., Qu, Y., Rahmati, A., Sawala, T., Thomas, P. A., and Trayford, J.: 2015, *MNRAS* **446(1)**, 521

Schechter, P.: 1976, *ApJ* **203**, 297

Schneider, A.: 2015, *MNRAS* **451**, 3117

Schneider, A., Smith, R. E., and Reed, D.: 2013, *MNRAS* **433**, 1573

Schneider, A., Trujillo-Gomez, S., Papastergis, E., Reed, D. S., and Lake, G.: 2016, *ArXiv e-prints*

Schneider, A., Trujillo-Gomez, S., Papastergis, E., Reed, D. S., and Lake, G.: 2017, *MNRAS* **470**, 1542

Sheth, R. K., Mo, H. J., and Tormen, G.: 2001, *MNRAS* **323**, 1

Sheth, R. K. and Tormen, G.: 1999, *MNRAS* **308**, 119

Song, M., Finkelstein, S. L., Ashby, M. L. N., Grazian, A., Lu, Y., Papovich, C., Salmon, B., Somerville, R. S., Dickinson, M., Duncan, K., Faber, S. M., Fazio, G. G., Ferguson, H. C., Fontana, A., Guo, Y., Hathi, N., Lee, S.-K., Merlin, E., and Willner, S. P.: 2016, *ApJ* **825**, 5

Spekkens, K., Giovanelli, R., and Haynes, M. P.: 2005, *The Astronomical Journal* **129**, 2119

Spergel, D. N. and Steinhardt, P. J.: 2000, *Physical Review Letters* **84**, 3760

Springel, V.: 2005, *MNRAS* **364**, 1105

Springel, V.: 2010, *MNRAS* **401**, 791

Springel, V., Di Matteo, T., and Hernquist, L.: 2005, *MNRAS* **361(3)**, 776

Springel, V., Wang, J., Vogelsberger, M., Ludlow, A., Jenkins, A., Helmi, A., Navarro, J. F., Frenk, C. S., and White, S. D. M.: 2008, *Mon. Not. Roy. Astron. Soc.* **391**, 1685

Springel, V., Yoshida, N., and White, S. D. M.: 2001, *New Astronomy* **6**, 79

Swaters, R. A., Madore, B. F., van den Bosch, F. C., and Balcells, M.: 2003, *ApJ* **583**, 732

Swaters, R. A., Sanders, R. H., and McGaugh, S. S.: 2010, *ApJ* **718(1)**, 380

Tinker, J., Kravtsov, A. V., Klypin, A., Abazajian, K., Warren, M., Yepes, G., Gottlöber, S., and Holz, D. E.: 2008, *ApJ* **688**, 709

Tissera, P. B., White, S. D. M., Pedrosa, S., and Scannapieco, C.: 2010, *MNRAS* **406**, 922

Tollet, E. et al.: 2016, *Mon. Not. Roy. Astron. Soc.* **456(4)**, 3542

Tulin, S. and Yu, H.-B.: 2018, *physical Reports* **730**, 1

Tulin, S., Yu, H.-B., and Zurek, K. M.: 2013a, *physical Review D* **87(11)**, 115007

Tulin, S., Yu, H.-B., and Zurek, K. M.: 2013b, *Physical Review Letters* **110(11)**, 111301

Tully, R. B. and Fisher, J. R.: 1977, *Astronomy and Astrophysics* **54**, 661

Vale, A. and Ostriker, J. P.: 2004, *MNRAS* **353**, 189

Vale, A. and Ostriker, J. P.: 2006, *MNRAS* **371**, 1173

Valli, M. and Yu, H.-B.: 2018, *Nature Astronomy*

van den Aarssen, L. G., Bringmann, T., and Pfrommer, C.: 2012, *Physical Review Letters* **109(23)**, 231301

van den Bosch, F. C., Robertson, B. E., Dalcanton, J. J., and de Blok, W. J. G.: 2000, *The Astronomical Journal* **119**, 1579

Vera-Ciro, C. A., Sales, L. V., Helmi, A., Frenk, C. S., Navarro, J. F., Springel, V., Vogelsberger, M., and White, S. D. M.: 2011, *MNRAS* **416**, 1377

Vogelsberger, M., Genel, S., Springel, V., Torrey, P., Sijacki, D., Xu, D., Snyder, G., Nelson, D., and Hernquist, L.: 2014a, *MNRAS* **444**, 1518

Vogelsberger, M., Zavala, J., Cyr-Racine, F.-Y., Pfrommer, C., Bringmann, T., and Sigurdson, K.: 2016, *MNRAS* **460**, 1399

Vogelsberger, M., Zavala, J., and Loeb, A.: 2012, *MNRAS* **423**, 3740

Vogelsberger, M., Zavala, J., Schutz, K., and Slatyer, T. R.: 2019, *MNRAS* **484**, 5437

Vogelsberger, M., Zavala, J., Simpson, C., and Jenkins, A.: 2014b, *MNRAS* **444**, 3684

Wang, L., Dutton, A. A., Stinson, G. S., Macciò, A. V., Penzo, C., Kang, X., Keller, B. W., and Wadsley, J.: 2015, *MNRAS* **454(1)**, 83

Wetzel, A. R., Hopkins, P. F., Kim, J.-h., Faucher-Giguère, C.-A., Kereš, D., and Quataert, E.: 2016, *The Astrophysical Journal, Letters* **827**, L23

Yoshida, N., Springel, V., White, S. D. M., and Tormen, G.: 2000a, *ApJ* **535(2)**, L103

Yoshida, N., Springel, V., White, S. D. M., and Tormen, G.: 2000b, *ApJl* **544**, L87

Zavala, J., Vogelsberger, M., and Walker, M. G.: 2013, *MNRAS* **431**, L20

Zhu, Q., Marinacci, F., Maji, M., Li, Y., Springel, V., and Hernquist, L.: 2016, *MNRAS* **458**, 1559

Zwicky, F.: 1933, *Helvetica Physica Acta* **6**, 110

Zwicky, F.: 1937, *ApJ* **86**, 217